

Dissertation
submitted to the
Combined Faculties of the Natural Sciences and Mathematics
of the Ruperto-Carola-University of Heidelberg, Germany
for the degree of
Doctor of Natural Sciences

Put forward by
Diplom-Physiker Christoph Diehl
born in: Mainz
Oral examination: 11.05.2011

First mass measurements with the MPIK/UW-PTMS

Referees:

Prof. Dr. Klaus Blaum
PD Dr. Wolfgang Quint

Zusammenfassung in Deutsch:

Die genaue Bestimmung des ${}^3\text{H}$ - ${}^3\text{He}$ Massenverhältnisses und daraus resultierend des Q -Wertes von Tritium, trägt zur Bestimmung der Elektron-Antineutrino-Masse durch das Karlsruhe Tritium Neutrino Experiment (KATRIN) bei. Eine Bestimmung des Massenverhältnisses mit einer Genauigkeit von besser als $1 \cdot 10^{-10}$ erlaubt einen Test des systematischen Fehlers der Endpunktsbestimmung des Betazerfalls von ${}^3\text{H}$ zu ${}^3\text{He}$ in der Datenanalyse von KATRIN. Um diese Präzision zu erreichen wurde ein Penningfallen-massenspektrometer (MPIK/UW-PTMS) an der University of Washington konstruiert und ans Max-Planck-Institut für Kernphysik transferiert. Hier wurde ein spezielles Tritiumlabor eingerichtet, in dem mehrere Umweltparameter, wie zum Beispiel das Magnetfeld und die Temperatur, stabilisiert werden. Das Experiment wurde in Betrieb genommen und ausführliche Messungen zur Charakterisierung des Spektrometers und zur Optimierung experimenteller Prozeduren wurden am Testion ${}^{12}\text{C}^{4+}$ durchgeführt. Erste Massenmessungen mit dem Spektrometer wurden mit ${}^1\text{H}^+$ und ${}^{16}\text{O}^{6+}$ durchgeführt. Diese lieferten eine Genauigkeit der Messungen von einigen 10^{-8} , zeigen aber auch das Potential des Spektrometers bald eine Präzision von besser als $1 \cdot 10^{-10}$ zu erreichen.

Zusammenfassung in Englisch:

The precise determination of the ${}^3\text{H}$ - ${}^3\text{He}$ mass ratio, and hence the tritium Q -value, is of relevance for the measurement of the electron anti-neutrino mass performed by the Karlsruhe Tritium Neutrino experiment (KATRIN). By determining this ratio to an uncertainty of better than 1 part in 10^{10} , systematic errors of the endpoint energy in the β -decay of ${}^3\text{H}$ to ${}^3\text{He}$ can be checked in the data analysis of KATRIN. To reach this precision, a Penning Trap Mass Spectrometer (MPIK/UW-PTMS) was constructed at the University of Washington, which has been transferred to the Max-Planck-Institute for Nuclear Physics in Heidelberg. Here, a dedicated tritium laboratory was set up. Special care was taken to stabilize several environmental parameters, such as the magnetic field or the temperature. The experiment was commissioned and extensive measurements with the test ion ${}^{12}\text{C}^{4+}$ were carried out in order to characterize the spectrometer and to optimize the experimental procedures. Finally, the first mass measurements with the spectrometer were performed on ${}^1\text{H}^+$ and ${}^{16}\text{O}^{6+}$, yielding an uncertainty of some parts in 10^8 , but also showing the potential of the spectrometer to reach a precision below 1 part in 10^{10} in the near future.

Contents

List of Figures	viii
List of Tables	xi
1 Introduction and motivation	1
1.1 Precision mass spectrometry	1
1.1.1 History of precision mass spectrometry	1
1.1.2 Penning trap mass spectrometry	3
1.2 The MPIK/UW-PTMS experiment	4
2 The search for the neutrino mass	6
2.1 The neutrino mass	6
2.2 Approaches to determine the neutrino mass	9
2.2.1 Double beta-decay	9
2.2.2 Cosmology	10
2.2.3 Ordinary beta-decay	11
2.2.4 Penning trap mass spectrometry	15
3 Penning trap theory	23
3.1 Electrostatics of the Penning trap	23
3.2 Harmonic ion motion in a Penning trap	24
3.3 Axial ion detection	27
3.3.1 Harmonic oscillator model of the ion	28
3.3.2 Lineshapes in axial ion detection	31
3.3.3 Axial frequency resolution	34
3.3.4 Incoherent noise detection	35
3.4 Shifts to the axial frequency	37
3.4.1 Higher order effects and special relativity	37
3.4.2 Misalignment and trap ellipticity	40
3.4.3 Miscellaneous frequency shifts	40
3.5 Cooling mechanisms	41
3.5.1 Magnetron cooling	42
3.5.2 Modified cyclotron cooling	43
3.6 Mass measurements and radial detection	43
3.6.1 The invariance theorem	44
3.6.2 Triggered sweep radial detection technique	44

4	Experimental setup	47
4.1	Experimental hardware	47
4.1.1	Double trap assembly	48
4.1.2	Ion creation	50
4.1.3	Magnet systems	53
4.1.4	Mechanical arrangement and vacuum components	56
4.1.5	Feedthrough of electronic signals to the traps	59
4.2	Electronics	60
4.2.1	Trap connections and external tuned circuit	62
4.2.2	Drive system	63
4.2.3	Axial amplifier	66
4.2.4	Room-temperature electronics and frequency lock	66
4.2.5	Voltage sources	68
4.3	Automation and data acquisition	68
4.3.1	Controller user interface	69
4.3.2	Control architecture	69
4.3.3	Data acquisition and automated analysis	71
4.3.4	Automation of experimental standard procedures	72
5	The Heidelberg tritium laboratory	74
5.1	Tritium safety concept	74
5.2	Environment stabilization systems	78
5.2.1	Magnetic field stabilization	79
5.2.2	Temperature stabilization	81
5.2.3	Vibration isolation	81
5.3	Adaption to the already existing spectrometer	81
6	Experimental results	83
6.1	Commissioning experiments	83
6.1.1	Tuned circuit and noise sources	84
6.1.2	Compensation of drive signals	86
6.1.3	Alignment of the traps	87
6.1.4	Bake-out of the traps	88
6.2	Ion preparation	89
6.2.1	Loading from the external ion source and the gas handling system	89
6.2.2	Loading from the field emission point	92
6.2.3	Application of different contaminant removal methods	93
6.2.4	Preparation of small ion clouds	95
6.3	Measurement of the eigenfrequencies and optimization of trap parameters	97
6.3.1	Axial frequency measurements	97
6.3.2	Measurements of the modified cyclotron frequency	108
6.3.3	Magnetron frequency measurements	112

6.4	Mass measurements	114
6.4.1	The proton mass measurement	116
6.4.2	The oxygen mass measurement	118
6.4.3	Systematic shifts	118
6.4.4	Summary of the mass measurements	124
7	Conclusions and outlook	126
	Bibliography	128

List of Figures

1.1	Uncertainty of the ^{28}Si mass over time.	2
2.1	Neutrino mass limits from experiment.	8
2.2	Feynman diagrams of double beta-decay.	9
2.3	Spectrum of the electrons emitted in tritium β -decay towards the endpoint.	11
2.4	Drawing of the KATRIN setup.	14
2.5	Schematic drawing of a MAC-E-filter.	16
2.6	Energy level diagram for tritium β -decay.	18
2.7	The spectrum of tritium β -decay electrons around the endpoint.	20
2.8	Development of the $^3\text{H}/^3\text{He}$ mass difference uncertainty over time.	21
3.1	General definition of a hyperbola.	24
3.2	Schematic drawing of a Penning trap.	25
3.3	Eigenmotions in a Penning trap.	26
3.4	Simple ion detection model.	29
3.5	The equivalent parallel circuit of a real inductor.	30
3.6	Tuned circuit model of the ion.	31
3.7	Lineshape and phase of an axial resonance.	32
3.8	Axial resonances with varying parameters.	33
3.9	The effect of noise on the axial resolution.	34
3.10	Hot ion cloud on top of the external tuned circuit.	35
3.11	Energy level diagram of an ion in a Penning trap.	42
3.12	Simulated modified cyclotron resonances.	45
4.1	Overview on the apparatus.	48
4.2	Sectional drawing of the trap tower.	49
4.3	Schematics and model of the external ion source.	50
4.4	Drawing of the gas handling system.	52
4.5	Setting of the electrodes and potential during the loading procedure.	53
4.6	Photos of the 1991 magnet.	54
4.7	Drawing of the Nalorac 1995 liquid helium cryostat.	55
4.8	Overview on the mechanical arrangement of the setup.	57
4.9	Drawing of the rotation and translation stage of the experiment.	58
4.10	One of the spare feedthrough flanges.	59
4.11	The basic detection scheme including two traps.	60
4.12	Concept of the external tuned circuit for a double Penning trap configuration.	61

4.13	Drive scheme for the double Penning trap.	64
4.14	Schematics of the detection electronics.	67
4.15	Screenshot of the experiment control program Controller 2.0.	70
4.16	Architecture of the computer control system of the experiment.	71
5.1	Schematic drawing of the safety system in the tritium laboratory.	75
5.2	Photo of the tritium cylinder and the gas handling system.	76
5.3	Glove boxes for tritium containment.	77
5.4	Performance of the pressure stabilization system.	80
5.5	Moving the experiment between room 1 and 2.	82
6.1	Cyclotron frequency measurements of $^{12}\text{C}^{5+}$ to determine the magnetic field drift of the superconducting magnet in Seattle.	84
6.2	Tuned circuit with and without additional noise.	85
6.3	Noise induced by the liquid helium stack heaters at the center of the tuned circuit.	86
6.4	Pressure at the gauge close to the turbo pump during the bake-out of the traps after exposure to air.	88
6.5	Vacuum pressure during the emission of electrons from the ion source.	90
6.6	Coherent signal of protons in the capture trap.	91
6.7	Mass spectrum from a FEP load.	92
6.8	Pictogram of the steps necessary for single ion preparation.	96
6.9	Damping of the axial motion directly after loading and after some preparation of the ion cloud.	98
6.10	Axial frequency sweeps of different quality.	100
6.11	Narrow axial resonance.	101
6.12	Centers of axial resonances and temperature close to the voltage source taken over one night.	102
6.13	Change of the lock voltage and the temperature close to the voltage source during a long-term magnetron frequency measurement.	103
6.14	Effect of guard tuning on the resonance shape.	105
6.15	Finding the optimum guard voltage by comparing changes in the correction voltage for different drive strengths.	106
6.16	Measurement for the determination of the electric center of the trap.	107
6.17	Modified cyclotron cooling resonance in the error signal.	108
6.18	Modified cyclotron resonances for $^{12}\text{C}^{4+}$	109
6.19	Modified cyclotron resonances in the error and the correction signal.	110
6.20	The drift of the magnetic field over 100 hours, observed by measuring cyclotron resonances for $^{12}\text{C}^{4+}$	111
6.21	Modified cyclotron data after removing a linear drift.	112
6.22	Magnetron cooling resonances of $^{12}\text{C}^{4+}$	113
6.23	Magnetron cooling frequency over time.	114

6.24	The proton data set.	117
6.25	The oxygen data set.	119
6.26	The oxygen data set before removing a linear drift.	123

List of Tables

3.1	Typical motional frequencies and energies in the Penning trap used for this thesis work.	28
4.1	Specifications of the 1995 magnet.	54
4.2	Typical parameters of the tuned circuit.	62
4.3	Specifications of synthesizers and the frequency standard in use with the experiment.	65
5.1	Stabilization of environmental conditions in Heidelberg.	79
6.1	Helpful quantities for axial frequency measurements.	97
6.2	Result of trap angle measurements via the magnetron frequency.	113
6.3	Absolute and relative statistical errors for the proton measurement.	116
6.4	Absolute and relative statistical errors for the oxygen measurement.	118
6.5	Shifts in the cyclotron frequency due to the coupling of the eigenmotions.	120
6.6	Systematic errors and their absolute and relative contribution to the cyclotron frequencies.	125

1 Introduction and motivation

Precision measurements of already known fundamental quantities in physics can result in new insights or provide stringent tests of theories. Examples are the high-precision spectroscopic measurements on the hydrogen atom [F⁺04] and the measurements of the g -factor of the free electron [HFG08]. Also, the efforts in improving the precision on a specific quantity often result in the development of new methods, as will be discussed in section 1.1.1. The aim of the experiment presented in this thesis work is to improve the precision in the knowledge of the energy released in the β -decay of tritium. Though this quantity is not very fundamental by itself, it is an important parameter for the determination of a very fundamental quantity: the mass of the neutrino.

1.1 Precision mass spectrometry

Mass spectrometry is a field of physics and chemistry that deals with weighing and categorizing microscopic objects such as atoms, molecules and clusters by their mass. Its applications reach from fundamental studies like the measurement of single atom masses [Bla06], over dating archaeological samples, [NKS77] to commercial applications like detection of explosives at airports [COTW06]. Many different techniques have been developed throughout the last century which can be roughly classified into techniques that actually determine the masses of specific particles, and techniques that measure the abundance of particles in a given sample. Although the latter make up the majority of available techniques and are of utmost relevance especially in the fields of chemistry and biology, these techniques will not be discussed in the framework of this thesis. Instead, mass spectrometry will be described in terms of weighing objects (by means of frequency measurements) and the mass spectrometers discussed are the equivalent of a balance on the atomic scale.

1.1.1 History of precision mass spectrometry

The history of mass spectrometry starts with the discovery of the electron and the measurement of its charge-to-mass-ratio by Thomson in 1897 [Tho97]. In these experiments, he utilized electric and magnetic fields to deflect the charged electrons. In one or the other way mass-dependent response of charged particles to electromagnetic fields still is the basic principle of all mass spectrometers. In 1906, Thomson was awarded the Nobel Prize in Physics for his discovery of the electron. The first mass spectrometer was developed in Thomsons laboratory, too. In this parabola spectrograph, an ion beam had to pass crossed electric and magnetic fields resulting in a splitting of the beam path depending on the charge-to-mass-ratio of the particles [Tho07]. In 1912, Thomson discovered the existence

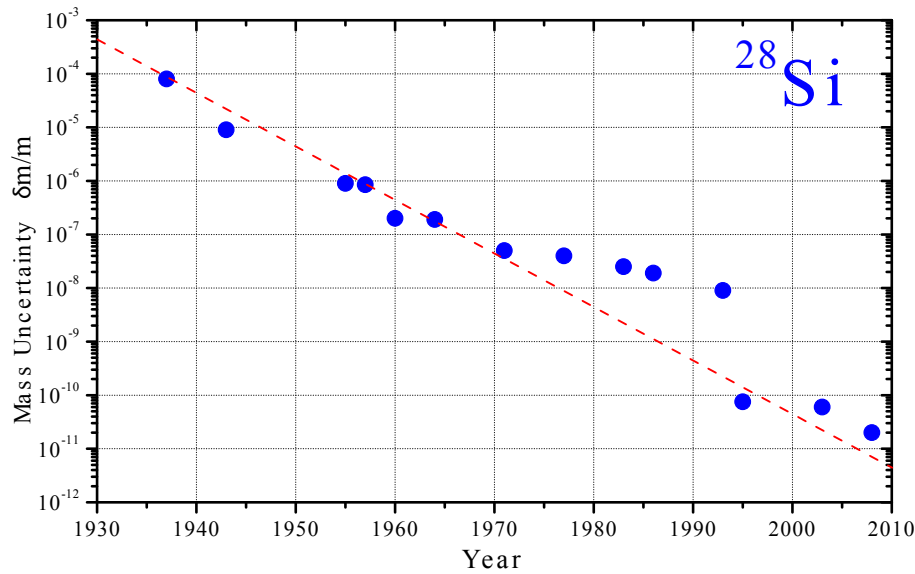


Figure 1.1: The uncertainty of the ^{28}Si mass is plotted over time. The jump in uncertainty in the 1990s is attributed to the advent of Penning trap mass spectrometry. The dashed line gives a guide to the eye and has a slope of one order of magnitude per decade. Courtesy of Klaus Blaum.

of isotopes in this apparatus by separating ^{20}Ne from ^{22}Ne [Tho12]. In the following years, Aston, a student of Thomson, further refined the apparatus and was able to discover more than 200 stable isotopes [Ast19]. For this discovery, he received the Nobel Prize in Chemistry in 1922. Aston's spectrograph achieved a relative mass uncertainty on the order of 10^{-4} and hence was able to also demonstrate the existence of the binding energy of the nucleus (the so-called mass defect) [Ast22]. In the next decades, Dempster [Dem35], Mat- tauch and Herzog [MH34], Nier [Nie47], and many others improved the basic concept of the parabola spectrograph and finally reached uncertainties of the order of 10^{-7} .

In the 1950s, another development started in parallel, the utilization of ion storage devices instead of beam apparatuses. Leading contributors in this field were Paul [Pau90] and Dehmelt [Deh90], who both received the Nobel Prize in Physics in 1989 for the development of the ion trapping technique. The Paul trap [PS53] is based on the superposition of a static electric field together with a radiofrequency field to achieve the three-dimensional confinement of the particles. Mass measurements can in principle be performed in a Paul trap, and its linear version, the quadrupole mass filter, is widely used in many fields of mass spectrometry. However, the accuracy is limited by the electric field stability and disturbances of the ion motion due to the applied radiofrequencies.

The Penning trap, which will be discussed in more detail in the following sections, was developed by Dehmelt at the University of Washington in Seattle for experiments with single electrons [WED78, VDSD87]. Nowadays, it is the most accurate device for high-

precision mass measurements available, with demonstrated uncertainties below 1 part in 10^{11} [RTP04]. However, before the potential of the Penning trap for mass spectrometry was realized, a different technique evolved: radiofrequency mass spectrometry. Pioneering work in this field was carried out by Smith, who was the first being able to relate the mass of a particle to a frequency measured in an experiment [SD56]. The mass synchronometer measured the cyclotron frequency ω_c in a magnetic field B , which is directly related to the charge-to-mass ratio q/m of a particle via

$$\omega_c = \frac{qB}{m}. \quad (1.1)$$

Due to the great improvements in atomic clocks, measuring a frequency is nowadays the measurement with the smallest intrinsic uncertainty. Based on the same idea, today mainly two different techniques are utilized in high-precision mass spectrometry: The already mentioned Penning trap and the storage ring [FGM08]. The latter acts as a big trap, where an ion beam circulates along a ring-shaped beamline. The mass of these ions is measured via the image-charges induced in a pickup capacitor that oscillate at a characteristic frequency [F^{+95} , H^{+00}]. One advantage of this technique is that many different masses can be determined at once, which makes the storage ring an excellent tool for mapping the masses of large parts of the nuclear chart. However, due to, e.g. the complexity of the ring and the stability of the many magnets involved in the measurements, the accuracy of the storage ring is limited to 1 part in 10^7 so far.

A good illustration of the advance in mass spectrometry is plotting the experimental uncertainties for a particular isotope versus time. This is illustrated for the case of ^{28}Si in Fig. 1.1. More details on the exciting history of mass spectrometry can be found elsewhere [Wap95, Bla06, Scr10].

1.1.2 Penning trap mass spectrometry

As already mentioned, the Penning trap is the mass spectrometer with the smallest demonstrated uncertainty so far. The basic principle of the Penning trap is to store a particle in a combination of a strong magnetic field with a weak electrostatic quadrupole field. The basic idea of slowing or even storing particles in an axial magnetic field was proposed by Penning [Pen36] for the implementation of a vacuum gauge. However, here no electrostatic trap structure was involved. The first description of the Penning trap was given by Pierce in 1949 [Pie49], who added endcaps to confine the particles axially and thus in three dimensions. The experimental realization of a Penning trap was carried out by Dehmelt in 1959, who also later proposed the name Penning trap in recognition of Penning [Deh68, Deh69]. Some major achievements in Dehmelt's Penning trap work were the first storage and detection of a single electron in a Penning trap [WED78] and the measurement of the g -factor of the free electron [VSD87]. Stimulated by Dehmelt's work, another group around Gräff started investigations of electrons in a Penning trap [GMRW68]. In Gräff's group in Mainz the first measurements of mass ratios in Penning traps were carried out, namely on the

electron-proton mass ratio [GK78, GKT80]. The Mainz group stayed quite active in the field of Penning trap based mass measurements [GWW90, BESW01] and initiated a number of activities at other sites, such as mass measurements on short-lived ions at radioactive beam facilities with the ISOLTRAP experiment [S⁺90] and measurements of highly charged ions at SMILETRAP [J⁺93]. In parallel to the Mainz measurements, the Seattle group entered the area of mass measurements with work carried out by Van Dyck, a co-worker of Dehmelt [VDWED76]. The first measurement was performed on the electron-positron mass ratio in 1979 [SVDD81], followed by measurements of the electron-proton mass ratio [VDS81]. A more systematic program on mass measurements was started in 1986 with a measurement of the proton mass [VDFDP89]. In this program the masses of several light isotopes, such as ⁴He [VDZVL⁺04] and ¹⁶O [VDPVLZ06] were determined with a final uncertainty of about 1 part in 10¹¹. In the late 1980s, also the group of Pritchard at MIT joined the high-precision mass measurement community with a measurement of the mass ratio of CO to N₂ [C⁺89]. The MIT group developed a technique for measuring mass doublets simultaneously in one trap and performed measurements with an uncertainty below 1 part in 10¹¹ [RTP04, R⁺05]. In 2003, the experiment was moved to the group of Myers at Florida State University, now being called the FSU/MIT-Trap. Here relative mass measurements in the 10⁻¹¹ range are still carried out [RWMM07, MRM09]. Also the field of mass measurements on short-lived isotopes has been greatly expanded since the start of ISOLTRAP, and many similar facilities have been setup. A good overview on this diverse field can be found in the review article of Blaum [Bla06]. The experiment described in this thesis work combines the Mainz and Seattle activities on high-precision mass measurements. It was developed at the University of Washington by Pinegar [Pin07], a student of Van Dyck, as an improvement to the original precision spectrometer. When the Seattle activities came to an end in 2008, the experiment was moved to the Max-Planck-Institut für Kernphysik, where Klaus Blaum from the Mainz group moved in the same year. The experiment is now called the MPIK/UW-PTMS (Max-Planck-Institut für Kernphysik/University of Washington-Penning Trap Mass Spectrometer), or THE-Trap since the first aim is for a Tritium-Helium mass-ratio measurement.

1.2 The MPIK/UW-PTMS experiment

Achieving experimental uncertainties of 1 part in 10¹¹ in the mass determination, a number of fundamental questions and problems can be addressed with a Penning trap mass spectrometer. Examples include the most stringent test of special relativity [R⁺05], the redefinition of the kilogram via an atomic standard [RMM08, A⁺11] or matter-antimatter asymmetry tests [G⁺99]. For a broad review on the application of Penning traps to fundamental physics questions, see [BNW10]. But not only can mass measurements directly contribute to tests of fundamental physics, they often can deliver valuable input parameters for other experiments. The MPIK/UW-PTMS experiment in particular aims to contribute to the search for the electron-antineutrino mass, that has not yet been determined experi-

mentally (see section 2.1). The most stringent limits on this quantity can be set via studies of electrons emitted in the decay of ${}^3\text{H}$ (see section 2.2.3). An important input parameter here is the mass difference between ${}^3\text{H}$ (tritium) and the decay product ${}^3\text{He}$ (see section 2.2.4). The MPIK/UW-PTMS, also being called THE-Trap in this context, was set up as a dedicated experiment for the determination of the ${}^3\text{H}/{}^3\text{He}$ mass ratio. This means that a number of parts of the experiment and the experimental area were designed specifically for this single measurement (see chapter 4). This work summarizes on the commissioning experiments (see chapter 6) on the way to the ${}^3\text{H}/{}^3\text{He}$ mass ratio. Here, in particular measurements with the q/m mass doublet ${}^{12}\text{C}^{4+}$ are of interest, as almost all relevant parameters of the trap can already be determined in this ion species (see section 6.3).

2 The search for the neutrino mass

The neutrino is one of the basic particles of the Standard Model of Particle Physics. It is attributed to the leptonic sector and has a lepton number of $L = 1$. There are three generations of neutrinos (ν_e, ν_μ, ν_τ), corresponding to the three generations of charged leptons: the electron e^- , the muon μ^- and the tauon τ^- . The neutrino carries a weak, but no electric charge, and only interacts by the weak interaction and by gravitation. Its spin is $1/2$. The anti-particle of the neutrinos are the anti-neutrinos ($\bar{\nu}_e, \bar{\nu}_\mu, \bar{\nu}_\tau$). It should be noted that especially in the context with their mass (as discussed in section 2.1) neutrino and anti-neutrino properties are often mixed up, assuming perfect CPT-symmetry. So if not otherwise stated within this thesis work normally the anti-neutrino mass is meant, when referring to the term “neutrino mass”.

2.1 The neutrino mass

The existence of the neutrino (or to be more precise the anti-neutrino) was first postulated by Pauli in 1930 in an open letter. It was introduced to explain the continuous shape of the spectrum for nuclear β -decay

$$n \rightarrow p + e^- + \bar{\nu}_e \quad . \quad (2.1)$$

The first experimental observation of the anti-neutrino was carried out in 1956 by Cowan and Reines (the latter received the Nobel Prize in Physics in 1995) [CRH⁺56] by observing the inverse β -decay:

$$\bar{\nu}_e + p \rightarrow n + e^+ \quad . \quad (2.2)$$

At this time, the neutrino was widely believed to be massless, and indeed, the Standard Model only includes massless neutrinos [Sak58]. Though already in 1957 there were theoretical predictions that neutrinos could have a finite mass and hence undergo oscillations [Pon58], it took until 1998 when SuperKamiokande – by measuring oscillations between ν_μ and ν_τ – proved that neutrinos have a finite mass. However, oscillation experiments are not able to measure the absolute mass, but mass differences only. The oscillations between the neutrino generations are possible as the neutrino mass eigenstates are a non-trivial superposition of the flavour eigenstates. As the weak eigenstates are not equal to the mass eigenstates (the same is true for the quarks in the hadronic sector as well), the matrix describing their relation has non-zero off-diagonal elements:

$$\nu_\alpha = \sum_i U_{\alpha i} \nu_i \quad \alpha = (e, \mu, \tau) \quad . \quad (2.3)$$

In this case, oscillations are a straightforward consequence of standard quantum mechanics. Considering the two-dimensional case only, the matrix can be characterized by one mixing angle θ in the following way:

$$\begin{pmatrix} | \nu_e \rangle \\ | \nu_\mu \rangle \end{pmatrix} = \begin{pmatrix} \cos \theta & \sin \theta \\ -\sin \theta & \cos \theta \end{pmatrix} \begin{pmatrix} | \nu_1 \rangle \\ | \nu_2 \rangle \end{pmatrix} . \quad (2.4)$$

This means that the time evolution of the muon-neutrino produced at $t = 0$ for instance can be described as

$$| \nu_\mu(t) \rangle = -e^{-iE_1 t/\hbar} \sin \theta | \nu_1 \rangle + e^{-iE_2 t/\hbar} \cos \theta | \nu_2 \rangle . \quad (2.5)$$

Here E_1 and E_2 are the energies of the neutrino mass eigenstates. Then $| \nu_1 \rangle$ and $| \nu_2 \rangle$ can be replaced by inverting Eq. (2.4). The next step is to evaluate the time-dependent probability for the muon-neutrino to be in the electron-neutrino state $| \nu_e \rangle$. The result of this operation after some trigonometric transformations is

$$P_{\mu \rightarrow e} = | \langle \nu_\mu(t) | \nu_e \rangle |^2 = \sin^2 2\theta \cdot \left[\sin^2 \left(\frac{(E_2 - E_1)t}{2\hbar} \right) \right] . \quad (2.6)$$

This shows that there is a non-zero probability of flavour oscillation in case neither θ nor the time-dependent term are zero. To further evaluate the time-dependent term, it is assumed that relativistic neutrinos are observed (as it is the case in the experiments observing neutrino oscillations), where the total energy E_i is dominated by kinetic energy. This means that the momentum dominates the rest mass $p \gg m_i \cdot c$ and the energy of the observed neutrinos is $E \approx pc$. A Taylor expansion of the energy of the mass eigenstates yields $E_i \approx E + \frac{m_i^2 c^4}{2E}$. Inserting this into Eq. (2.6) yields:

$$P_{\mu \rightarrow e} = \sin^2 2\theta \cdot \left[\sin^2 \left(\frac{(m_2^2 - m_1^2)c^4 t}{4\hbar E} \right) \right] . \quad (2.7)$$

Hence, the existence of the neutrino oscillations proves that $\Delta m_{21}^2 = m_2^2 - m_1^2$ must be non-zero, implying the existence of a non-zero neutrino mass. In the three-neutrino case the matrix of Eq. (2.3) can be similarly parameterized (see e.g. [M⁺07]) with the three mixing angles θ_{12} , θ_{23} and θ_{13} ; and a phase α .

Many experiments have contributed (for an overview see [STV08]) to the knowledge of the neutrino mixing matrix, showing that neutrino mixing is a much more pronounced phenomenon than quark mixing. The angles θ_{12} , θ_{23} and the corresponding mass differences have been determined, only θ_{13} seems to be quite small and only upper limits could be derived. The resulting mass differences as accepted by the Particle Data Group [N⁺10] are

$$|\Delta m_{21}^2| = (7.59 \pm 0.20) \cdot 10^{-5} (\text{eV}/c^2)^2 \quad (2.8)$$

$$|\Delta m_{23}^2| = (2.43 \pm 0.13) \cdot 10^{-3} (\text{eV}/c^2)^2 . \quad (2.9)$$

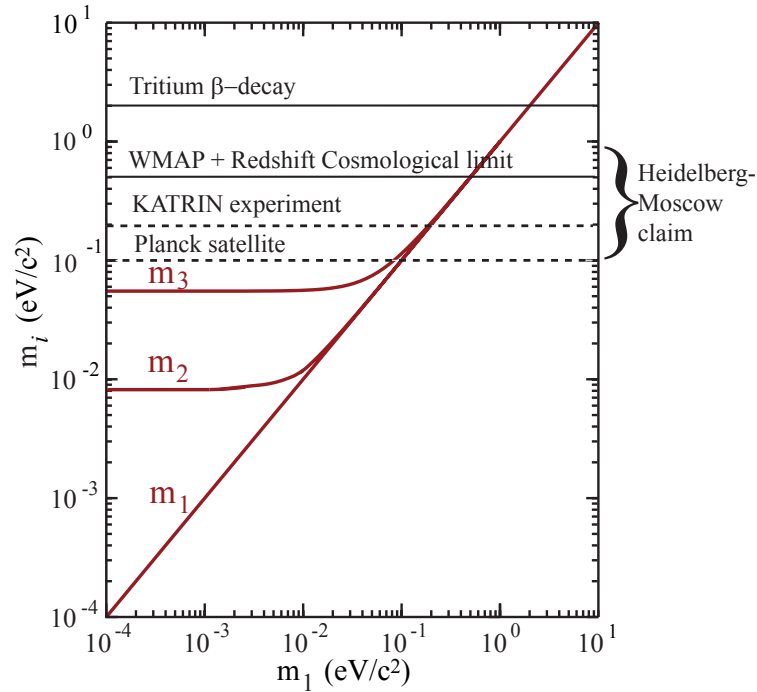


Figure 2.1: Neutrino mass limits as given by the experimental investigations. From the oscillation measurements, the mass differences are known. For masses higher than $0.1 \frac{\text{eV}}{c^2}$ the neutrino masses are basically degenerate. Experimental investigations of upper mass limits for the neutrino mass are indicated by the solid lines, the dashed lines show the expected sensitivity limits (95% C.L.) from future experiments. The claimed neutrino mass region of the Heidelberg-Moscow experiment is indicated by a bracket.

With these values as constraints for the total masses, different scenarios for the ordering and the scale of the neutrino masses are possible, as illustrated in Fig. 2.1. For squared neutrino masses significantly larger than Δm_{23}^2 , the neutrino masses are basically degenerate. At scales comparable to Δm_{23}^2 , the masses would be non-degenerate. While the experimental evidence that the neutrino must have a mass is commonly accepted, the mechanism how neutrinos gain their mass is still under discussion. One particular problem is that the mass is much smaller than the masses of all other elementary particles, which poses the question whether they undergo the same mechanism for mass formation. As the neutrino masses are not explained by the Standard Model of Particle Physics, understanding this mechanism is directly related to theories beyond the Standard Model. For a comprehensive review see [M⁺07].

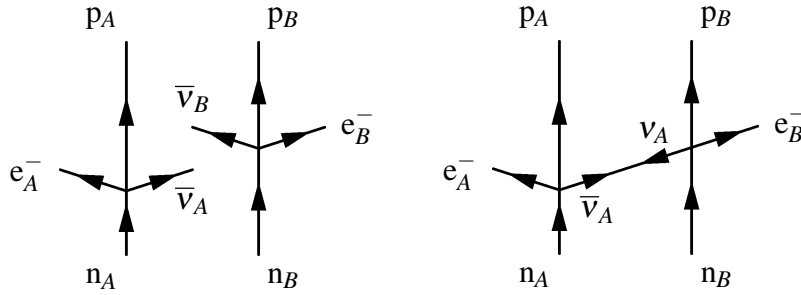


Figure 2.2: On the left side of the figure, double β -decay with the emission of two anti-neutrinos ($2\nu\beta\beta$) is illustrated (n stands for neutron, p for proton, e^- for electron and ν for neutrino). It resembles two independent β -decays. On the right side neutrino-less double β -decay ($0\nu\beta\beta$) is illustrated, where the anti-neutrino emitted from one β -decay changes its helicity and becomes its own anti-particle.

2.2 Approaches to determine the neutrino mass

Several complementary approaches to determine the electron anti-neutrino mass exist. Most of them are based on decay studies of radioactive nuclides, namely experiments on ordinary and double β -decay. Other limits on the neutrino mass are determined from cosmological observations. A short overview on the most prominent techniques is given. For a more detailed overview with particular emphasis on the tritium β -decay approach see [OW08]. Many of these approaches can profit from the ability of Penning trap mass spectrometry to provide mass differences as input parameters (see [DFC⁺01, RWMM07, R⁺08] and section 2.2.4).

It should also be noted that similar approaches to determine the electron neutrino mass exist, but have not yet reached the same level of uncertainty (see [N⁺10] for the present upper limit of around 300 eV). However, efforts to utilize electron capture processes (the inverse process to β -decay) to reach similar uncertainties as for the anti-neutrino case are under discussion ([E⁺10]), and again Penning trap mass spectrometry might be able to provide valuable input parameters for these measurements ([BNW10]).

2.2.1 Double beta-decay

Double β -decay is a rare decay-channel for nuclides, where ordinary β -decay is energetically forbidden. The nuclides then decay via two simultaneous β -decays. So far it was observed in 10 isotopes (^{48}Ca , ^{76}Ge , ^{82}Se , ^{96}Zr , ^{100}Mo , ^{116}Cd , $^{128,130}\text{Te}$, ^{130}Ba , ^{150}Nd and ^{238}U). The first indirect observation of double β -decay was made by geochemical methods in 1950 [IR50]. The first direct measurement was performed in 1987 [EHM87]. Two different kinds of double β -decay are in principle possible. In the two-neutrino double β -decay $2\nu\beta\beta$, as illustrated on the left side of Fig. 2.2, two anti-neutrinos are sent out and the pro-

cess just resembles two independent but simultaneous β -decays. So far only this process has been unambiguously measured. An alternative comes with the neutrinoless double β -decay ($0\nu\beta\beta$), illustrated on the right side of Fig. 2.2. The neutrino emitted in one decay is converted into an anti-neutrino, a process which is only possible if the neutrino carries a component of the opposite helicity, which means it possesses a mass. This also means that neutrinos are their own anti-particles and hence of Majorana type. The decay rate Γ for this process is proportional to the coherent sum of the neutrino masses, being called the effective neutrino mass m_{ee} :

$$\begin{aligned} \Gamma_{0\nu\beta\beta} &\propto \left| \sum_i U_{ei}^2 m_i \right|^2 \equiv m_{ee}^2 \\ &= |(m_1 \cos^2 \theta_{12} + m_2 e^{i\alpha_2} \sin^2 \theta_{12}) \cos^2 \theta_{13} + m_3 e^{i(\alpha_3+2\phi)} \sin^2 \theta_{13}|^2 \quad . \end{aligned} \quad (2.10)$$

Here, α_i are the Majorana phases which describe an additional rotation matrix added to the neutrino mixing formalism for the Majorana particle case and ϕ is a CP violating phase. The contribution of the neutrino masses to m_{ee} is intricate, in particular the knowledge of the Majorana phases is crucial for extracting them. In addition, other factors in the decay rate are also not known to high accuracy yet, one major part is the nuclear matrix element [ŠFR⁺08].

Experimentally, there are great challenges to cope with as the decay has an expected decay time of about 10^{26} years. On top there always is a large background by the competing process ($2\nu\beta\beta$ -decay), whose life-time is orders of magnitude shorter. Fortunately, the two decay modes have different signatures, $2\nu\beta\beta$ has a continuous electron energy spectrum, similar to ordinary β -decay, while $0\nu\beta\beta$ produces a sharp line. There is a subgroup of the Heidelberg-Moscow experiment that claims to have observed $0\nu\beta\beta$ with a life-time of $1.5 \cdot 10^{25}$ years in ^{76}Ge , resulting in $0.1 \text{ eV} < m_{ee}c^2 < 0.9 \text{ eV}$ [KDHK01]. As the claim is heavily disputed, new experiments are on the way to check the results [AEE08], one of them being the GERDA experiment [S⁺05], led by scientists from the Max-Planck-Institut für Kernphysik. An alternative approach to the double β -decay is the neutrinoless double electron capture process ($0\nu\text{ECEC}$), which has been subject to recent investigations in a Penning trap [E⁺11].

2.2.2 Cosmology

The question of the magnitude of neutrino masses plays an important role in cosmology as well, as their number in space is extremely high. Hence, they could contribute to the overall mass of the universe [LP06]. The Big Bang Model of Cosmology predicts a present-day background of 336 neutrinos/cm³. Assuming a total mass of $\sum m_i = 1\text{eV}/c^2$, which still would be compatible with the limits from direct mass measurements (see next section for more details), neutrinos would constitute about 2% of the total mass of the universe.

But not only is the neutrino mass of big interest as an input parameter to cosmological models, cosmology itself is also able to give limits on the neutrino mass. The leading

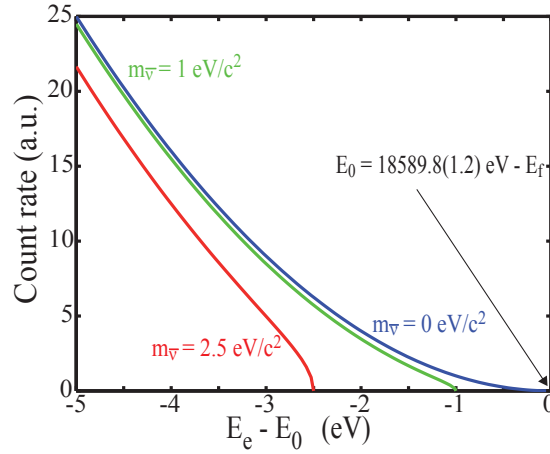


Figure 2.3: Spectrum of the electrons emitted in tritium β -decay towards the endpoint. Depending on the neutrino mass the spectrum is modified as can be seen in the different curves.

argument here is that neutrinos act as a mass/energy carrier in the structure formation of the universe. Depending on their mass and energy, this effect is more or less pronounced. The size of this effect can be measured by mapping fluctuations in the cosmic microwave background (CMB), which represents the structure of the universe 380000 years after the Big Bang, when the photons decoupled from matter. Together with refined cosmological models and a survey of the large scale structure (LSS) of the universe, where millions of galaxies were observed, it is then possible to give limits on the neutrino mass. As cosmological models usually include a large number of parameters the limits derived from the existing experimental determinations for CMB and LSS vary considerably, but are in agreement with the earth-based measurements by tritium β -decay and double β -decay. In a recent analysis [RVJM10] based on the latest data by WMAP combined with redshift data, the limit for the neutrino mass is given as $\sum m_i \leq 0.5 \text{eV}/c^2$; older limits based on WMAP data only report $\sum m_i < 1.3 \text{eV}/c^2$ [D⁺09]. The next generation experiment Planck, launched into space in 2009, is expected to be capable of improving these limits down into the 0.1 eV region or even below [HTW06]. However, it should still be kept in mind that the cosmological data are highly model-dependent and even changes on the 1% level in the total amount of matter in the universe can significantly shift the limits for the neutrino mass.

2.2.3 Ordinary beta-decay

The study of the electron spectrum of β -decay is the most straight-forward approach to determine the neutrino mass, and hence, has been studied by far the earliest of all techniques described here. Already Enrico Fermi proposed this technique in 1934, when he developed

his model of the nuclear β -decay [Fer34]. The starting point is Fermi's Golden Rule for the interaction rate Γ of scattering and decay processes

$$\Gamma = \frac{2\pi}{\hbar} |M_{fi}|^2 \cdot \rho(E) \quad , \quad (2.11)$$

where M_{fi} is the transition matrix element that characterizes the overlap of the wave functions of the final and initial state of the nucleus and $\rho(E)$ is the phase-space density, which is given by kinematics. To see the effect of neutrino mass on the shape of the spectrum, only the phase-space density needs to be analyzed further. It is given as [PRSZ04]

$$d\rho(E_0, E_e) = \frac{(4\pi)^2}{(2\pi\hbar)^6} p_e^2 \frac{dp_e}{dE_e} p_\nu^2 \frac{dp_\nu}{dE_0} V^2 dE_e \quad . \quad (2.12)$$

Here, E_0 is the total available energy, E_e the energy of the electron, p_e the momentum of the electron, p_ν the momentum of the neutrino and V the box normalization volume. Eq. (2.12) is easily derived from the phase space volume a specific particle fills: $4\pi p^2 dp \cdot V$. The box normalization volume has no influence on the final result of Eq. (2.11) as it is contained in the nuclear matrix element as well and cancels out. Utilizing the relativistic energy-momentum relation $E^2 = p^2 c^2 + m^2 c^4$ for both the electron and the neutrino yields the following equation:

$$p^2 dp = \frac{1}{c^2} p E dE = \frac{1}{c^3} E \sqrt{E^2 - m^2 c^4} dE \quad . \quad (2.13)$$

Inserting Eq. (2.13) into Eq. (2.12) and neglecting the recoil of the nucleus, which leads to $E_\nu = E_0 - E_e$ gives:

$$d\rho(E_0, E_e) = \frac{(4\pi)^2 V^2}{(2\pi\hbar c)^6} E_e \sqrt{E_e^2 - m_e^2 c^4} \cdot (E_0 - E_e) \sqrt{(E_0 - E_e)^2 - m_\nu^2 c^4} dE_e \quad . \quad (2.14)$$

From analyzing Eq. (2.14), it is clear that the spectrum is particular sensitive to the neutrino mass – or to be more correct to m_ν^2 – close to the endpoint energy E_0 . This is illustrated in the plot of the spectrum in Fig. 2.3.

A refined analysis of the basic kinematics and the inclusion of the transition matrix element M_{fi} can be found in a review paper of Otten and Weinheimer [OW08]. It includes the recoil of the daughter nucleus as well as its excited states and the possibility of neutrino mixing. However, all these effects do not change the basic dependence of Eq. (2.14) on the neutrino mass.

In principle the neutrino mass could be derived from every β -emitting isotope. However, almost all measurements were carried out on the decay of tritium:



Reasons for that are (see [OW08]):

1. The decay energy $E_0 \approx 18.6$ keV is one of the lowest of all β -decays. Therefore, the relative effect of the neutrino mass is high compared to other β -emitters.
2. The tritium β -decay is super-allowed, resulting in a short half-life of only 12.3 years. Hence, a large specific activity is available. Also the nuclear matrix element of super-allowed β -decays can be calculated accurately enough and do not depend on the electron energy.
3. As ${}^3\text{H}_2$ is among the simplest molecules, its final state spectrum can be calculated quantitatively does not contribute to the error of the neutrino mass so far.
4. Tritium is available as a side-product of heavy-water nuclear reactors and is thus available in significant amounts.

The only alternative to tritium investigated so far is the decay of ${}^{187}\text{Re}$, which can be measured in cryogenic bolometers. With this method the total energy of all participants of the decay except for the neutrino is measured directly. The so far best result from this approach originates from the MIBeta experiment [S⁺04] and yielded a limit to the neutrino mass of $m_\nu < 15$ eV/c². In the future MARE experiment, [M⁺06] it is planned to improve this limit down to 1 eV/c² being competitive to the current generation of tritium decay experiments.

But so far, the tritium-based experiments are the most sensitive approach for direct neutrino mass measurements. Their history dates back to the experiments of Curran and co-workers [CAC49] in the late 1940s, yielding an upper limit for the neutrino mass of 1 keV/c². Since then, a number of experiments have been carried out utilizing different techniques for both the tritium source and the spectrometer. For an overview on these measurements see [OW08]. The most recent experiments carried out are the Mainz [K⁺05] and the Troitsk [L⁺01] efforts, both based on a so-called MAC-E-filter, that will be explained in more detail in section 2.2.3. Both experiments reached similar sensitivity and the combined upper limit for the (anti-)neutrino mass is given as

$$m(\bar{\nu}_e) < 2 \text{ eV}/c^2 \quad (95\% \text{C.L.}) \quad . \quad (2.16)$$

This is somewhat higher than the other attempts described in the previous sections. However, the big advantage of this limit is that it is more or less independent from theoretical uncertainties and hence should be much more robust than the approaches described above.

The KATRIN experiment

As described in section 2.2, limits on the neutrino mass derived from double β -decay and cosmology have reached the sub-eV level. To countercheck these results, it is extremely important to push down the limits from the tritium β -decay measurements into this region as well. As this is accompanied by huge technological challenges [A⁺04] that will be partly discussed in this section, a huge collaboration centered around the former Mainz and

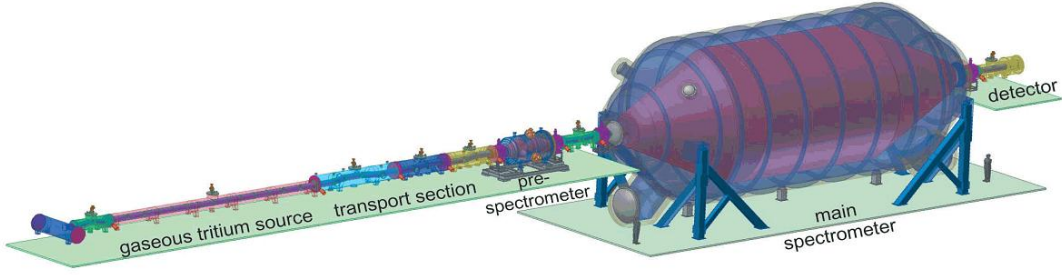


Figure 2.4: Drawing of the KATRIN setup. Taken from [A⁺04].

Troitsk groups was formed in order to perform the KARlsruhe TRitium Neutrino Experiment (KATRIN). The aim of the experiment is to improve the sensitivity to the neutrino mass by one order of magnitude to $m_{\nu_e} < 0.2 \text{eV}/c^2$. As $m_{\nu_e}^2$ is the observable of the experiment, this requires an improvement of the overall experimental sensitivity by a factor of 100.

The overall setup of KATRIN is depicted in Fig. 2.4. The tritium decay takes place in a windowless gaseous $^3\text{H}_2$ source in order to avoid charging of the source, which would spoil the energy resolution of the spectrometer. In order to prevent tritium molecules from diffusing into the main spectrometer a differential pumping system with some ion optics that bend the electron beam is utilized. Part of this differential pumping section contains Penning trap spectrometers that have been developed at the Max-Planck-Institut für Kernphysik [UDRL⁺09]. In these spectrometers, the broad-band FT-ICR (Fourier Transform-Ion Cyclotron Resonance) detection technique is utilized in order to monitor charged contaminations from the source region. Behind the differential pumping section, a pre-spectrometer is placed in the beamline in order to block the low-energy electrons, which could cause background problems in the main spectrometer.

The heart of the experiment is the main spectrometer, which is built in a 10 m diameter vacuum vessel. The spectrometer utilizes the well-established MAC-E-filter technique (Magnetic Adiabatic Collimation applied to an Electrostatic filter) of the Mainz and Troitsk experiments, but is scaled up by a factor of 10 in diameter and hence a factor of 100 in detection plane. The MAC-E-filter technique utilizes magnetic adiabatic collimation in combination with an electrostatic filter. The basic principle is illustrated in Fig. 2.5.

The electrons are produced inside a superconducting solenoid at a field strength B_S . As the magnetic field guides and focuses the electrons due to the cyclotron motion perpendicular to field lines, a solid angle of almost 2π is covered by this kind of spectrometer. The electrons travel towards the magnetic field minimum B_{min} at which the field maximum of the electrostatic filter is placed. In this process the cyclotron energy of the electrons is adiabatically transferred into longitudinal energy E_{\parallel} as long as the following condition is met:

$$\left| \frac{1}{B} \frac{dB}{dt} \right| \ll \omega_c = \frac{eB}{\gamma m} \quad , \quad (2.17)$$

where ω_c is the cyclotron frequency and γ the relativistic Lorentz factor, which is about 1 for the tritium decay. The exact amount of conversion of transverse cyclotron energy E_{\perp} into longitudinal energy E_{\parallel} can be determined from electrodynamics. The orbital magnetic moment

$$\mu = \frac{e\omega_c R^2}{2} \quad (2.18)$$

is a constant of motion and can be expressed as

$$\mu = \frac{E_{\perp}}{B} = \text{const.} \quad (2.19)$$

as well. This means that the transverse energy E_{\perp} of the electrons is reduced in the following way due to the change in magnetic field:

$$E_{\perp,\min} = \frac{B_{\min}}{B_S} E_{\perp,S} = \frac{B_{\min}}{B_S} \sin^2 \alpha \cdot E = \frac{R_S^2}{R_{\min}^2} \sin^2 \alpha \cdot E \quad (2.20)$$

Here E is the total energy of the electrons, α is the angle under which the electrons leave the source and R_S and R_{\min} are the cyclotron radii at the source and the radii at the minimum position. From Eq. (2.20) it is clear that the bigger the analyzing plane and the smaller the magnetic field B_{\min} , the more energy is transferred into the longitudinal direction. This is important as only the longitudinal energy is analyzed in the electrostatic filter. The relative width of the filter is determined by the extreme values of $\alpha = 0$ and $\alpha = \pi/2$ to be

$$\frac{\Delta E}{E} = \frac{B_{\min}}{B_S} \quad (2.21)$$

For a more detailed discussion on the MAC-E-filter, see [P⁺92].

The KATRIN MAC-E-filter has a ratio of $\frac{B_S}{B_{\min}} \approx 20000$, resulting in a energy resolution of $\Delta E = 0.93$ eV near the tritium β -decay endpoint E_0 . Finally, the electrons that had sufficient energy to pass the MAC-E-filter are detected by a 148 pixel PIN diode detector that will give spatial information, too. The KATRIN experiment is under construction right now and it is planned to start the data-taking in 2012. To accumulate a sufficient amount of statistics the experiment will have to run for about 5 years.

2.2.4 Penning trap mass spectrometry

As already mentioned in the previous sections, a number of experiments for the determination of the neutrino mass is based on studies of nuclear decays. Here in particular, the total available energy given by the Q -value of these decays plays an important role. The Q -value is defined via the energy difference between two different states, that is given as their mass difference. Hence, it is accessible by Penning trap mass spectrometry if one assumes that Einstein's famous equation [Ein05]

$$E = mc^2 \quad (2.22)$$

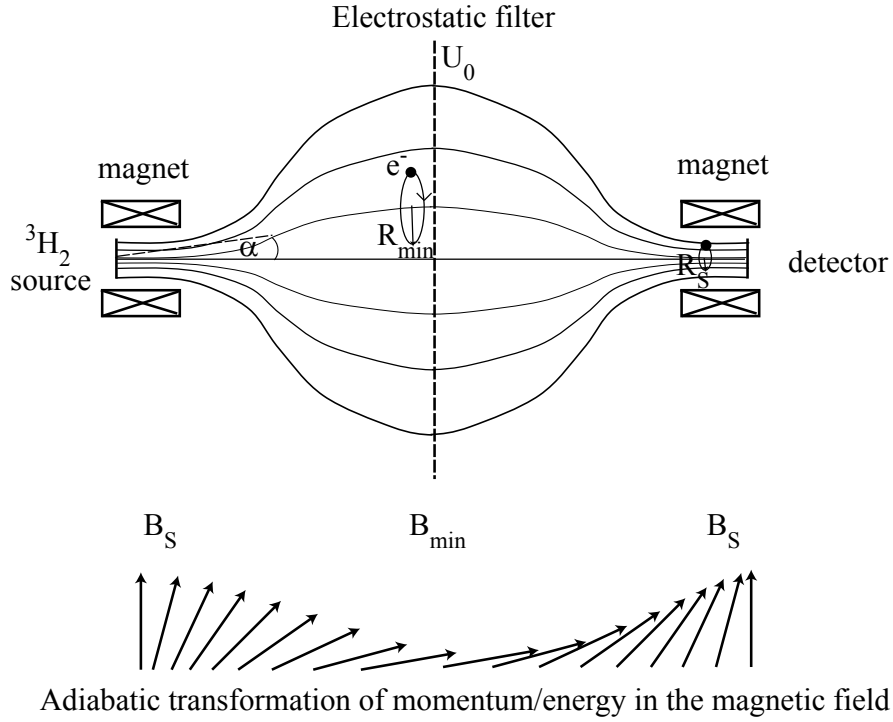


Figure 2.5: Schematic drawing of a MAC-E-filter. The arrows represent the momentum of the electrons. In the strong magnetic field B_S most of the total kinetic energy is in the transverse direction E_{\perp} . When the electrons travel through the magnetic field gradient towards the magnetic field minimum B_{min} , a large fraction of E_{\perp} is converted into longitudinal energy E_{\parallel} that is analyzed by the filter potential U_0 .

is correct. Actually, Penning trap mass spectrometry contributed to the most sensitive test of this relation so far [R⁺05] and confirmed it on a 1 part in 10^7 level. The most precise way to determine the mass difference is to measure the absolute mass of either the mother or the daughter nuclide and their mass ratio:

$$m_f - m_i = m_f \left(1 - \frac{m_i}{m_f} \right) = m_f(1 - R) \quad . \quad (2.23)$$

Here, m_f is the mass of the daughter (final state) and m_i the mass of the mother (initial state) nuclide. In order to determine an absolute mass in Penning trap mass spectrometry, the mass of the ion-of-interest has to be related to the atomic mass standard, which is defined by the atomic mass unit

$$m_u = \frac{1}{12} m(^{12}\text{C}) \quad . \quad (2.24)$$

This is done by measuring the mass ratio of the ion-of-interest and a reference ion (preferably a ^{12}C ion, a carbon cluster or an ion whose mass is determined to much higher accu-

racy than desired for ion-of-interest). The mass ratio of m_i and m_f is measured by taking the two ions-of-interest as references to each other. As usually mass doublets are measured

$$m_f - m_i \ll m_i, m_f \Leftrightarrow R \approx 1 \quad (2.25)$$

a lot of systematic shifts in the mass ratio $R = m_i/m_f$ are strongly suppressed. However, Penning trap mass spectrometry has to pay a price, when Q -values are to be determined: the relative uncertainty in the mass ratio has to be significantly smaller than the final uncertainty in the Q -value. This can be seen, when analyzing the relative uncertainty, assuming uncorrelated errors in m_f and R

$$\frac{\Delta(m_f - m_i)}{m_f - m_i} = \sqrt{\left(\frac{\Delta m_f}{m_f}\right)^2 + \left(\frac{\Delta R}{R-1}\right)^2} \quad (2.26)$$

In Eq. (2.26) $R-1$ can be a very small quantity due to Eq. (2.25) and hence, $\Delta R/R$ must be known to much higher accuracy than $\Delta m_f/m_f$. In the case of tritium, this effect is particularly big due to the very small mass difference of only 18.6 keV between ${}^3\text{H}$ and ${}^3\text{He}$. The mass of ${}^3\text{He}$ is already known on the 1 part in 10^9 level [NFB⁺06] and hence does not contribute to Eq. (2.26) at the desired level of precision. This means that the total uncertainty can be written as

$$\frac{\Delta(m_f - m_i)}{m_f - m_i} \approx \frac{\Delta R}{R-1} \quad (2.27)$$

As $R-1 = 6.6 \cdot 10^{-6}$ an uncertainty of one part in 10^{11} , which is nowadays achievable in Penning trap mass spectrometry, will result in a relative uncertainty of about 1 part in 10^6 in the Q -value.

Even though Penning trap mass spectrometry can contribute to a number of experiments related to neutrino physics, here only tritium β -decay will be treated. For an overview on the role of Penning traps in neutrino physics see [BNW10].

To analyze the contribution of Penning trap physics to the neutrino mass determination, it is necessary to clarify the exact relation between the quantity that is accessible to Penning trap mass spectrometry $\Delta m({}^3\text{H}^+, {}^3\text{He}^+) = m({}^3\text{H}^+) - m({}^3\text{He}^+)$ and the relevant experimental parameter in the β -decay experiments E_0 . Here, it is also noteworthy that most experiments utilize molecular tritium ${}^3\text{H}_2$ as a source, which has to be taken into account in these considerations. The different energies are illustrated in Fig. 2.6. The standard quantity to describe the energy released in nuclear decays is the Q -value. In the case of β^- -decay it is defined as

$$(A, Z) \rightarrow (A, Z+1)^+ + e^- + \bar{\nu}_e + Q \quad (2.28)$$

This total available energy Q is shared between the reactants in the following way:

$$Q = E_e + E_\nu + E_{\text{recoil}} + E_f \quad (2.29)$$

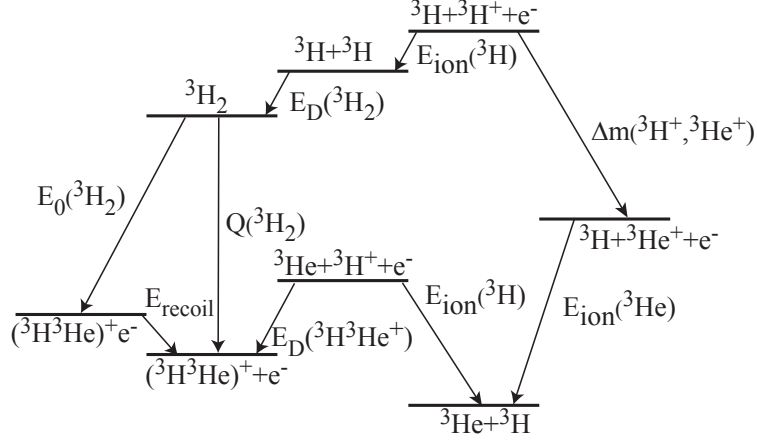


Figure 2.6: The different energies relevant for the tritium β -decay in a gaseous source. E_D depicts a dissociation energy, E_{ion} an ionization energy.

Here E_{recoil} is the recoil energy of the daughter nucleus, E_e the kinetic energy of the electron, E_ν the kinetic energy of the anti-neutrino and E_f the final state of excitation of ${}^3\text{He}$. The endpoint energy E_0 , which was already discussed in section 2.2.3, is defined for the case of the daughter being in the absolute ground state $E_f = 0$ as

$$E_0 = Q - E_{\text{recoil}} = E_e + E_\nu \quad . \quad (2.30)$$

The mass difference determined by Penning trap mass spectrometry is

$$\begin{aligned} \Delta m({}^3\text{H}^+, {}^3\text{He}^+) &= m({}^3\text{H}^+) - m({}^3\text{He}^+) \quad (2.31) \\ &= (m({}^3\text{H}) - m(e^-) + \frac{1}{c^2} \cdot E_{\text{ion}}({}^3\text{H})) - (m({}^3\text{He}) - m(e^-) + \frac{1}{c^2} \cdot E_{\text{ion}}({}^3\text{He})) \\ &= m({}^3\text{H}) - m({}^3\text{He}) + \frac{1}{c^2} \cdot (E_{\text{ion}}({}^3\text{He}) - E_{\text{ion}}({}^3\text{H})) \quad . \end{aligned}$$

Given that the tritium decay does not occur from an atomic source but from a molecular sample of ${}^3\text{H}_2$ into $({}^3\text{He}^3\text{H})^+$, it is also necessary to take the dissociation energies $E_D({}^3\text{H}_2)$ and $E_D({}^3\text{He}^3\text{H})$ into account.

Together this results in the following relation between $E_0({}^3\text{H}_2)$ and $\Delta m({}^3\text{H}^+, {}^3\text{He}^+)$:

$$E_0({}^3\text{H}_2) = \Delta m({}^3\text{H}^+, {}^3\text{He}^+)c^2 + E_D({}^3\text{H}_2) - E_D({}^3\text{He}^3\text{H}) - E_{\text{ion}}({}^3\text{He}) - E_{\text{recoil}} \quad . \quad (2.32)$$

Having clarified the general relation between the quantities measurable with KATRIN and in Penning traps, the question remains how KATRIN can benefit from an independent Q -value measurement. This question has been addressed in detail in a paper of Otten, Bonn and Weinheimer [OBW06] and the results will be summarized here. At first sight, e.g. at Eq. (2.14), it appears that tritium β -decay experiments, like KATRIN, can use an

external E_0 -determination together with their determined endpoint to extract the neutrino mass directly. Unfortunately, the situation is not quite so simple. Close to the endpoint of the spectrum the count rate approaches in principle zero and even within the last 10 eV only a fraction of $2 \cdot 10^{-10}$ of the total number of decays are accumulated. So for a sub-eV neutrino mass determination the expected background count rate of 10^{-2} counts per second in the KATRIN main spectrometer exceeds the actual number of counts from β -decay close to the endpoint. In addition, several effects, such as the final state spectrum of the daughter molecule and charging of the source region, can shift the endpoint of the β -spectrum. Therefore, a more refined fitting mechanism is necessary in order to determine m_ν . Three parameters need to be determined: the squared neutrino mass m_ν^2 , the endpoint energy E_0 and the background count rate b . The total count rate for a sharp electrostatic filter, such as KATRIN, can be determined starting from first principle (Eq. (2.11)) to be [OW08]

$$r(\varepsilon) = A \cdot \sum_i |U_{ei}|^2 (\varepsilon^2 - m_i^2 c^4)^{3/2} + b = s + b \quad , \quad (2.33)$$

where $\varepsilon := E_0 - E_e$, s is the rate of real signals and A the energy-independent characteristic amplitude that incorporates factors such as the total number of decays, the nuclear matrix element, etc.. Eq. (2.33) and Fig. 2.3 show that the neutrino mass can be determined from a fit to its signature above the endpoint as well. For practical purposes, it is also clear that s must be larger than b , which requires $\varepsilon \gg m_s c^2$, where m_s is the sensitivity to the neutrino mass. This allows to develop Eq. (2.33) into

$$r(\varepsilon) = A \left(\varepsilon^3 - \frac{3}{2} \varepsilon \sum_i |U_{ei}|^2 m_i^2 \right) + b \quad . \quad (2.34)$$

In the following $m_\nu^2 := \sum_i |U_{ei}|^2 m_i^2$ will be utilized.

Analyzing Eq. (2.34) shows that the region of optimum sensitivity for the neutrino mass is limited on both sides of the energy spectrum. Towards the high-energy side, the background count rate will dominate, while towards the low-energy side the ε^3 -term is suppressing the m_ν^2 -term. Optimum sensitivity is expected at a count rate of $s(\varepsilon_{\text{opt}}) = 2b$ [Ott94]. Optimum sensitivity for E_0 on the other hand is given more towards the low-energy side, as the effect of the finite neutrino mass basically vanishes due to the ε^3 -term. The background rate b obviously can be determined best at an energy above E_0 . These different regions are illustrated in Fig. 2.7.

As a next step, it is possible to analyze how an external endpoint E_0 instead of the fit would influence the uncertainty of the neutrino mass. From Eq. (2.34) the uncertainty due to E_0 can be derived to be

$$\Delta m_\nu^2 = \frac{\partial r / \partial E_0}{\partial r / \partial m_\nu^2} \Delta E_0 = \frac{2(E_0 - E_e) \Delta E_0}{c^4} \quad . \quad (2.35)$$

Here E_e is the electron energy that the MAC-E-filter is adjusted to. Eq. (2.35) shows that an external E_0 suffers from an upscaling with the factor $2(E_0 - E_e)/c^4$, which is determined

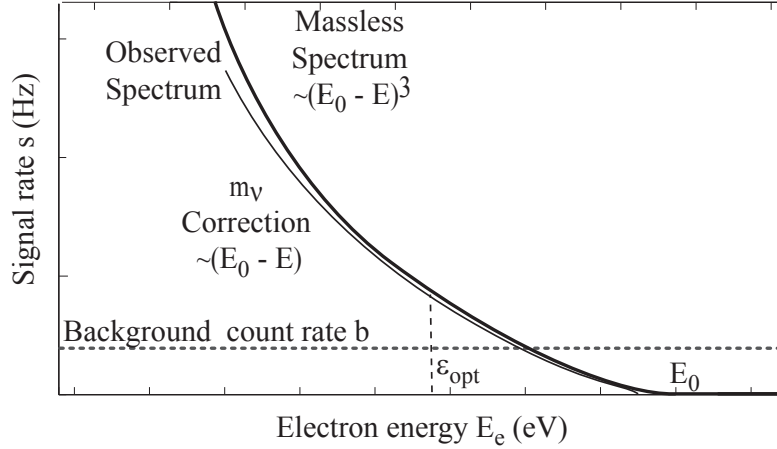


Figure 2.7: The spectrum of tritium β -decay electrons around the endpoint. Three regions contain different information on the spectrum. Close to the endpoint at ϵ_{opt} the spectrum is sensitive to m_ν , further below the endpoint to E_0 and above the endpoint to b .

by the background of the spectrometer as stated in the discussion above. Combining the best E_0 -measurement from SMILETRAP, that yielded an uncertainty of $\Delta E_0 = 1.2$ eV [NFB⁺06] with the Mainz neutrino mass experiment value of $\epsilon_{\text{opt}} = 15$ eV results in a contribution of $\Delta m_\nu^2 = 36$ eV²/c⁴, which is a factor of 20 larger than the result from “internal” fitting [K⁺05]. Correspondingly, for the Mainz neutrino mass experiment, an external $\Delta E_0 \approx 50$ meV would have been needed in order to improve the limits on the neutrino mass. Additional complication is added by the electron energy E_e , and hence the electrostatic potential of the filter U needs to be known on the same level as E_0 in order to be useful for the external E_0 -measurement. For KATRIN the situation is even more challenging as $\epsilon_{\text{opt}} \approx 3$ eV is expected. Together with an improved statistical limit this results in the need for $\Delta E_0 \approx 5$ meV, which also can be underlined in a Monte Carlo simulation of the data analysis [OW08]. From Eq. (2.26) it can be concluded that Penning trap mass spectrometry would have to reach the 1 part in 10^{12} level in order to contribute directly to the neutrino mass determination.

However, an improved E_0 does not only bring a benefit to KATRIN in the neutrino mass determination. It would, probably be even more important to also provide a test of the KATRIN data, as KATRIN derives E_0 as well. This is of extreme importance as KATRIN most likely is the only experiment to directly measure m_ν on the sub-eV scale for quite a while. So hidden systematics can be excluded if the KATRIN E_0 agrees with an external E_0 on the 100 meV scale. This would correspond to a few parts in 10^{11} uncertainty in the ${}^3\text{H}/{}^3\text{He}$ mass ratio, which is more realistic to be reached soon by Penning trap mass spectrometry. For the Mainz measurements, the SMILETRAP result served the same purpose and could exclude systematic deviations of more than 1 eV.

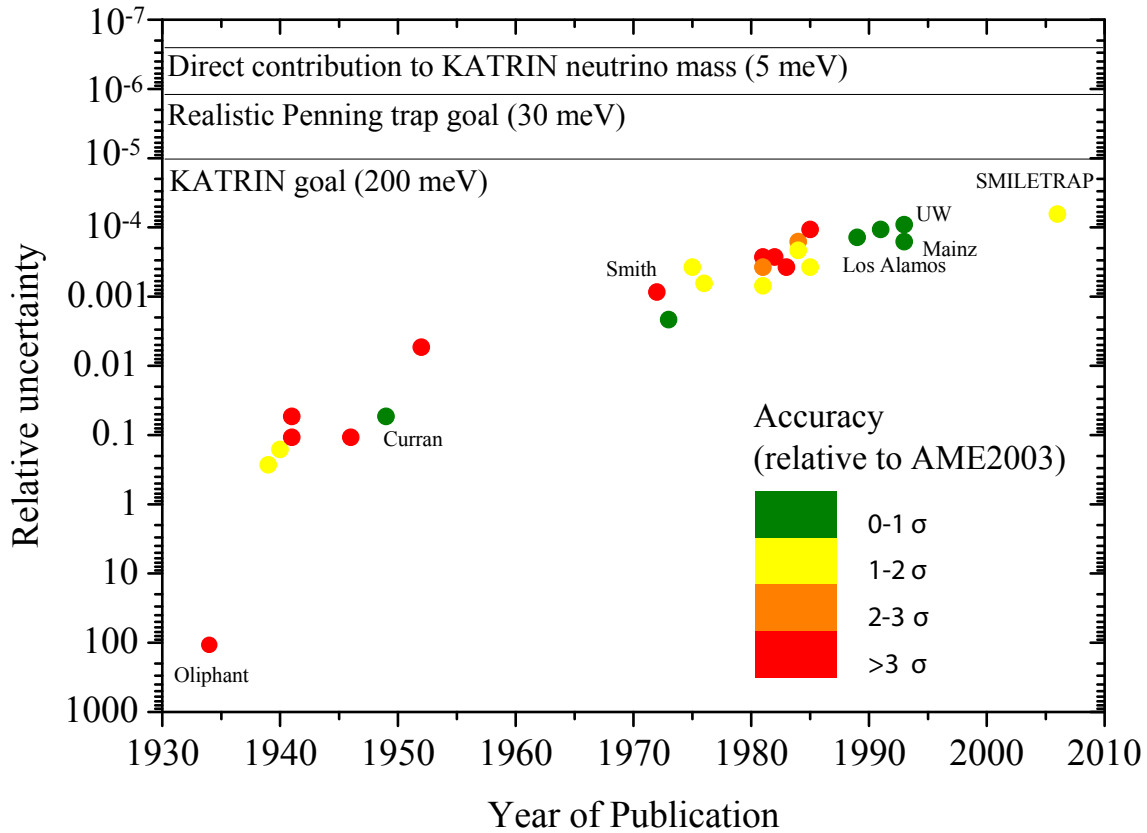


Figure 2.8: Development of the ${}^3\text{H}/{}^3\text{He}$ mass difference uncertainty over time. The relative uncertainty compares the error bars of the experiment with the absolute value. The color-coding gives the accuracy relative to the AME2003 value of 18591(1) eV. Here, relative accuracy means how many of its own error bars σ the experiment deviates from the AME2003 value.

***Q*-value measurements**

As already mentioned in the previous section, E_0 or the corresponding mass difference $\Delta m({}^3\text{H}^+, {}^3\text{He}^+)$ is an important parameter in the determination of the neutrino mass. Not surprisingly, many different experiments that are summarized in Fig. 2.8, have aimed to determine this quantity in the past.

Here, two main experimental approaches can be distinguished: Weighing the mass difference by means of mass spectrometric methods and measuring the energy of the β -electrons with a variety of experimental methods. The first determination dates back to 1934 and coincides with the discovery of ${}^3\text{H}$ and ${}^3\text{He}$ by Oliphant [OHR34]. The value is taken from the kinematics of neutron bombardment on a hydrogen target and suggests that $\Delta m({}^3\text{H}, {}^3\text{He}) \approx 2 \text{ MeV}$, which is orders of magnitude from the real value. After that discovery, several studies in the 1940s were published [WW46], all yielding results be-

tween 10 and 20 keV and errors on the 1 keV scale. In 1949, Curran published a value of 18(1) keV [CAC49], which is both precise and accurate (as compared to the most recent measurements) by using an electrostatic deflector for the β -electrons. Further improvement of the precision (but not the accuracy) was achieved by Langer in 1952 with a value of 17.95(10) keV [LM52] by using a magnetic spectrometer for observing the β -decay. After that it took until the 1970s before further improvements into the 10 eV region were published, which were reviewed by Audi [AGG85]. In particular noteworthy here are the measurements of Smith [SW75] that utilized RF mass spectrometry (see section 1.1.1) and provided a first mass spectrometric approach as an alternative to the observation of the β -spectrum. In the 1980s also another mass spectrometric approach, now related to traps was taken, the FT-ICR-technique, where the cyclotron motion of a cloud of ions in a cell is measured by image currents that are Fourier transformed [L⁺85]. The first utilization of a Penning trap mass spectrometer dates back to 1993, when Van Dyck achieved a value of 18590.0(1.7) eV with the original UW-PTMS [VDFS93]. At about the same time, the β -spectrometers at Mainz and Los Alamos published values with slightly higher uncertainties, that are in good agreement with Van Dyck's result. The latest and most accurate result on E_0 also stems from Penning trap mass spectrometry and was achieved by the SMILETRAP experiment in 2006 [NFB⁺06]. A value of 18589.8(1.2) eV was published, which again is in good agreement with the previous determinations. For the SMILETRAP experiment, it is in particular noteworthy that the method is somewhat complementary to the UW-PTMS measurement, where continuous non-destructive monitoring of a single ion was utilized. SMILETRAP instead used the time-of-flight ion-cyclotron-resonance (TOF-ICR) method, a destructive method, where the time-of-flight of ions ejected from the trap as a function of the excitation frequency is measured. The world average as taken from the atomic mass evaluation of 2003 [AWT03] is given as 18591(1) eV, not taking into account the later SMILETRAP value.

Reviewing these results in the context of the demands on E_0 of KATRIN (at most 100 meV uncertainty), it is clear that another measurement of E_0 is urgently needed. So far, Penning trap mass spectrometry seems to be the only technique that is able to provide measurements with this uncertainty. Therefore, the MPIK/UW-PTMS experiment, that will be described in detail throughout this thesis was developed and aims at meeting the KATRIN requirements.

3 Penning trap theory

The motion of a single ion in an ideal Penning trap is an example of a harmonic oscillator. Hence, it can be described analytically for most parts. In this chapter, the basic ion motion as well as specific features needed to understand the discussion in the next chapters will be described. An excellent review on the topic is given in the article of Brown and Gabrielse [BG86]. A more specific discussion of the theory related to the UW-PTMS mass measurement can be found in the theses of Farnham and Van Liew [Far95, VL04].

3.1 Electrostatics of the Penning trap

In order to perform high-precision measurements on single ions it is important to store them in a well-defined volume. The Earnshaw theorem [Ear42] states that a purely electro- or magnetostatic solution to this problem is not possible. One possible solution is the superposition of a strong magnetic field with an electrostatic field as it is realized in the Penning trap. The magnetostatic part of the problem is to produce a homogeneous magnetic field strength $\vec{B}(\vec{r})$. The basic equation that needs to be solved is

$$\vec{B}(\vec{r}) = \frac{\mu_0}{4\pi} \int_V \vec{j}(\vec{r}') \times \frac{\vec{r} - \vec{r}'}{|\vec{r} - \vec{r}'|^3} d^3 r' \quad , \quad (3.1)$$

where $\vec{j}(\vec{r}')$ is the current density that creates the magnetic field. Usually, it is solved numerically for the design of complicated magnet systems such as the superconducting magnets used in Penning trap mass spectrometry [GT88, VDFZS99]. For the discussion of the ideal Penning trap it will be assumed that the magnetic field is $\vec{B}(\vec{r}) = B\hat{z}$.

The basic equation for the electrostatics of the Penning trap is the Laplace equation

$$\Delta\Phi(x, y, z) = 0 \quad , \quad (3.2)$$

where $\Phi(x, y, z)$ is the potential. One possible solution to this equation that yields harmonic motion is

$$\Phi(x, y, z) = \Phi_0 + (ax^2 + by^2 + cz^2) \quad \text{with} \quad a + b + c = 0 \quad . \quad (3.3)$$

Choosing $a = b = -c/2$ and transforming to cylindrical coordinates (ρ, z) yields

$$\Phi(\rho, z) = \Phi_0 - c \left(\frac{\rho^2}{2} - z^2 \right) \quad . \quad (3.4)$$

The equipotential lines of this field configuration are hyperbolas as

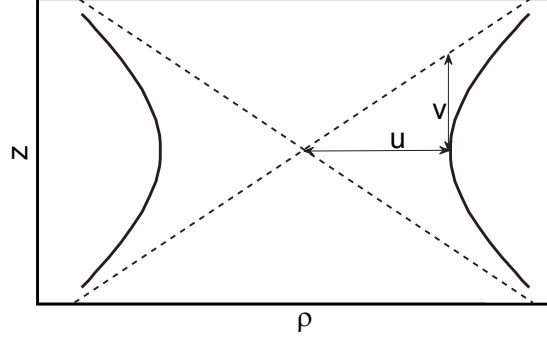


Figure 3.1: General definition of a hyperbola. The dashed lines are called the asymptotes of the hyperbola.

$$\Phi(\rho, z) = \text{const.} = \frac{\rho^2}{\sqrt{2}^2} - \frac{z^2}{\sqrt{1}^2} \quad (3.5)$$

and the general equation for a hyperbola is given as

$$\pm 1 = \frac{\rho^2}{u^2} - \frac{z^2}{v^2}, \quad (3.6)$$

where u and v are defined as illustrated in Fig. 3.1. For a Penning trap, the two hyperbolas (one oriented in the z -direction and one oriented in the ρ -direction) are defined by the constants z_0 and ρ_0 , which can be chosen independently as long as Eq. (3.5) is fulfilled for each of the electrodes. One popular choice is the asymptotically symmetric trap, where hyperbolas with identical asymptotes are used in the two directions and $\rho_0 = \sqrt{2}z_0$. Another advantageous design is the orthogonal trap [Gab83], where $\rho_0 \approx 1.16z_0$. This design allows to cancel unwanted effects of compensation electrodes in the imperfect Penning trap (see section 3.4.1). It should also be stated that Penning traps are three-dimensional objects and hence the actual electrodes are hyperbola of revolution.

Inserting boundary conditions for the electrostatic potential $\Phi(0, z_0) = 0$ and $\Phi(\rho_0, 0) = -V_0$, where $-V_0$ is the voltage applied to the ring, allows to solve for Φ_0 and c yielding

$$\Phi(\rho, z) = -\frac{V_0 z_0^2}{z_0^2 + \rho_0^2/2} + V_0 \frac{z^2 - \frac{1}{2}\rho^2}{z_0^2 + \rho_0^2/2}. \quad (3.7)$$

In the following $d = \frac{1}{2}\sqrt{2z_0^2 + \rho_0^2}$ will be defined as the characteristic trap dimension. The dimensions of a Penning trap are illustrated in Fig. 3.2.

3.2 Harmonic ion motion in a Penning trap

In order to investigate and manipulate ions in a Penning trap, it is important to understand their basic motion. This section will concentrate on the motion of a single ion. However,

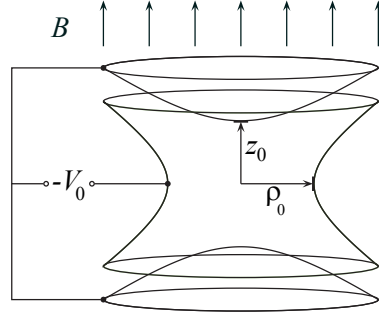


Figure 3.2: Schematic drawing of a Penning trap. The characteristic dimensions are z_0 and ρ_0 . The magnetic field is applied along the z -axis. Courtesy of Jochen Ketter.

it should be noted that ion clouds and contaminations with other ions are an important complication of the experimental procedures, and hence possible ways to get rid of them will be discussed in section 6.2.3. For a theoretical treatment of cloud/plasma effects in a Penning trap see [MGW05].

Ions in an ideal Penning trap undergo harmonic motions. As the energies of the particles for the experiment discussed in this thesis are extremely low, relativistic effects will be neglected for now in the discussion of the ideal Penning trap (relativistic effects on the axial motion are discussed in section 3.4.1). The starting point of the calculations is the well-known Lorentz force

$$\vec{F} = m\ddot{\vec{r}} = q[\vec{E} + \dot{\vec{r}} \times \vec{B}] \quad , \quad (3.8)$$

where q is the charge and m the mass of the ion. The electric field is given by differentiating Eq. (3.7) as

$$\vec{E} = -\vec{\nabla}\Phi = -\left(\frac{V_0}{d^2}z\hat{z} - \frac{V_0}{2d^2}\rho\hat{\rho}\right) \quad . \quad (3.9)$$

The magnetic field is defined to be $\vec{B} = B\hat{z}$. Eq. (3.8) in this case separates into an axial and a radial part. The axial part can be written as

$$\ddot{z} + \frac{qV_0}{md^2}z = 0 \quad . \quad (3.10)$$

This is a simple equation of harmonic motion and can be solved with the ansatz $z = A_z e^{i\omega t}$. The resulting axial frequency is

$$\omega_z = \sqrt{\frac{qV_0}{md^2}} \quad . \quad (3.11)$$

The radial equation of motion can be written as

$$\ddot{\vec{\rho}} = \frac{qV_0}{2md^2}\vec{\rho} + \frac{q}{m}B\dot{\vec{\rho}} \times \hat{z} \quad . \quad (3.12)$$

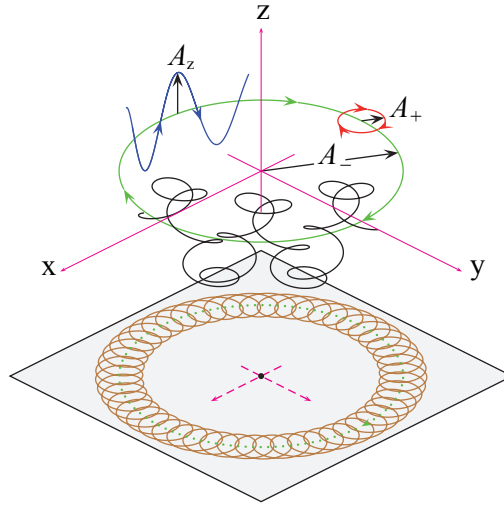


Figure 3.3: The three eigenmotions in a Penning trap: The modified cyclotron motion in red, the magnetron motion in green and the axial motion in blue. A two-dimensional projection of the motion is shown at the bottom. Courtesy of Jochen Ketter.

Making the ansatz for a circular motion $\dot{\vec{\rho}} = \vec{\omega} \times \vec{\rho}$ with $\vec{\omega} = \omega \hat{z}$ yields

$$\omega^2 \vec{\rho} + \omega \omega_c \vec{\rho} + \frac{1}{2} \omega_z^2 \vec{\rho} = 0 \quad , \quad (3.13)$$

where

$$\omega_c = \frac{qB}{m} \quad (3.14)$$

is the free-space cyclotron motion. The non-trivial solution is

$$\omega_{+/-} = -\frac{1}{2} \left(\omega_c \pm \sqrt{\omega_c^2 - 2\omega_z^2} \right) \quad . \quad (3.15)$$

This corresponds to two circular motions, the fast modified cyclotron motion ω_+ and the slow magnetron motion ω_- . The minus sign is reflecting the direction of the motion. In the following it will be ignored. Eq. (3.15) also includes a stability criterion for the motion in the Penning trap. In order for the square-root to be real, $\omega_c > \sqrt{2}\omega_z$ needs to be fulfilled. This results in

$$\frac{q}{m} > \frac{2V_0}{B^2 \cdot d^2} \quad . \quad (3.16)$$

For typical conditions in this trap $q/m > 0.015$ e/u needs to be fulfilled.

Combining the three eigenmotions calculated above the way how to measure a mass in a Penning trap also becomes evident (as will be discussed in section 3.6):

$$\omega_z^2 + \omega_+^2 + \omega_-^2 = \omega_c^2 = \left(\frac{qB}{m}\right)^2 . \quad (3.17)$$

The vector of motion is given as

$$\vec{r} = \left(\vec{A}_z \cdot e^{i(\omega_z t + \phi_z)} + \vec{A}_+ \cdot e^{i(\omega_+ t + \phi_+)} + \vec{A}_- \cdot e^{i(\omega_- t + \phi_-)} \right) . \quad (3.18)$$

Here \vec{A}_z , \vec{A}_+ , \vec{A}_- are the motional amplitudes and ϕ_z , ϕ_+ and ϕ_- are the corresponding phases. A schematic representation of the three eigenmotions in an ideal Penning trap is given in Fig. 3.3. For typical conditions in a Penning trap there is a clear hierarchy of the three eigenfrequencies: $\omega_+ \gg \omega_z \gg \omega_-$. Typical values for MPIK/UW-PTMS are given in Tab. 3.1. Another interesting feature of the motion can be seen, when calculating the energy of the motions:

$$E_{\text{total}} = E_{\text{pot}} + E_{\text{kin}} = \frac{1}{2}m [A_z^2 \omega_z^2 + A_+^2 (\omega_+^2 - \omega_+ \omega_-) + A_-^2 (\omega_-^2 - \omega_+ \omega_-)] . \quad (3.19)$$

As $\omega_- < \omega_+$, this means that the magnetron motion is in principle unstable as it has negative energy. A more detailed analysis shows that most of the energy of the magnetron motion is potential energy: The ion slowly travels around a potential hill. As long as no additional energy is added to the magnetron motion, it will be basically stable. Fortunately, there is only very little interaction of the magnetron motion with the outside world and so the life-time of this motion is significantly longer than any experimental observation time in practice.

3.3 Axial ion detection

A number of different detection techniques have been developed for ions in a Penning trap. They are usually highly adapted to the specific needs of the trap systems. E.g. mass measurements on short-lived radionuclides, as they are carried out at ISOLTRAP [M⁺08], need a method to cope with limited observation time, which is provided by the destructive TOF-ICR method [G⁺07], where the ion's excitation energy is monitored by its time of flight leaving the magnet. A non-destructive method for detection is the FT-ICR (Fourier Transform-Ion Cyclotron Resonance) technique [K⁺09], where a transient of the induced image charge in the ring electrodes of the Penning trap is Fourier transformed in order to determine the modified cyclotron frequency. However, for the highest precision mass spectrometry so far, only axial ion detection techniques, based on non-destructive image charge detection in the endcaps of the Penning trap, have been utilized as it is the case with this experiment. Hence, only the characteristics of the axial motion relevant to this detection technique will be elaborated further. For an overview on different techniques, see [VD95].

Parameter	$^1\text{H}^+$	$^{12}\text{C}^{4+}$	$^3\text{H}^+$	$^3\text{He}^+$
Ring voltage (V)	29.7	88.5	89.000	88.999
Axial frequency ν_z (MHz)	4.0	4.0	4.0	4.0
Axial energy E_z (eV)	$3.4 \cdot 10^{-4}$	$3.4 \cdot 10^{-4}$	$3.4 \cdot 10^{-4}$	$3.4 \cdot 10^{-4}$
Axial quantum number n_z	$2 \cdot 10^4$	$2 \cdot 10^4$	$2 \cdot 10^4$	$2 \cdot 10^4$
Axial amplitude A_z (μm)	10.1	3.0	5.9	5.8
Mod. cyc. freq. ν_+ (MHz)	80.055822	26.617367	26.472458	26.472637
Mod. cyc. energy E_+ (eV)	$6.9 \cdot 10^{-3}$	$2.3 \cdot 10^{-3}$	$2.3 \cdot 10^{-3}$	$2.3 \cdot 10^{-3}$
Mod. cyc. ampl. A_+ (μm)	2.2	1.2	2.3	2.3
Magn. frequency ν_- (kHz)	99.930	300.555	302.200	302.198
Magn. energy E_- (eV)	$-8.6 \cdot 10^{-6}$	$-2.5 \cdot 10^{-5}$	$-2.6 \cdot 10^{-5}$	$-2.6 \cdot 10^{-5}$
Magn. amplitude A_- (μm)	2.2	1.2	2.3	2.3

Table 3.1: Typical motional frequencies and energies in the Penning trap used for this thesis work. The axial frequency is kept at $\nu_z = 4$ MHz, the magnetic field is $B \approx 5.258\text{T}$. The motional amplitudes and energies are for a 4 K environment and fully cooled modes. The effect of compensation electrodes is neglected.

3.3.1 Harmonic oscillator model of the ion

In order to achieve high-precision measurements non-destructive detection methods are favorable. An elegant way to detect the ion is via the image currents induced into the endcaps of the Penning trap. In a simplified model these electrodes can be considered as a parallel plate capacitor with a distance $\tilde{d} = 2z_0$ between the infinitely large plates (see Fig. 3.4).

To detect these image currents a resistor can be attached to the capacitor. This will result in a voltage drop across the resistor $V_R = R \cdot I$, where I is the image current. This corresponds to an electric field between the plates

$$E = \kappa \frac{V_R}{2z_0} \quad , \quad (3.20)$$

where $\kappa = 1$ for the case of a parallel plate capacitor and $\kappa \approx 0.8$ for hyperbolic Penning traps [Gab83]. The power dissipated in the resistor is

$$P = V_R \cdot I = E \cdot q \cdot \dot{z} = F_{\text{diss}} \dot{z} \quad . \quad (3.21)$$

This equation can be solved for \dot{z} yielding

$$\dot{z} = \frac{2z_0}{q\kappa} I \quad . \quad (3.22)$$

The dissipative force F_{diss} is added to the equation of motion (3.10), resulting in

$$m\ddot{z} + m\omega_z^2 z = -E \cdot q = -q\kappa \frac{V_R}{2z_0} \quad . \quad (3.23)$$

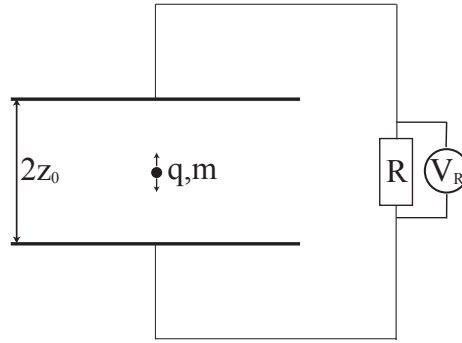


Figure 3.4: Simple model for the detection of ions in a Penning trap. The ion is moving between the plates of a capacitor. The induced current is detected via the voltage drop across a resistor.

Inserting

$$V_R = R \cdot I = R \frac{q\kappa}{2z_0} \dot{z} \quad (3.24)$$

Eq. (3.23) can be identified as the equation of a damped harmonic oscillator

$$m\ddot{z} + m\gamma_z\dot{z} + m\omega_z^2 z = 0 \quad . \quad (3.25)$$

Here, $\gamma_z/2$ is the decay constant of the damped motion. For the single ion between two parallel plates it is

$$\gamma_z = \frac{R}{m} \left(\frac{q\kappa}{2z_0} \right)^2 \quad . \quad (3.26)$$

A damped harmonic oscillation is not yet what is needed in order to continuously detect the image currents induced by the ion, as the signal is decaying away with time. Hence, the addition of an axial driving force

$$F(t) = \frac{\kappa' V_d(t) \cdot q}{2z_0} \quad (3.27)$$

is necessary in order to keep the ion in a steady state. Here κ' is a characteristic constant of the trap, depending on the electrode the drive is applied (if it is applied to the endcap $\kappa' = \kappa$, which will be assumed here for simplicity). The axial equation of motion then becomes

$$m\ddot{z} + m\gamma_z\dot{z} + m\omega_z^2 z = F(t) \quad , \quad (3.28)$$

with well-known text-book solutions [LL76].

However, as already mentioned, the observable in Penning trap mass measurements is not the motional amplitude of the ion but the induced image current I . Inserting Eq. (3.24)



Figure 3.5: The equivalent parallel circuit of a real inductor.

into Eq. (3.28) and utilizing Eq. (3.27) yields

$$m \left(\frac{2z_0}{q\kappa} \right)^2 \frac{dI}{dt} + R \cdot I + m\omega_z^2 \left(\frac{2z_0}{q\kappa} \right)^2 \int dt I = V_{\text{drive}}(t) \quad . \quad (3.29)$$

External tuned circuit and ion tuned circuit

Before deriving the solutions to Eq. (3.29) the simple model of a parallel plate capacitor should be replaced by the realistic case of a Penning trap. First of all, the geometry of the Penning trap with hyperbolic electrodes gives a deviation from $\kappa = 1$ to $\kappa \approx 0.8$.

Even more important is the fact that the trap electrodes have a capacitance to ground C_t . This means that the impedance of the detection circuit is not purely ohmic if only a resistor was added. Instead an inductor L_{ext} is attached to the trap in order to tune out C_t at the resonance frequency

$$\omega_{LC} = \frac{1}{\sqrt{L_{\text{ext}}C_t}} \quad . \quad (3.30)$$

L_{ext} normally is chosen such that $\omega_{LC} \approx \omega_z$. A real inductor also has a series resistance R_s . Assuming that R_s is small compared to the series impedance ωL_{ext}^s the real inductor can be described by an equivalent parallel circuit (see Fig. 3.5) with

$$R_p = R_s \left[1 + \left(\frac{\omega L_{\text{ext}}^s}{R_s} \right)^2 \right] \approx \frac{(\omega L_{\text{ext}}^s)^2}{R_s} = Q_{\text{ext}} \omega L_{\text{ext}}^s \quad (3.31)$$

$$L_{\text{ext}}^p = L_{\text{ext}}^s \left[1 + \left(\frac{R_s}{\omega L_{\text{ext}}^s} \right)^2 \right] \approx L_{\text{ext}}^s \quad . \quad (3.32)$$

Here ω is the resonance frequency of the resulting LRC circuit, that approximately is ω_{LC} for small R_s . Q_{ext} is the quality factor of the tuned circuit that is a measure of its damping.

In addition, the ion can also be modeled as a tuned circuit as has been pointed out by Wineland and Dehmelt [WD75]. This allows to treat the combination of the ion tuned circuit with the external tuned circuit completely in terms of electrical quantities. A representation of this model is given in Fig. 3.6. The differential equation of a driven series tuned circuit is

$$R \cdot I + L \frac{dI}{dt} + \frac{1}{C} \int dt I = V_{\text{drive}}(t) \quad . \quad (3.33)$$

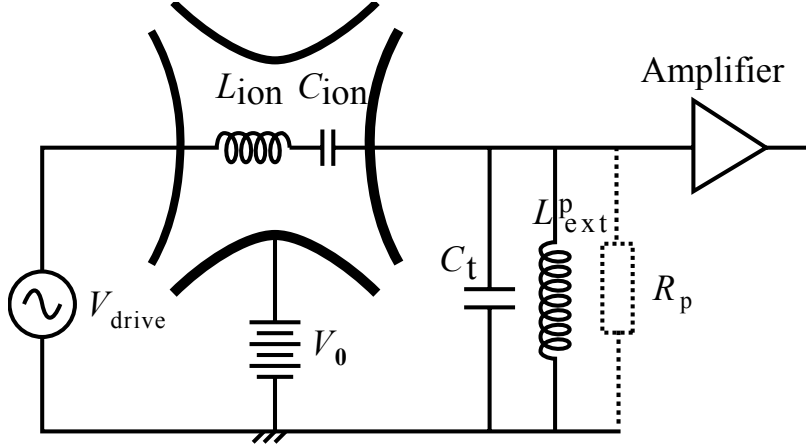


Figure 3.6: The tuned circuit model of the ion and the external tuned circuit.

Comparing this to Eq. (3.29) yields

$$L_{\text{ion}} = m \left(\frac{2z_0}{q\kappa} \right)^2 \quad (3.34)$$

$$C_{\text{ion}} = \frac{1}{\omega_z^2 L_{\text{ion}}} \quad (3.35)$$

3.3.2 Lineshapes in axial ion detection

In order to determine the axial lineshape Eq. (3.29) of the ion driven with $V_{\text{drive}}(t) = |V_d|e^{i\omega_d t}$ the ansatz $I = I(\omega_d)e^{i\omega_d t}$ is taken. Inserting this into Eq. (3.29) and utilizing the definitions of Eq. (3.34) yields

$$I(\omega_d) = \frac{V_d}{(i\omega_d L_{\text{ion}} - i\frac{1}{\omega_d C_{\text{ion}}}) + R_{\parallel}} \quad (3.36)$$

Rewriting this in terms of ω_z and γ_z by using Eq. (3.34) and Eq. (3.42) results in

$$\begin{aligned} I(\omega_d) &= \frac{i\omega_d \gamma_z V_d}{R_{\parallel}(\omega_z^2 - \omega_d^2 + i\omega_d \gamma_z)} \quad (3.37) \\ &= \frac{V_d}{R_{\parallel} \cdot ((\omega_d^2 - \omega_z^2)^2 + \omega_d^2 \gamma_z^2)} \cdot [\omega_d^2 \gamma_z^2 - i\omega_d \gamma_z (\omega_d^2 - \omega_z^2)] \quad . \end{aligned}$$

The experimental observable is the voltage drop $V_R(\omega_d) = R_{\parallel} \cdot I(\omega_d)e^{i\omega_d t}$ across R_{\parallel} . Using the Euler notation this can be written as $V_R(\omega_d) = |V_R(\omega_d)|e^{i\phi(\omega_d)}$ with

$$|V_R(\omega_d)| = \frac{\omega_d \gamma_z V_d}{[(\omega_d^2 - \omega_z^2)^2 + \gamma_z^2 \omega_d^2]^{\frac{1}{2}}} \quad (3.38)$$

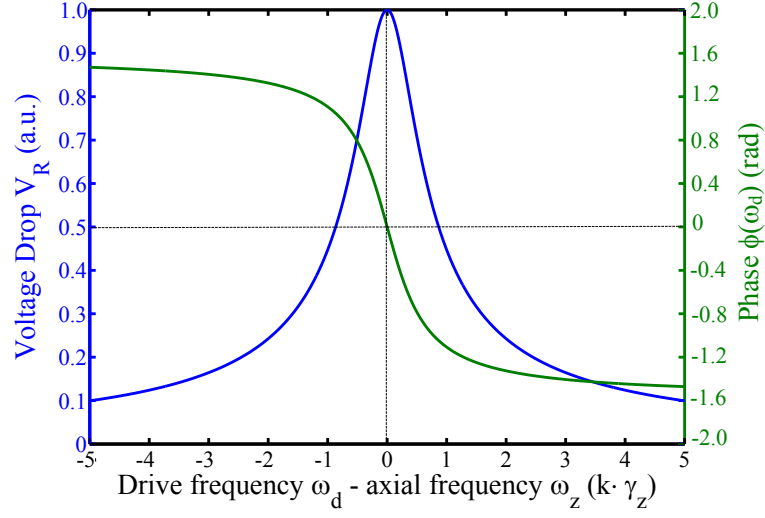


Figure 3.7: The lineshape and the phase of a driven axial ion resonance. The center frequency is given as $\omega_{\text{center}} = \sqrt{\omega_z^2 - \frac{\gamma_z^2}{2}}$ and the full-width at half maximum as $\text{FWHM} = \sqrt{3} \cdot \gamma_z$. The abscissa is scaled in terms of a number k of axial line-widths.

and

$$\phi(\omega_d) = -\tan^{-1} \left(\frac{\omega_d^2 - \omega_z^2}{\omega_d \gamma_z} \right) . \quad (3.39)$$

The shape resulting from Eq. (3.38) is illustrated in Fig. 3.7. The center of the resonance curve is at $\omega_{\text{center}} = \sqrt{\omega_z^2 - \frac{\gamma_z^2}{2}}$. Its full-width at half maximum is given as $\text{FWHM} = \sqrt{3} \gamma_z$. It should also be noted that in principle the noise of the detection system needs to be included into the treatment of the ion tuned circuit given above. However, on resonance the ion tuned circuit shorts out the voltage noise of the parallel resistor R_{\parallel} . In addition the thermal noise is less strong than the coherent drive signal in many cases.

In experimental practice the axial signal is detected by means of a phase-sensitive detection technique. The phase $\phi(\omega_d)$ is determined by mixing the axial signal $V_R(\omega_d)$ with the drive signal shifted by a phase ϕ_{det} . The resulting error signal is

$$V_S(\omega_d) = G_{\text{det}} |V_R(\omega_d)| \cdot \cos[\phi(\omega_d) + \phi_{\text{det}}] . \quad (3.40)$$

Here G_{det} is the overall gain of the detection system. The shape of the error signal $V_S(\omega_d)$ depends on the phase $\phi(\omega_d)$ and the number of ions N as illustrated in Fig. 3.8. For the frequency lock scheme, the dispersion-shaped signal ($\phi_{\text{det}} = 90^\circ$) is utilized. This results in

$$V_S(\omega_d) = G_{\text{det}} \frac{\omega_d(\omega_d^2 - \omega_z^2) \gamma_z V_d}{(\omega_d^2 - \omega_z^2)^2 + \omega_d^2 \gamma_z^2} . \quad (3.41)$$

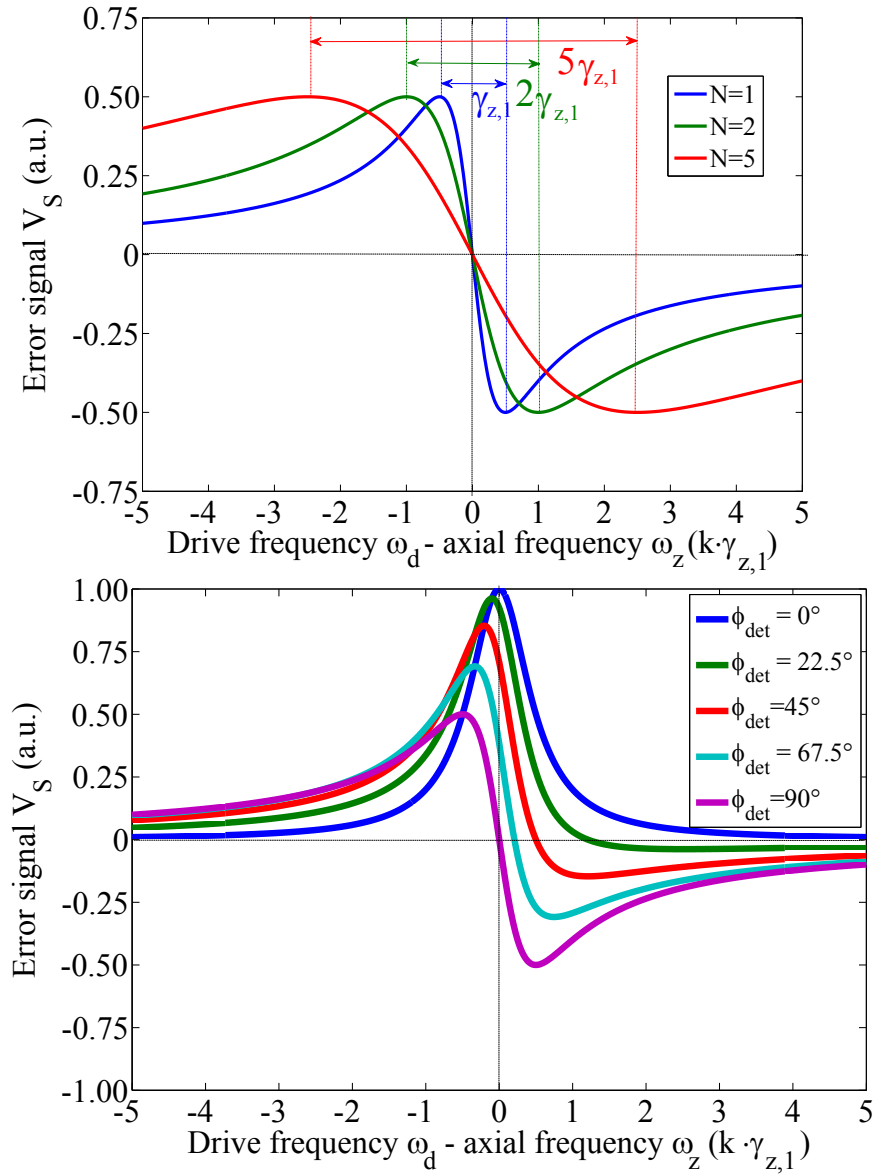


Figure 3.8: In the upper figure a resonance with $\phi_{\text{det}} = 90^\circ$ is shown for different ion numbers N . In the lower figure different phases for the same ion number ($N = 1$) are illustrated. The abscissa is scaled in terms of single-ion axial line-widths, where k is the number of line-widths.

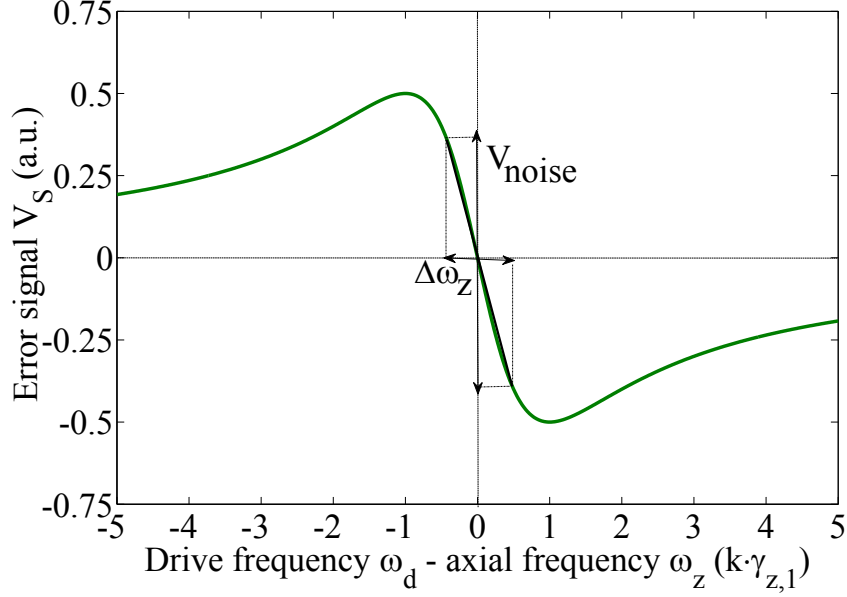


Figure 3.9: The effect of noise on the axial resolution. The noise voltage V_{noise} induces an uncertainty $\Delta\omega_z$ in the determination of the zero-crossing of the error signal.

The width of the signal is γ_z as is illustrated in Fig. 3.8. Utilizing Eq. (3.31) and Eq. (3.34) the line-width can be identified as

$$\gamma_z = \frac{R_p}{L_{\text{ion}}} = \frac{R_p}{m} \left(\frac{q\kappa}{2z_0} \right)^2 = \frac{N \cdot Q_{\text{ext}}}{m_{\text{ion}} \omega_z C_t} \cdot \left(\frac{q_{\text{ion}} \kappa}{2z_0} \right)^2 = N \cdot \gamma_{z,1} \quad . \quad (3.42)$$

Here, q_{ion} is the charge of a single ion and m_{ion} its mass. They are related to the quantities q and m by the number of ions N . $\gamma_{z,1}$ is the line-width of a single ion.

Eq. (3.42) demonstrates two important features of the ion detection technique: First of all, inserting realistic values (see Table 4.2), it shows that the ions have a line-width that is much smaller than the line-width of the external tuned circuit, given as $\gamma_{\text{TC}} = \omega_z / Q_{\text{ext}}$. This again validates the assumption that the ions see the external tuned circuit as a pure resistor. And secondly, it hints to the possibility to determine the ion number in the trap as the line-width of the ions is directly proportional to the number of ions N .

3.3.3 Axial frequency resolution

In particular unfavorable to the axial frequency detection are effects that limit the ability to resolve the exact axial frequency. One such effect comes from the noise of the detection system V_{noise} . Assuming $V_{\text{noise}} = 0$, the axial frequency is determined by finding the zero-crossing of the dispersion-shaped signal (assuming $\phi_{\text{det}} = 90^\circ$). For $V_{\text{noise}} \neq 0$ the axial

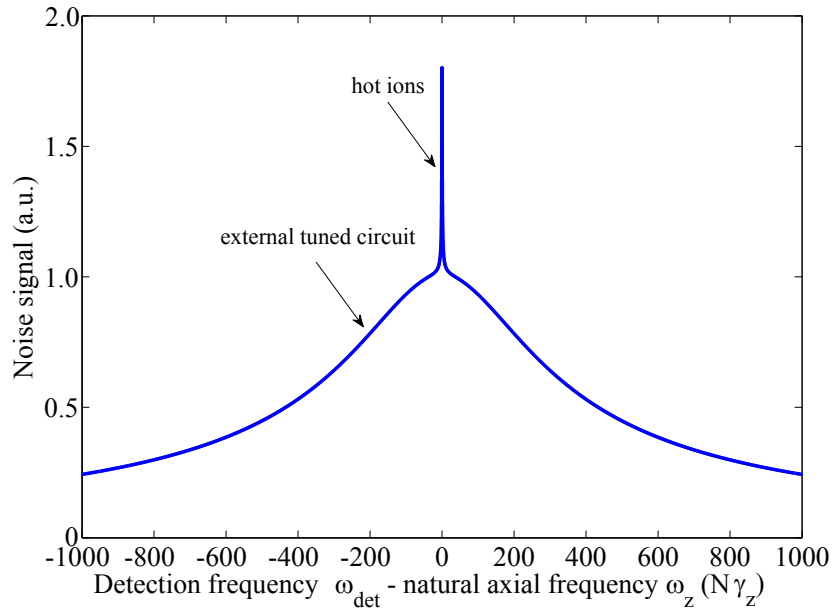


Figure 3.10: Hot ion cloud on top of the external tuned circuit.

resonance is smeared out and the exact zero-crossing cannot be determined unambiguously any longer (see Fig. 3.9). Instead only an interval $\Delta\omega_z$ can be defined by the condition $|V_S| \leq V_{\text{noise}}$. This results in

$$\Delta\omega_z = V_{\text{noise}} \cdot \left(\frac{dV_S(\omega_d)}{d\omega_d} \right)^{-1} \Big|_{V_S=0} . \quad (3.43)$$

Inserting the derivative of Eq. (3.41) yields a broadening of the axial line-width of

$$\Delta\omega_z = \frac{\gamma_z V_{\text{noise}}}{2V_d} . \quad (3.44)$$

3.3.4 Incoherent noise detection

In practice, coherent detection of the ions as described in the previous sections can be sometimes hard or even impossible, when large amounts of contamination ions are present in the trap. So for diagnostic purposes and mass scans, another detection scheme is available. The scheme relies on detecting the noise amplitude of the tuned circuit and changes to it induced by the ions. The effective noise voltage as a function of frequency without the ions is dominated by the external tuned circuit. Assuming white Johnson noise

$$V_{\text{noise}} = \sqrt{4k_B T R_p \nu_b} , \quad (3.45)$$

where ν_b is the detection bandwidth (with $\nu_b \ll \gamma_{LC}$), the noise spectrum shows a similar shape as the ions response (see Fig. 3.7). A main difference is that the line-width γ_{LC} of this parallel tuned circuit is orders of magnitude larger than γ_z . The presence of ions in the trap adds additional signal around the frequency ω_z , depending on the effective axial ion temperature T_{ion} . Starting from Eq. (3.22) and assuming $\frac{1}{2}m\bar{z}^2 = k_B T_{\text{ion}}$ the corresponding effective voltage is

$$V_{\text{ion}}^{\text{eff}} = \sqrt{\frac{k_B T_{\text{ion}} q^2 \kappa^2}{4mz_0^2}} \cdot R_p^2 \quad . \quad (3.46)$$

The hotter the ions are, the more signal is detected in the noise. As soon as the ions come into resonance with the tuned circuit they approach thermal equilibrium and the signal is decaying with a time-constant

$$\tau_z = \frac{2}{\gamma_{z,1}} \quad , \quad (3.47)$$

which resembles the decay time of the undriven solution ($F(t) = 0$ in Eq. (3.28)). Being in thermal equilibrium the ions would even short out the noise voltage at their resonance frequency resulting in a dip in the noise spectrum (see [WD75] for more details). However, this shorting is not complete in practice. Phenomenologically this can be explained by introducing an additional series resistance R_{ion} in the ion tuned circuit, so that the noise is not completely shorted out. As the dip is harder to observe than the peak of hotter ions, which can be explained by the higher signal-to-noise ratio and broadening effects already discussed in section 3.3.3, methods to heat the ions are necessary.

One particularly effective approach is to apply a drive close to $2\omega_z$. This can cause a so-called parametric resonance [LL76]. In order for this drive to be effective, it is necessary that the potential created by it has a quadrupolar component, so that the additional drive force is proportional to the amplitude z of the ion. In this case, the equation of motion (3.28) is modified to

$$\ddot{z} + \gamma_z \dot{z} + \omega_z^2 [1 + A_{\text{par}} \cos[(2\omega_z + \varepsilon)t]]z = 0 \quad , \quad (3.48)$$

where A_{par} is a function of the strength of the parametric drive and ε is a small deviation parameter with $\varepsilon \ll \omega_z$. This kind of differential equation is called a Mathieu equation [Mat68]. It has a solution

$$z(t) = a(t) \cos \left[\left(\omega_z + \frac{\varepsilon}{2} \right) t \right] + b(t) \sin \left[\left(\omega_z + \frac{\varepsilon}{2} \right) t \right] \quad , \quad (3.49)$$

where $a(t)$ and $b(t)$ vary slowly with time. Inserting Eq. (3.49) into Eq. (3.48), it can be shown that a solution to $a(t)$ and $b(t)$ exists that is proportional to e^{st} , where s is a positive real number. This means that the amplitude of the ion motion increases exponentially in time. The condition for this phenomenon to occur is

$$-\sqrt{\frac{A_{\text{par}}^2 \omega_z^2}{4} - \gamma_z^2} < \varepsilon < +\sqrt{\frac{A_{\text{par}}^2 \omega_z^2}{4} - \gamma_z^2} \quad , \quad (3.50)$$

also implying that $|A_{\text{par}}|$ needs to be larger than $\frac{2\gamma_z}{\omega_z}$ in order for parametric resonance to occur. However, an exponentially increasing amplitude is undesirable as the ions would be expelled from the trap quickly, depending on the time-scale given by $1/s$. Fortunately, unavoidable higher order contributions to the trapping potential (see section 3.4) limit the maximum amplitude and allow for parametric detection even of single particles in a Penning trap [TG95].

3.4 Shifts to the axial frequency

The motion described in the sections above was the motion of an ion in an ideal Penning trap, where higher-order effects in the electric and magnetic fields were neglected. Also other effects such as voltage noise, misalignment or special relativity have not been considered in the treatment above. Depending on the specific arrangement of an experiment, also other deviations can arise, e.g. for this experiment a shift in the axial motion due to the modulation of the ring voltage is observed. In the following, the shifts in the axial frequency caused by effects relevant to this experiment will be discussed briefly. A more profound discussions can be found in the review article of Brown and Gabrielse [BG86].

3.4.1 Higher order effects and special relativity

So far, a constant magnetic field $\vec{B} = B\hat{z}$ and a quadrupolar electrostatic potential (see Eq. (3.4)) have been assumed. In reality higher order terms of the magnetic and electrostatic potential have to be considered. Higher order magnetic terms can arise from the geometry of the superconducting coils, compensation coils added to the setup and the distribution of the materials surrounding the ions. Assuming rotational symmetry for all these effects, the deviations from a constant magnetic field can be developed on the z -axis in cylindrical coordinates $r = (\rho, z)$, with $r^2 = \rho^2 + z^2$ into

$$\delta B = \sum_{n=0}^{\infty} B_n \cdot r^n \cdot P_n(\cos \Theta) \quad . \quad (3.51)$$

Here, P_n are Legendre polynomials and Θ is the angle between r and z . B_0 is a constant offset, that causes a different effective B , which is no problem as long as it is constant in time. B_1 is the linear distortion that should be 0 due to mirror symmetry. B_2 is the so called magnetic bottle term. Including the magnetic field in the ρ -direction as well, the B_2 also induces a coupling between the axial and the radial motions.

Higher order effects of the electrostatic fields are caused by the deviation of the electrodes from infinitely large hyperbolic surfaces of revolution, charging of the electrodes or misalignment. Again assuming cylindrical symmetry it can be parametrized as

$$\delta \Phi = \frac{1}{2} V_0 \sum_{n=0}^{\infty} C_n \left(\frac{r}{d} \right)^n P_n(\cos \Theta) \quad . \quad (3.52)$$

Typically, it is assumed that only the even terms of this development are relevant as mirror symmetry of the trap arrangement is expected. The C_0 correction gives a constant offset to the potential that has no influence on the electric field and hence on the motion of the particle. The C_2 correction gives a constant shift of the natural axial frequency. However, this does not cause any problem as long as C_2 stays constant in time. Effectively the C_2 is usually treated as a renormalization of the characteristic trap dimension d to an effective d_{eff} . The octupolar correction C_4 causes a problematic distortion as it introduces non-harmonic behavior and coupling between the eigenmotions in the trap.

A third effect coupling and shifting the frequencies of the eigenmotions is the relativistic mass increase. The higher the energy in one of the modes is, the higher is the relativistic mass and hence the lower the frequency in the other eigenmodes.

A complete discussion of the leading shifts induced by B_2 , C_4 , and relativity is given in the PhD thesis of Farnham [Far95]. Here, only the results for the axial motion that are particularly important for the detection scheme (see section 3.6.2) are given. In the following equation $\alpha = \omega_z/\omega_+$ is a small parameter ($\alpha < 0.15$ for the experiments carried out in this thesis) around which a series expansion was performed. Only the first two non-vanishing terms of each series are given as all higher orders are negligible, even for the highest precision of $\delta m/m = 1 \cdot 10^{-11}$ reached so far in Seattle.

$$\begin{aligned} \frac{\delta \omega_z}{\omega_z} = & \left[\frac{B_2}{m\omega_z^2 B_0} (1 + \alpha^2) - \frac{1}{mc^2} \left(\frac{1}{2} + \frac{1}{4} \alpha^2 \right) - \frac{6C_4}{qV_0} \left(\frac{1}{2} \alpha^2 + \frac{1}{4} \alpha^4 \right) \right] \cdot E_+ \\ & + \left[-\frac{3}{8mc^2} + \frac{3C_4}{2qV_0} \right] \cdot E_z \\ & + \left[-\frac{B_2}{m\omega_z^2 B_0} (1 + \alpha^2) - \frac{1}{mc^2} \left(-\frac{1}{4} \alpha^2 - \frac{1}{8} \alpha^4 \right) + \frac{6C_4}{qV_0} \left(1 + \frac{1}{2} \alpha^2 \right) \right] \cdot E_- \quad (3.53) \end{aligned}$$

Anharmonic axial motion

A major problem limiting high-precision mass measurements is the anharmonicity of the trap. Anharmonicity means that the frequency of an oscillator is not independent of the motion amplitude any longer. The leading anharmonic terms in a Penning trap are the sextupolar correction C_3 (which can often be neglected due to mirror symmetry) and the octupolar correction C_4 . Looking at the dependences on ρ and z from $P_3(\cos \Theta)r^3 = z^3 - \frac{3}{2}z\rho^2$ and $P_4(\cos \Theta)r^4 = z^4 - 3z^2\rho^2 + 3\rho^4/8$ only the z^3 and z^4 -term can contribute to the anharmonicity in the axial motion. The $z^2\rho^2$ term couples axial and radial motion as already shown in Eq. (3.53), and hence results in a constant shift of the axial frequency as long as the radial modes do not change their energies. The ρ^4 and the $z\rho^2$ terms are no direct source of anharmonicity. So, concentrating on the z^3 and z^4 -term the axial equation of motion (see Eq. (3.10)) is modified to

$$\ddot{z} + \gamma_z \dot{z} + \omega_z^2 \left(1 + \frac{3}{2} C_3 \frac{z}{d} + 2C_4 \frac{z^2}{d^2} \right) z = F(t)/m \quad . \quad (3.54)$$

The corrections result in an amplitude-dependent axial frequency of (see [LL76] for the details)

$$\omega_z(A_z) = \omega_z + \frac{A_z^2}{d^2} \left(-\frac{45C_3^2}{48} + \frac{3C_4}{4} \right) \omega_z \quad . \quad (3.55)$$

The amplitude-dependency of ω_z causes the shape of the axial signal to change as a function of amplitude. This is called anharmonic pulling. Qualitatively it can be described in the following way: When sweeping the drive over the axial resonance, the amplitude A_z gets larger. This changes the resonance frequency according to Eq. (3.55). If the axial frequency changes in the same direction as the drive frequency, the ions will stay in resonance with the drive over a larger frequency interval, resulting in a wider resonance. If the drive is swept the other way around, the natural axial frequency and the drive frequency will change in opposite directions, and hence the resonance will be narrower.

Effect of asymmetric potentials

Effects such as patch potentials or asymmetrically biased endcaps induce a potential with asymmetric terms, where C_1 and C_3 are the leading contributors [BG86]. The asymmetric potential V_A has two effects: The first effect is to change the center of the ion motion by

$$\Delta z = -\frac{d^2 \cdot V_A \cdot C_1}{2 \cdot z_0 \cdot V_0} \quad . \quad (3.56)$$

This effect can also be utilized intentionally to move the ion in the trap and map the magnetic field. The second effect is a shift in the axial frequency given as

$$\frac{\Delta \nu_z}{\nu_z} = \frac{3}{4} \left(\frac{d}{z_0} \right)^4 C_1 \cdot C_3 \frac{V_A^2}{V_0^2} \quad . \quad (3.57)$$

Compensated Penning trap

In order to cancel the higher order electrostatic terms and in particular C_4 , the leading electrostatic frequency shift contribution, compensation electrodes (called guards) are added to the basic Penning trap design. This results in an additional potential near the center of the trap

$$\Phi_c = \frac{1}{2} V_c \sum_{k=0}^{\infty} D_k \left(\frac{r}{d} \right)^k P_k(\cos \Theta) \quad . \quad (3.58)$$

Assuming that the guards are constructed and mounted mirror symmetrically, only the even terms should be non-zero; however by applying different voltages to the upper and lower guards it is also possible to influence the odd terms, which can be necessary to compensate for charging of the trap electrodes. D_0 is unobservable for the ions, and hence does not play any role. D_1 shifts the center of the ion motion in the Penning trap. D_2 adds a somewhat unwanted shift to the axial frequency by changing the potential curvature at the center of

the trap. It can be avoided by an appropriate choice of the ratio of ρ_0 to z_0 as has been shown by Gabrielse [Gab83]. D_3 and D_4 are used to cancel out the C_3 and C_4 term, which cause anharmonic shifts (see 3.4.1).

By winding compensation coils around the trap a similar cancellation of the higher order magnetic field terms is possible as well.

3.4.2 Misalignment and trap ellipticity

Other frequency shifts originate from deviations of the trap surfaces from the ideal hyperbolic shape and from misalignment of the electric field with respect to the magnetic field axis. These two effects are summarized in [Gab09b]. The deviation of the trap surfaces is characterized by the harmonic distortion parameter ε that modifies the potential to

$$\Phi(x, y, z) = \frac{V_0}{2d^2} \left(z^2 - \frac{1}{2}(x^2 + y^2) - \frac{\varepsilon}{2}(x^2 - y^2) \right) . \quad (3.59)$$

The misalignment of the magnetic field axis is characterized by the two angles θ and ϕ :

$$\begin{aligned} B_x &= B_0 \sin \theta \cos \phi \\ B_y &= B_0 \sin \theta \sin \phi \\ B_z &= B_0 \cos \theta \quad . \end{aligned} \quad (3.60)$$

The two effects result in a modification of the equations of motion and hence the eigenfrequencies. They become $\bar{\omega}_+(\theta, \phi, \varepsilon)$, $\bar{\omega}_-(\theta, \phi, \varepsilon)$ and $\bar{\omega}_z(\theta, \phi, \varepsilon)$. However, to first order this effect is not relevant as will be discussed in section 3.6. One possibility to measure and optimize the misalignment angle θ is by maximizing the axial frequency $\bar{\omega}_z$ for a given voltage as

$$\bar{\omega}_z^2 \approx \omega_z^2 \left[1 - \frac{3}{2} \theta^2 \right] . \quad (3.61)$$

A second possibility is to measure the three eigenfrequencies and utilize the relation

$$\bar{\omega}_- = \frac{\bar{\omega}_z^2}{2\bar{\omega}_+} \cdot \left[1 + \frac{9}{4} \theta^2 - \frac{1}{2} \varepsilon^2 \right] . \quad (3.62)$$

3.4.3 Miscellaneous frequency shifts

A number of other frequency shifts have been observed in Penning trap mass spectrometry. They are summarized here shortly: The image charge shift is caused by the image charges induced in the endcaps that modify the effective potential. The resulting shifts are given by

[Por01]:

$$\begin{aligned}\omega_z^2 &= \omega_{z0}^2 - \Delta_z \\ \omega_+ &= \omega_{+0} - \frac{\Delta\rho}{\omega_+} \\ \omega_- &= \omega_{-0} + \frac{\Delta\rho}{\omega_+} .\end{aligned}$$

Here $\Delta_z = \frac{qE_z^{\text{im}}}{md}$ and $\Delta\rho = \frac{qE_\rho^{\text{im}}}{md}$ with $E^{\text{im}} \propto \frac{q}{d^2}$ being the electric field of the image charges.

Another shift of the axial frequency is induced by the modulation, which is part of the detection system as will be discussed in section 4.2. A sideband of the ion motion is created by applying a signal $V_{\text{mod}}(t) = \chi V_0 \cos \omega_{\text{mod}} t$ to the ring. Assuming ω_{mod} to be fast compared to the time-scales of the axial frequency measurement its effect on the potential can be time-averaged, resulting in a shift of the axial frequency of [BG86]

$$\Delta\omega_z = -\omega_z \frac{\chi^2}{16} . \quad (3.63)$$

The modulation also shifts the other eigenmotions. However, these shifts are suppressed by another factor of $(\omega_z/\omega_c)^3$.

A number of other shifts cannot be quantified so nicely. In particular, the effects of contamination ions and ion clouds are apparent in experimental data, while a theoretical treatment is complicated [WD75] and still not fully existing. However, in the case of a single ion in a clean trap, such as one has to achieve for high-precision measurements, both these effects do not play a role.

3.5 Cooling mechanisms

In order to perform high-precision measurements in a Penning trap it is extremely important to have good control over the motions of the ions and in particular to reduce their motional amplitudes A_z , A_+ and A_- . As the center part of the Penning trap just around the potential minimum will be the most harmonic region, deviations as discussed in section 3.4 will be smaller for a well cooled ion than for a hot ion with a larger orbit. For the axial motion, damping of A_z is achieved via the attached tuned circuit as already discussed in section 3.3. So the energy in this mode, E_z , will basically be $k_B T_{\text{TC}}$. For the radial motions, such a coupling to an external tuned circuit does not exist in this experiment, so decreasing their amplitude needs other mechanisms. Natural energy loss mechanisms such as radiative energy loss or collisions with the rest gas do not play a role in the cryogenic environment and for ions as utilized in this thesis. Hence, artificial coupling to the axial motion via sideband excitations of the ions is utilized. A broader overview on different cooling mechanisms in Penning traps can be found elsewhere [Bla06]. For the following discussion it is also useful, albeit not necessary, to switch to a quantum-mechanical picture

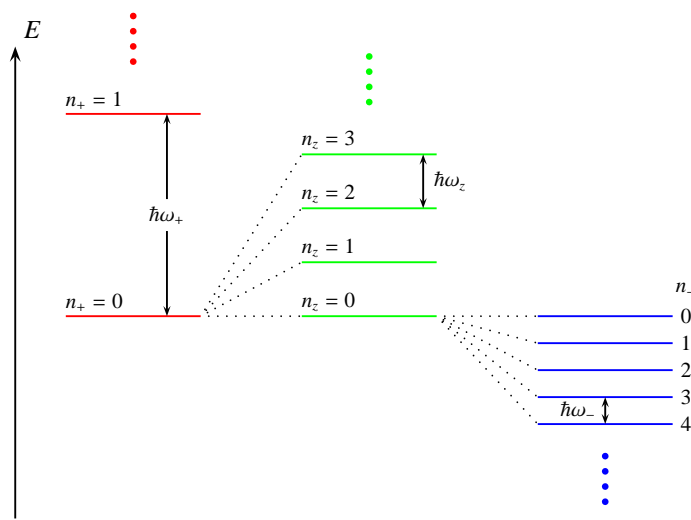


Figure 3.11: Energy level diagram of an ion in a Penning trap. The three eigenmotions of the ion are treated as three harmonic oscillators. Courtesy of Jochen Ketter.

of the ion motion. The quantum-mechanical level diagram, where the three eigenmotions of the ion are treated as three harmonic oscillators, is illustrated in Fig. 3.11.

3.5.1 Magnetron cooling

As already discussed in section 3.2 the magnetron mode is in principle unstable. So in contrast to the axial and the cyclotron mode reducing A_- is accomplished by adding energy to the mode. In this sense the term magnetron cooling is somewhat inappropriate. However, it is the standard term used in literature. Even though the cooling process could be described completely classically as $(n_z, n_-) \gg 1$, it is more convenient and intuitive to explain it in terms of quantum mechanical level diagrams introduced in Fig. 3.11. The total magnetron energy is given as

$$E_- = -\hbar\omega_-(n_- + \frac{1}{2}) \quad \text{with } n_- = 0, 1, 2, \dots \quad , \quad (3.64)$$

while the axial energy is given as

$$E_z = +\hbar\omega_z(n_z + \frac{1}{2}) \quad \text{with } n_z = 0, 1, 2, \dots \quad . \quad (3.65)$$

The cooling is achieved by shining a rf-signal at frequency $\omega_z + \omega_-$ into the trap. This signal has to have a quadrupolar potential component ρz in order to couple the axial with the radial motion. For any level (n_z, n_-) the drive can trigger two transitions: A transition from $(n_z, n_-) \rightarrow (n_z + 1, n_- - 1)$ or a transition from $(n_z, n_-) \rightarrow (n_z - 1, n_- + 1)$. In terms of ladder operators the two processes are explained as $a_z^\dagger a_-$ with a rate proportional to

$(n_z + 1)n_-$ and $a_z a_-^\dagger$ with a rate proportional to $n_z(n_- + 1)$. An equilibrium is reached, when the two rates are equal, which is the case for $n_z = n_-$. Under this condition the magnetron energy becomes

$$E_- = -\frac{\omega_-}{\omega_z} E_z \quad . \quad (3.66)$$

The axial mode is in thermal equilibrium with the tuned circuit. Therefore, it has an energy of $E_z = k_B T_{TC}$, where T_{TC} typically should be close to the temperature of the surrounding environment (in this experiment 4 K), even though feedback in the detection system might significantly alter this temperature [GDG10].

3.5.2 Modified cyclotron cooling

For damping the modified cyclotron motion, the same approach as for the magnetron motion is taken. An rf-signal at a frequency of $\omega_z - \omega_+$ is shone into the trap. For historic reasons this cooling drive is called cyclotron coupling in the context of this experiment. The difference in sign compared to the magnetron case is due to the positive energy of the modified cyclotron motion. The modified cyclotron energy is given as

$$E_+ = \hbar \omega_+ \left(n_+ + \frac{1}{2} \right) \quad \text{with} \quad n_+ = 0, 1, 2, \dots \quad . \quad (3.67)$$

The same considerations as in the magnetron case yield an equilibrium modified cyclotron energy of

$$E_+ = \frac{\omega_+}{\omega_z} E_z \quad . \quad (3.68)$$

3.6 Mass measurements and radial detection

So far, it was shown that three-dimensional confinement of an ion is possible in a Penning trap and how its axial frequency can be detected. The next step is to derive intrinsic properties of the ion. One of the quantities accessible by ion storage in Penning traps is the mass of the ion. As already discussed earlier (see section 3.2) the eigenfrequencies depend on the mass of the ion. In principle the mass could be derived directly from the axial frequency (see Eq. (3.11)). The problem here is the stability of V_0 , which would limit the achievable mass resolution. Another approach would be to use the relation

$$\omega_+ + \omega_- = \omega_c \quad . \quad (3.69)$$

Indeed, this is a standard approach in many experiments that utilize the TOF-ICR technique and is exactly true in the ideal Penning trap. However, Penning trap imperfections, in particular the misalignment of the trap and the ellipticity of the traps finally limit the accuracy of this method (see [Gab09a] for a profound discussion).

3.6.1 The invariance theorem

In order to make full use of the precision and accuracy Penning trap mass spectrometry has to offer, all three eigenfrequencies have to be measured. Then the true cyclotron frequency is derived from their quadratic sum (being called the invariance theorem)

$$\omega_c^2 = \bar{\omega}_+(\theta, \phi, \varepsilon)^2 + \bar{\omega}_-(\theta, \phi, \varepsilon)^2 + \bar{\omega}_z(\theta, \phi, \varepsilon)^2 = \left(\frac{qB}{m}\right)^2 . \quad (3.70)$$

For the perfect trap, where $\theta = \phi = \varepsilon = 0$, this relation is trivial. However, it is also valid, when θ , ϕ and ε are not zero [BG82]. Other shifts as discussed in section 3.4 are not covered by this theorem and have to be investigated separately.

Differentiating Eq. (3.70) also reveals the advantage of the invariance theorem over utilizing ω_z for mass measurements: Not all eigenfrequencies have to be measured to the same precision, the relative uncertainties in ω_z and ω_- are suppressed by the square of their ratio with ω_c :

$$\frac{\Delta\omega_c}{\omega_c} = \left(\frac{\omega_+}{\omega_c}\right)^2 \frac{\Delta\omega_+}{\omega_+} + \left(\frac{\omega_-}{\omega_c}\right)^2 \frac{\Delta\omega_-}{\omega_-} + \left(\frac{\omega_z}{\omega_c}\right)^2 \frac{\Delta\omega_z}{\omega_z} . \quad (3.71)$$

For the frequencies utilized in this thesis work, this means that the relative contribution of the axial frequency is suppressed by at least a factor of 50, while the relative contribution of the magnetron frequency is suppressed by at least a factor of 10^4 .

Knowing ω_c , it is still necessary to determine the magnetic field B to relate the measured frequency to the mass of the ion. As there is no method with comparable precision, this has to be done via an ion in the Penning trap as well. So not only one cyclotron frequency, but the ratio of two cyclotron frequencies is taken (as has already been discussed briefly in section 2.2.4):

$$\frac{m_2}{m_1} = \frac{q_2 B_0}{\omega_{c2}} \cdot \frac{\omega_{c1}}{q_1 B_0} = \frac{q_2}{q_1} \cdot \frac{\omega_{c1}}{\omega_{c2}} . \quad (3.72)$$

The magnetic field B_0 cancels, and due to the quantization of charge, $\frac{q_2}{q_1}$ is a trivial expression. When the time between the two cyclotron frequency measurements is reasonably small and the experimental conditions are identical, a lot of the shifts and drifts in ω_{c1} and ω_{c2} are identical and cancel out to first order.

For absolute mass measurements the natural reference ion is ^{12}C as its mass defines the atomic mass unit u . However, also other reference ions are suitable if their mass is known to higher precision than for the ion-of-interest. For relative measurements, the two ions of interest are normally taken as reference to each other as it was already discussed for the Q -value measurements in section 2.2.4.

3.6.2 Triggered sweep radial detection technique

So far, only the axial detection technique has been discussed. From Eq. (3.70) it is clear that the other eigenmotions also have to be measured. This is done by means of an indirect

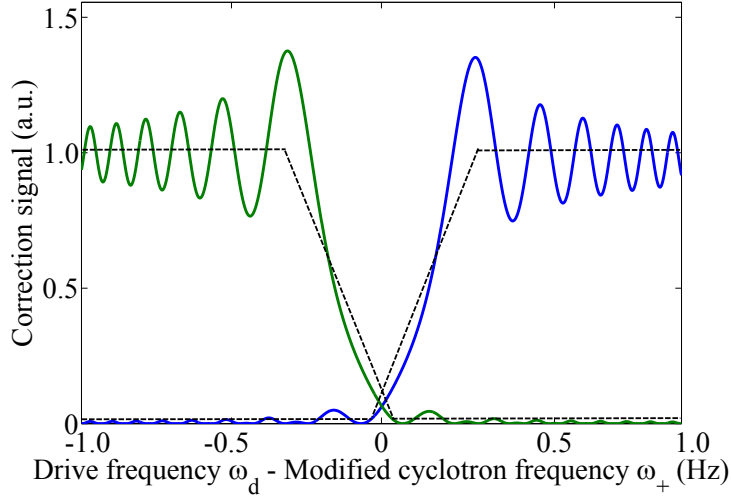


Figure 3.12: Simulation of modified cyclotron resonances with the triggered detection technique. The blue curve is an up-sweep in frequency, the green curve a down-sweep. The dashed black lines are the typical stepfunctions that are fitted to the data in the experiment. The crossing of the up- and the down-sweep occurs at the natural modified cyclotron frequency.

detection method based on the shifts in the axial motion that have already been discussed in section 3.4.1. From Eq. (3.71) it is also clear that the detection of the modified cyclotron motion necessitates the highest precision. The first order frequency shift to the axial motion induced by changes in the cyclotron excitation is given as

$$\frac{\delta \omega_z}{\omega_z} = \left[\frac{B_2}{B_0 m \omega_z^2} - \frac{1}{2mc^2} - \frac{3C_4}{qV_0} \left(\frac{\omega_z}{\omega_+} \right)^2 \right] E_+ \quad . \quad (3.73)$$

In order to use this shift for a determination of the modified cyclotron frequency it is important to keep the axial frequency stable enough to resolve the shifts. A convenient way to achieve this is by making use of the dispersion-shaped driven axial signal (see Fig. (3.8)). Setting the detection phase $\phi_{\text{det}} = 90^\circ$ the signal has two favorable properties: First, the zero-crossing is exactly at the natural axial frequency ω_z and second, only around the zero-crossing the slope of the signal is negative. These two properties allow to lock the axial signal by generating a correction signal ΔV (see section 4.2.4) for the ring voltage, so that

$$V_{\text{ring}} = V_0 + \Delta V \quad . \quad (3.74)$$

The modified cyclotron frequency is then detected by sweeping a rf-drive $\omega_d(t) = \omega_s + \alpha \cdot t$, applied to the trap electrodes, over the cyclotron resonance. Here, $\alpha = d\omega_d/dt$ is the sweep rate and ω_s is the start frequency of the sweep. A theoretical line-shape of this signal can

be obtained [VL04] from solving the equation of motion of the driven modified cyclotron harmonic oscillator for the modified cyclotron radius. The result is

$$r_+(t) = r_+(0) + \frac{q\tilde{E}_{\text{drive}}}{2\omega_+m} \left[\int_0^t \cos\left(\alpha\left(t' + \frac{\omega_s - \omega_+}{2\alpha}\right)^2\right) dt' + \int_0^t \sin\left(\alpha\left(t' + \frac{\omega_s - \omega_+}{2\alpha}\right)^2\right) dt' \right], \quad (3.75)$$

where \tilde{E}_{drive} is the electric field strength of the drive. Inserting the modified cyclotron energy $E_+ = \frac{1}{2}m\omega_+^2 r(t)^2$ into Eq. (3.73) the line-shape of the triggered detection technique is obtained. Fig. 3.12 shows the line-shape for both an up- and downswEEP of the drive frequency. The shape of the signal is explained by beating of the natural modified cyclotron frequency with the drive that is swept. The larger amplitude after passing the resonance reflects the energy absorbed from the drive. The crossing of up- and downswEEP occurs just at the modified cyclotron frequency. Therefore, in practice, it is simpler and more robust to fit a step-like function to the cyclotron resonance and determine the modified cyclotron frequency by bracketing the resonance from both sides. A more detailed discussion also including distortions of the modified cyclotron line-shape was given by Van Liew [VL04]. However, these distortions influence the determination of the modified cyclotron frequency on a level below 1 part in 10^{11} . Shifts of the modified cyclotron frequency, similar to Eq. (3.53) are discussed by Farnham [Far95].

4 Experimental setup

The experimental setup described here is a merger of two experiments that have already been described in earlier theses of the University of Washington [Far95, VL04, Pin07]. The first experiment is the University of Washington-Penning Trap Mass Spectrometer (UW-PTMS). Since the 1980s it has performed several of the most precise mass measurements [VDS81, VDFS93, VDZVL⁺04, VDPVLZ06]. Many important techniques in Penning trap physics, such as resistive cooling, anharmonic detection or the compensation via guard electrodes have been developed and refined in the Seattle group. However, with the existing setup only a limited number of stable isotopes had been accessible by in-trap production and been measured to the precision limit of the spectrometer of about 1 part in 10^{11} . Therefore, an enhanced version of the UW-PTMS was planned. This second experiment is particularly dedicated to the $^3\text{H}/^3\text{He}$ mass-ratio measurement. Main differences to the original UW-PTMS are the external creation of ions, which allows a much wider range of masses to be measured, and the utilization of a double Penning trap system, which allows for a faster measurement procedure. In Seattle, the mechanical construction as well as the detection electronics for this setup were completed. However, only very little tests could be performed on its ion trapping capabilities. Both experiments were shipped to the Max-Planck-Institut für Kernphysik in the course of the year 2008. Here, the two experiments were merged by adding the most useful parts, such as the magnet or the environment stabilization system, of the original experiment to the upgraded version. While minor modifications or additions to the Seattle components have been carried out or will be carried out in the future, the majority of parts remained unchanged. The focus of this thesis was put on demonstrating the capability of the partly untested components to perform work with single ions. In the following, a basic description of all parts relevant for the $^3\text{H}/^3\text{He}$ mass ratio measurement and the commissioning experiments within this thesis will be given. In particular changes to the already existing spectrometers will be discussed. Most notably the computer-control system of the experiment has undergone major modifications towards the automation of the measurement procedure.

4.1 Experimental hardware

In this section the main mechanical components of the setup will be described. An overview is given in Fig. 4.1. Ions can be created either by in-trap creation with a field emission point, which was the case for the $^{12}\text{C}^{4+}$ -studies of this thesis. Or they can be created in the external Penning ion source, which will be the case for future $^3\text{H}/^3\text{He}$ -measurements. The trap assembly is housed in a vacuum envelope situated in the magnetic center of a superconducting magnet with a maximum field strength of 5.9 T. The traps share the 4-K

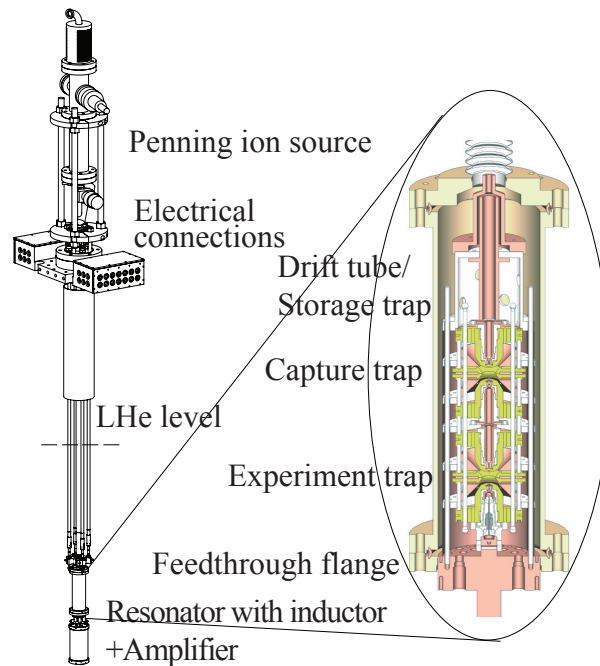


Figure 4.1: Overview on the apparatus and the traps. For more details see text.

liquid helium reservoir with the magnet. The trap tower consists of three traps, two hyperbolic Penning traps and a cylindrical tube trap. Ions from the Penning ion source will be slowed down or even trapped in the tube trap. Only small amounts of ions (1-10 ions) will then be transferred to the capture trap, where single ions will be prepared. For a precision measurement, the ions will be transferred to the experiment trap, where the magnetic field homogeneity is the highest (specified to about $2 \cdot 10^{-8} / \text{cm}^3$). The final measurement cycle [Höc10] foresees the storage of a single ^3H and a single ^3He ion that are continuously swapped between the two traps in order to keep the time between the measurements as short as possible. This would allow to shorten the time scale between measurements of different species from several hours or even days to several minutes, hence resulting in a minimized dependence on long-term drift effects in the magnetic or electrostatic field. Part of the detection electronics also sits inside the 4-K environment of the magnet bore, in particular the external tuned circuit, formed by an inductor, and the amplifier.

4.1.1 Double trap assembly

The heart of the experiment is the trap assembly (see Fig. 4.2). The two hyperbolic traps are almost identical with characteristic dimensions of $\rho_0 = 2.77(1)$ mm and $z_0 = 2.29(1)$ mm at room temperature. Small differences exist though in the size of the holes in the endcaps and skimmers due to the demands of the ion transfer process (see [Höc10] for more details).

The capture trap (C) is dedicated to ion storage and preparation as it is situated out of

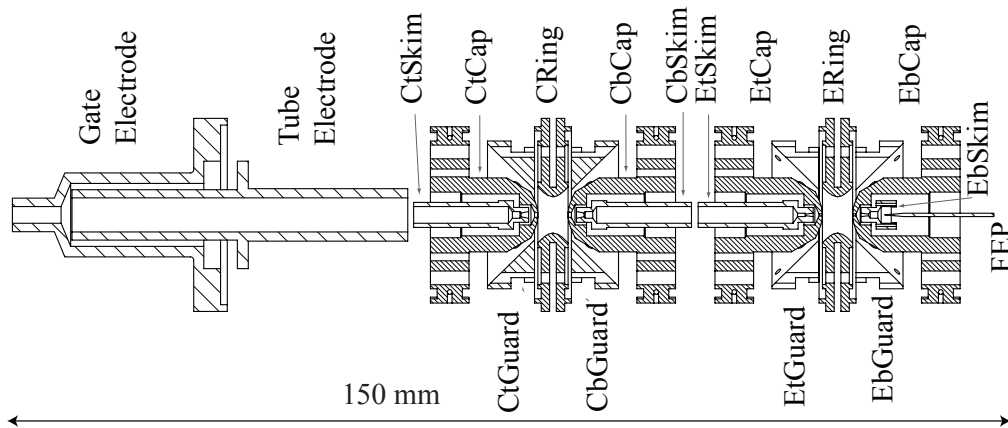


Figure 4.2: Sectional drawing of the trap tower. The naming of the electrodes mainly follows the convention of the thesis of Pinegar [Pin07], where the lower hyperbolic trap is called experiment trap and hence all of its electrodes are named with E, the upper hyperbolic trap is called capture trap and hence its electrodes are named with C. The letters t and b stand for top and bottom.

the most homogeneous region of the magnetic field. For precision measurements, it is intended to transfer a single ion from the capture trap to the experiment trap (E) and perform the high-precision measurements in this trap. In the ideal case, a single ion of another species can be prepared in the capture trap. A full measurement cycle then would consist of a cyclotron frequency measurement for one ion in the experiment trap, switching with another ion, and a cyclotron measurement for the other ion. Simulations and calculations (see [Pin07, Hoc10]) suggest that this trap-to-trap transfer process should be challenging but possible. The major complication is the size of the hole in EtSkim of only $250\ \mu\text{m}$. With proper cooling of the ions and good alignment of the traps the radial displacement of the ions should be on the order of $10\ \mu\text{m}$.

The upper cylindrical trap consists of the gate electrode, the tube electrode and the skimmer CtSkim. It is far from being a perfect cylindrical trap and so its storage capabilities have yet to be proven [Tre11]. Two different modes of operation are intended: The first mode will be as a trap for a large cloud of ions produced by the external Penning ion source. In the second mode, it will be used as a pulsed drift tube to slow down the ions before catching them with the capture trap.

All trap electrodes are fabricated from phosphor bronze, which is an alloy mainly consisting of copper with some admixture of tin and small amounts of phosphorus. All electrodes, except for the skimmers, which have too small holes (as small as $250\ \mu\text{m}$), have been gold-plated in order to avoid patch potentials on the surfaces. Insulators between the different electrodes are made from MACOR. The whole assembly is held together by titanium rods and springs.

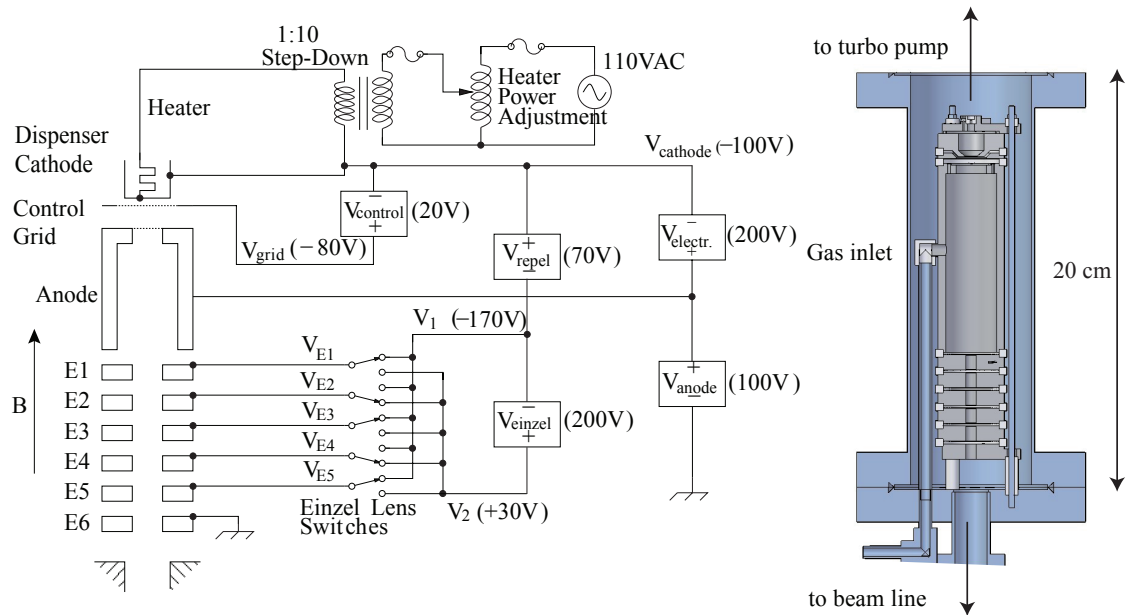


Figure 4.3: Schematics and model of the external ion source.

Electrostatics of the trap

As already discussed in section 3.4.1 the guard electrodes are introduced into the trap design in order to allow for cancellation of unwanted higher order distortions in the electric field. However, this capability in principle comes at the price of also influencing the quadrupolar field by changing the C_2 of the trap. The change in C_2 (being called D_2) is a function of ρ_0/z_0 . At a ratio of about 1.16, C_2 actually is zero. The traps utilized in the experiment are built with a ratio of 1.21, so that a small D_2 -term still remains. Experimentally, the detected D_2 varies quite a lot (between about $-3 \cdot 10^{-2}$ and about $-1 \cdot 10^{-4}$) as a function of the conditions in the trap (see section 6.3). Based on relaxation calculations on a similar Seattle trap [Gab83], it is also possible to estimate D_2 and D_4 . The result is $D_2 \approx -10^{-3}$ and $D_4 \approx -9 \cdot 10^{-3}$. Electrostatic simulations on this issue utilizing the program TOSCA are planned [Sch11].

4.1.2 Ion creation

Ions can be created by different methods in this setup. They all have in common that neutral atoms or molecules are ionized by collisions with electrons. The cross sections for this process are very similar for different ionized species. They start at the ionization energy $E_{\text{ionization}}$ and have a maximum at energies around (3-4) $E_{\text{ionization}}$ [Wol95].

External ion source and gas handling system

The external ion source is intended to provide ions created from gaseous samples. In particular the ions of interest here are ^3H and ^3He . The advantage of an external ion source over the previously used internal ion sources [VDFS93] lies in the much lower contamination of the trap surfaces with ^3H . This turned out to be a major limitation due to self-loading of the traps from electrons, that were emitted in the ^3H beta-decay [VDPVLZ06]. Also, a wider variety of other ions can be loaded without breaking the vacuum of the traps. In addition no disturbance due to heating of internal sources is induced in the cryogenic region.

The ion source chosen for this experiment is a Penning ion source (see Fig. 4.3). In this configuration, an electron-gun is combined with a magnetic field in order to confine the electrons in the radial direction. As the ion source anyway sits in the fringe field (about 3 mT) of the superconducting magnet this kind of ion source was a natural choice. An additional solenoid, creating a field of about 20 mT, is wound around the ion source chamber both for testing purposes and additional optimization of the ion current. A detailed treatment of the ion source characteristics can be found in [Pin03, Pin07].

The electrons are produced in a commercial dispenser cathode manufactured by the company Heat Wave Labs. Electrons are emitted from a tungsten matrix that contains a mixture of barium calcium aluminate. This lowers the work function and allows for emission at temperatures as low as 1250 K, compared to 2600 K for pure tungsten.

The cathode can emit currents of up to 10 mA. However, one major drawback is the strong dependence of the emission on the vacuum pressure in the ion source region, that should not exceed 10^{-7} mbar. The cathode is biased to a potential V_{cathode} of typically -100 V. In front of the cathode a grid is placed that is slightly biased to V_{grid} with respect to the potential of the cathode. It allows to control the electron current. The anode is set at a potential $V_{\text{electr.}}$ about 200 V above the cathode potential. This means that the electrons from the cathode have a typical energy of 200 eV at their collision site with the gaseous sample. The gas is inserted via a hole on the side of the anode. The ions are then accelerated towards an Einzel lens stack that allows focussing of the beam. For typical voltage settings their energy is known to be between 80-90 eV. It should be noted that the purity of the gas inserted into the ion source is important for several reasons. First of all, no mass selective elements filter the beam from contaminant ions before the actual trap tower. There is some suppression of heavier masses due to the increase in cyclotron orbits, though. The addition of other mass-selective elements, such as Wien filters, as has been demonstrated in other setups [HZH⁺95], was not considered necessary [VL04].

A second point that requires clean gas samples is the strong degradation of the dispenser cathode by water vapor. Therefore, the ^3H and ^3He gas was filled into cylinders that were heated to 400 °C before. These cylinders are attached to a gas handling system, that is illustrated in Fig. 4.4. The amount of ^3H or ^3He that is released into the ion source can be controlled by a needle valve in combination with a pressure gauge. By knowing the volume V and the pressure p between the needle valve and the inlet valve the number of

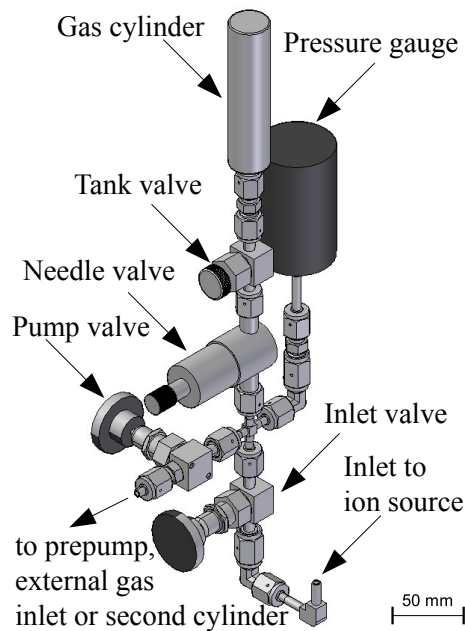


Figure 4.4: Drawing of the gas handling system. Courtesy of Marius Tremer.

gas molecules N can be estimated from the ideal gas law as

$$N = \frac{pV}{k_B T} \quad . \quad (4.1)$$

The volume between the needle valve and the inlet valve is about 25 cm^3 . In order to keep this volume clean, it needs to be pumped for some time prior to the inlet of ^3H and ^3He . In principle, this can be done via the vacuum system of the ion source. However, in practice it turned out that the rest gas that accumulated in the main volume due to outgassing and leaks poisoned the cathode for several hours. Therefore, in addition to the original Seattle design, a possibility to separately pump this volume was installed. Also, for test purposes the possibility to let other gases into the ion source was implemented and utilized.

Field emission point

The standard way of loading the Penning traps in all previous experiments at the University of Washington was the electron impact ionization via an electron beam created in a field emission point (FEP). Also, for almost all ion-related studies of this thesis work, this loading method has been utilized. The field emission point is a very fine tungsten wire that was sharpened in an electro-etching process. The FEP is situated underneath the bottom endcap of the experiment Penning trap (see Fig. 4.5). In order to start electron emission a potential difference between the FEP and the nearby skimmer of 300 V or more is applied, which results in a field emitted electron current of some nA. The electrons then collide

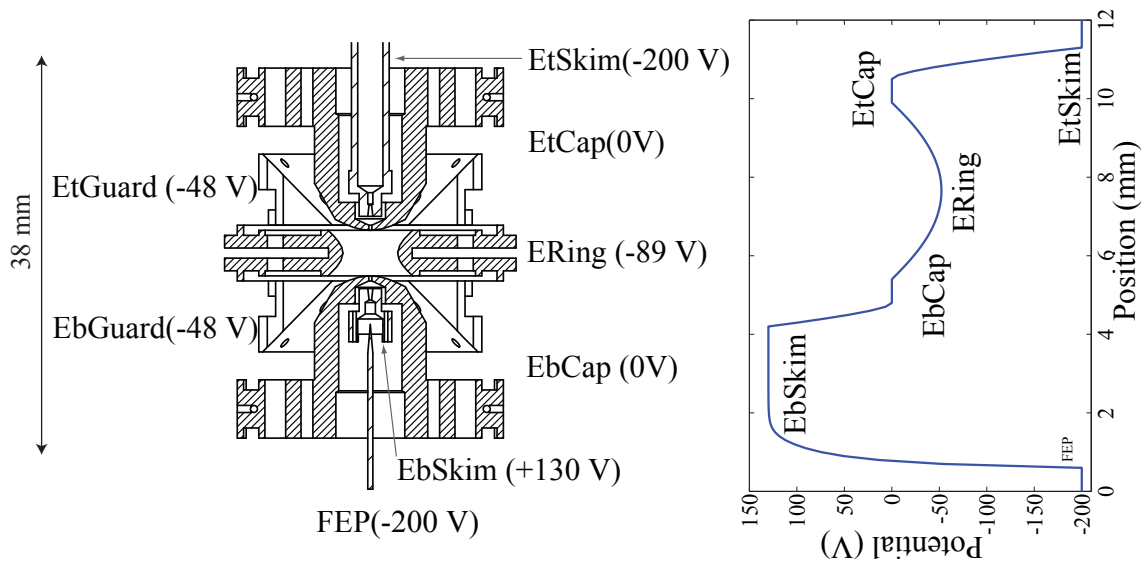


Figure 4.5: Left: Schematics of the experiment trap and settings of the electrodes during the loading procedure. The abbreviations are explained in section 4.1.1. Right: Resulting potential as derived from a SIMION simulation. The abscissa is not on the same scale as the drawing to the left.

with the ions of interest somewhere in the trap volume. In order to have a more effective use of the electrons, the same voltage as on the FEP is applied to the skimmer of the other endcap, which will let the electrons pass multiple times through the trap, before they hit one of the endcaps or skimmers. The ions of interest in our setup can either be sputtered off the surfaces of the trap electrodes or are part of the rest gas. In earlier setups additional atom sources were included [VDFS93]. As the external ion source now serves this purpose, this is not the case any longer. Therefore, only some light ions, such as H, C, N, O, F (see section 6.2.2) can be produced. However, the FEP is able to run with up to 500 V (limited by its power supply), which allows to create high charge states for the light ions. It should be emphasized that the field emission point cannot be utilized for the final ${}^3\text{H}/{}^3\text{He}$ measurements as previous attempts of in-trap-creation of ${}^3\text{H}$ with the FEP suffered from contamination of the trap surfaces by the ${}^3\text{H}$ and subsequent β -emission into the trap.

4.1.3 Magnet systems

From Eq. (3.70) and Eq. (3.71) it is clear that strong magnetic fields are desirable in order to achieve high cyclotron frequencies. This improves the overall mass resolution as the influence of the typically less stable voltage sources is decreased. For fields above about 1 T this results in the need for using superconducting magnets.

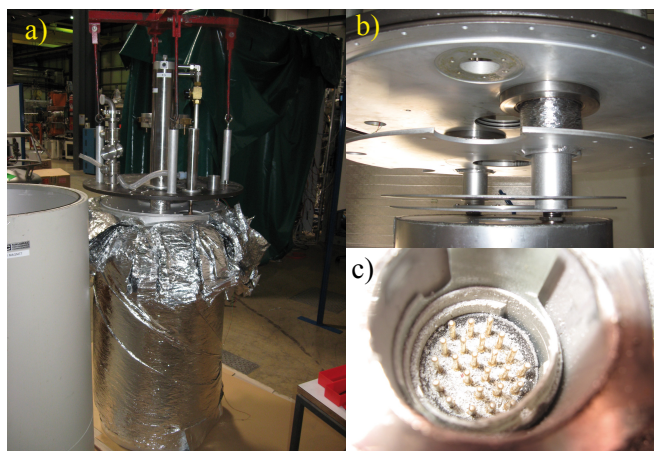


Figure 4.6: a) The 1991 magnet without the housing. Superisolating foil is wrapped around an aluminum shield, which houses the 77-K and 4-K shield. b) Detailed look at the connections and shieldings of the liquid helium reservoir. c) The 24 pin connector to the coils.

Quantity	specified value	measured value
Magnetic field	5.9 T	5.258 T
Field drift	$10^{-9}/\text{h}$	$< 10^{-10}/\text{h}$
Field homogeneity	$2 \cdot 10^{-8}/\text{cm}^3$	$1 \cdot 10^{-5}/\text{cm}^3$
Liquid helium use	$< 1.2 \ell/\text{d}$	$1.4 \ell/\text{d}$

Table 4.1: Specifications of the 1995 magnet.

The 1995 NCC magnet

The magnet system utilized in this experiment has been in use at the University of Washington already since 1995 [VDFZS99]. It was manufactured by Nalorac Cryogenics Corporation (NCC). Its specifications as given by the company or measured in Heidelberg are given in Tab. 4.1. In addition, another magnet system from the same company, utilized for the tests of the new spectrometer, but with lower specifications, was transported to MPIK. Unfortunately, this system broke during the transport and is not available any longer for test purposes. However, the disassembly of this system gave some interesting insights in the construction of the magnet system (see Fig. 4.6).

A drawing of the 1995 magnet is given in Fig. 4.7. The magnetic field can be set up to 5.9 T, currently the field is at about 5.258 T (see section 6.3.2). The field is created in a combination of two superconducting solenoids that consist of a single-filament wire of niobium-titanium. In addition several correction coils that allow to cancel higher order magnetic field terms are installed in the magnet. The solenoids and the correction coils are

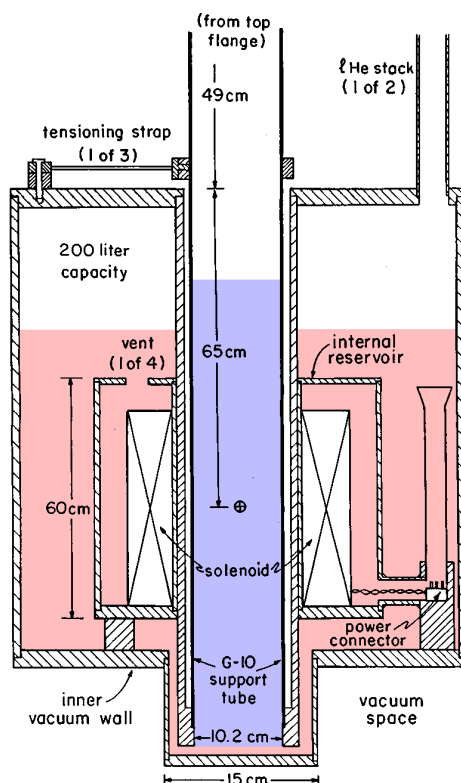


Figure 4.7: Drawing of the Nalorac 1995 liquid helium cryostat.

charged via a 24 pin electrical connector.

The solenoids sit in a separate part of the 200 ℓ reservoir of liquid helium. The reservoir is isolated by several layers of insulation. First there is an isolation vacuum that is originally (before cryopumping sets in) pumped to about 10^{-2} mbar. Then an aluminum heat shield is installed. Another shield is given by a liquid nitrogen reservoir at 77 K, that again is shielded by an aluminum heat shield. Around this reservoir about 100 layers of superisolating foil are wound and again the volume to the outer magnet housing is part of the isolation vacuum.

The experiment can be lowered into the 102 mm diameter bore, that is connected to the reservoir of the coils. This bore is either closed by a flange with attached heat shields or by the header of the experiment. The liquid helium reservoir is kept at a pressure of about 50 hPa above the outside pressure in order to prevent air from entering the magnet. However, during the filling of the magnet, and the lowering and raising of the experiment, it is inevitable that some air gets trapped in the magnet. This air forming ice inside the cryostat has been a major problem in the operation of the magnet. Already during the shut-

down of the magnet in Seattle, it was realized that ice had accumulated in the funnel that guides the charging stick to the power connector. Hence, it was impossible to decharge the magnet in a controlled way and the magnet had to be quenched. Basically, the same happened during the charging of the magnet in Heidelberg. At a magnetic field strength of about 5.3 T the charging stick was removed and could not be reinserted to the power connector due to pieces of ice between the pins. Hence, no corrections to the higher orders of the magnetic field could be carried out, resulting in a homogeneity of $1 \cdot 10^{-5}/\text{cm}^3$ recently measured with an NMR probe [Tre11]. Another air ice related problem concerns the liquid helium filling stacks. In one of the stacks a liquid helium level sensor is mounted. This stack cannot be opened any longer as the sensor seems to be frozen to the wall. In order to prevent ice from blocking the remaining liquid helium filling stack, the air ice accumulating there, is always removed by a metal stick before filling the magnet.

Magnetic field correction coils

Around the trap tower, but outside the vacuum envelope, a set of home-made correction coils is wound. In total there are five coils: one set of three coils and one set of two coils. With this configuration, together with a home-made constant current source, the B_1 and B_2 terms of the magnetic field can be compensated. Without the traps inserted an NMR measurement determined $B_1 \approx 0.1 \text{ mT/m}$ and $B_2 \approx 0.2 \text{ T/m}^2$ at the position of the experiment trap. The design values for the compensation are $\Delta B_0 = 3.8 \text{ nT/mA}$, $\Delta B_1 = 1.7 \text{ mT}/(\text{mA}\cdot\text{m})$ and $\Delta B_2 = 59 \text{ mT}/(\text{mA}\cdot\text{m}^2)$ [Zaf07]. Several mA of current can be inserted into the coils. So far, they have not been used together with the experiment.

4.1.4 Mechanical arrangement and vacuum components

The mechanical arrangement of the setup is crucial for the experiment for many different reasons. First of all, the setup sits in a strong magnetic field, so that magnetic components can significantly distort measurements of the cyclotron frequency by adding higher order terms to the magnetic field (see Eq. (3.51)). Secondly, the alignment of the electrostatic field of the trap with respect to the magnetic field causes shifts in the eigenfrequencies of the ion (see Eq. (3.61)). And thirdly, ultra-high vacuum (better than 10^{-12} mbar) is needed in order to avoid ion losses due to rest-gas collisions.

Vacuum envelope and pumps

The overall mechanical arrangement of the experiment is illustrated in Fig. 4.8. The vacuum envelope consists of the vacuum chambers of the external ion source, the beam line and the trap chamber. The ion source chamber is made of standard stainless steel vacuum components. On top, an Alcatel ATH-30 turbo pump with a pumping speed for N_2 of 30 l/s is mounted on a CF63 flange. As an alternative, in case of maintenance, an Oerlikon Leybold Turbovac SL 80 pump with a pumping speed for N_2 of 65 l/s is available. The

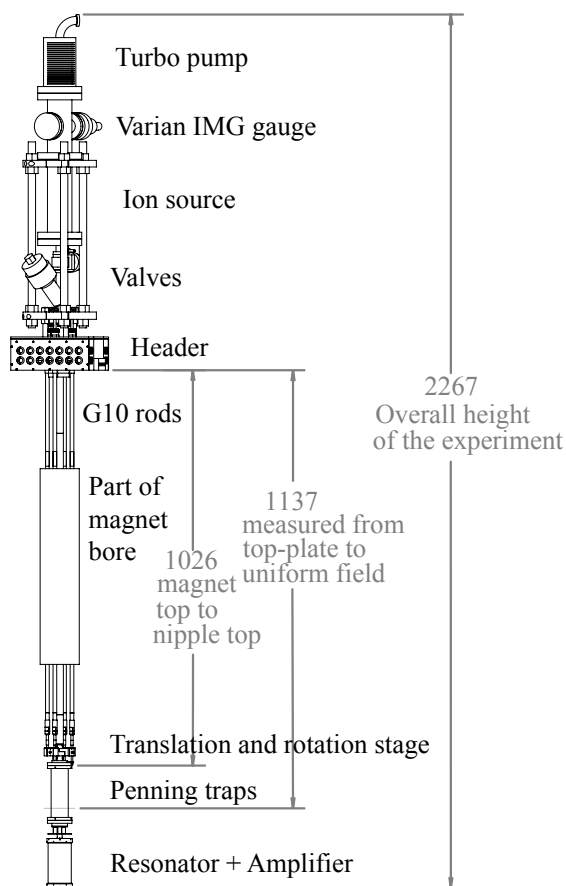


Figure 4.8: Overview on the mechanical arrangement of the setup. All lengths are in mm.

prevacuum is maintained by an Edwards XDS 5 or 10 prepump (the two pumps are used as replacement to each other) with a pumping speed of 5 or 10 m³/h, respectively. At the ion source chamber also an inverted magnetron gauge Varian IMG-100 is mounted. Typically the vacuum in the ion source chamber is around $1 \cdot 10^{-10}$ mbar, when the experiment is inserted into the magnet. However, during the lowering of the experiment this value can fluctuate a lot, which points towards some disturbance of the gauge by the stray field of the magnet. The prevacuum is measured at the pump with a Pfeiffer Pirani gauge TPR 280. It typically has a pressure of $1 \cdot 10^{-2}$ mbar.

While the ion source chamber sits outside the magnet at room temperature, the rest of the vacuum envelope is located inside the magnet cryostat. These two temperature regions can be separated by two valves. One of the valves is computer-controlled and is part of the automated loading procedure. Inside the cryostat the vacuum is maintained by the cryopumping effect of the cold surfaces. These surfaces adsorb all neutral gas atoms and molecules except for H₂ and He. As no gauges exist that can measure pressures as small as obtained by this effect, the vacuum can only be estimated to be below 10^{-13} mbar by

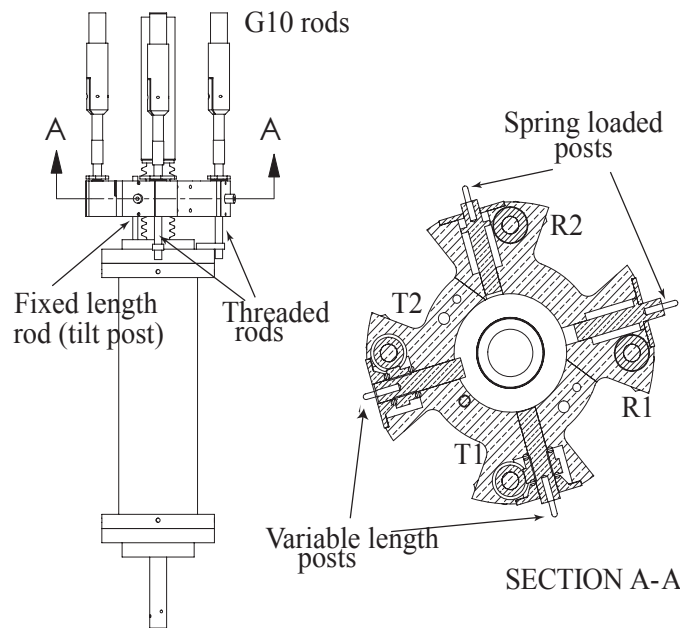


Figure 4.9: Drawing of the rotation and translation stage of the experiment. For details see text.

measurements of the storage time of ions in the Penning trap [Str11].

The beam line is made out of CF20 stainless steel standard vacuum components. As the magnetic environment of the traps is in particular crucial, a special material is utilized for the trap envelope: aluminum bronze C642, which is iron-free. As the trap envelope was custom-made by the workshop of the University of Washington also special OFHC copper vacuum seals, based on the TriSeal standard, are utilized. So far, they have shown good sealing properties both at room-temperature and in the cryogenic environment. However, as a drawback the seals have to be custom-manufactured in the workshop.

Translation and tilt of the experiment

As already discussed in section 3.4.2, it is important to align the experiment properly. Due to the contraction of all components that are immersed into the liquid helium, it is also necessary that this alignment can be changed in-situ. For this purpose, a tilt and translation system is installed (see Fig. 4.9). At the experiment header, four rods, made of G10 compound material, are mounted that can be turned by the experimenter. Two rods (T1, T2) provide the ability to translate the system in the x - and y -coordinate. This is achieved by a custom-made gear by pushing the translation stage away from the wall. The gear ratio is $39.6 \mu\text{m} / \text{turn}$ of the rod and the two rods are mounted such that the movement in x and y is orthogonal. The other two rods (R1, R2) provide the tilt of the experiment by turning screws that are mounted between the tilt stage and the trap chamber. The tilt angle is de-

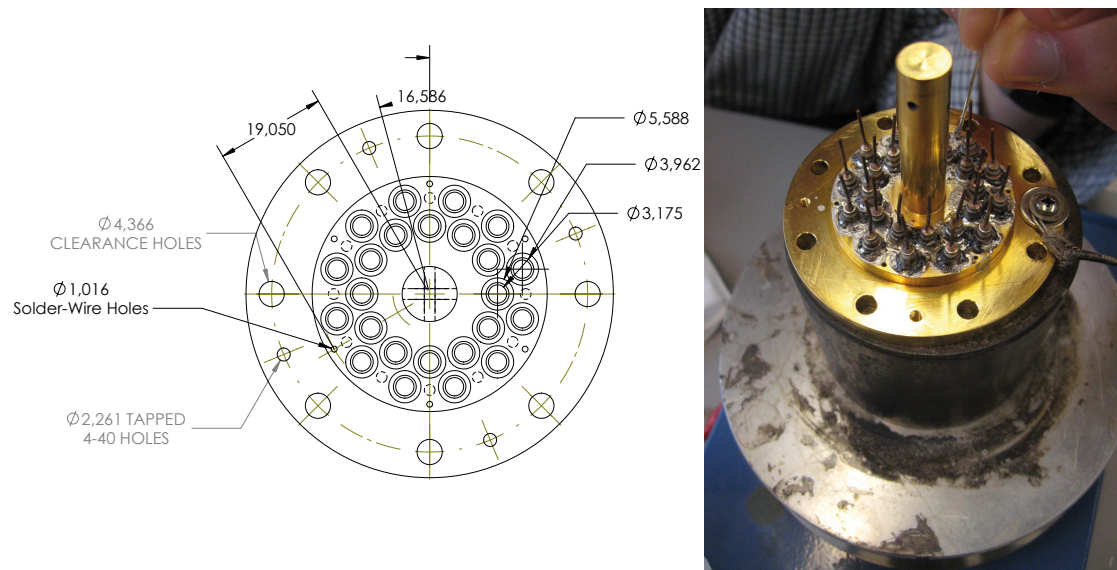


Figure 4.10: One of the spare flanges with the feedthroughs to the trap. Lengths are in mm.

terminated by a tilt-post that is mounted off-axis and keeps a definite distance between the trap chamber and the tilt stage. This forms a tripod with two different lengths of the legs. One turn of the rods is supposed to change the angle by 1° . Unfortunately, at the same time the experiment trap is translated by 2.3 mm, which needs to be corrected by the translation stage. The maximum possible tilt is limited to 2.4° . At this angle the experiment hits the walls of the magnet bore. Several methods to measure and optimize the alignment of the traps have been tested (see section 6.1.3).

In the translation and tilt stage of the experiment a number of custom-made ball bearings are utilized. Originally ruby balls were in use, but it turned out that these can easily be crushed by the forces in the translation stage, and so they were replaced by more resistant brass balls.

4.1.5 Feedthrough of electronic signals to the traps

A very important point for the experiment is the transport of electronic signals to the trap and vice versa. First of all, the signals have to get into the magnet bore, which is realized by the header. Here, leak-tight BNC feedthroughs are utilized as inside the bore there is an overpressure of about 50 hPa. From the header semi-rigid coaxial cables (except for the ring voltage and the corrections coils, where twisted pair cables are utilized) guide the signals to the trap. Here, the next challenge is to conduct the signals into the vacuum of the traps with the additional complication of a cryogenic environment. The solution is a custom-made OFHC copper feedthrough flange (see Fig. 4.10) with 24 feedthroughs

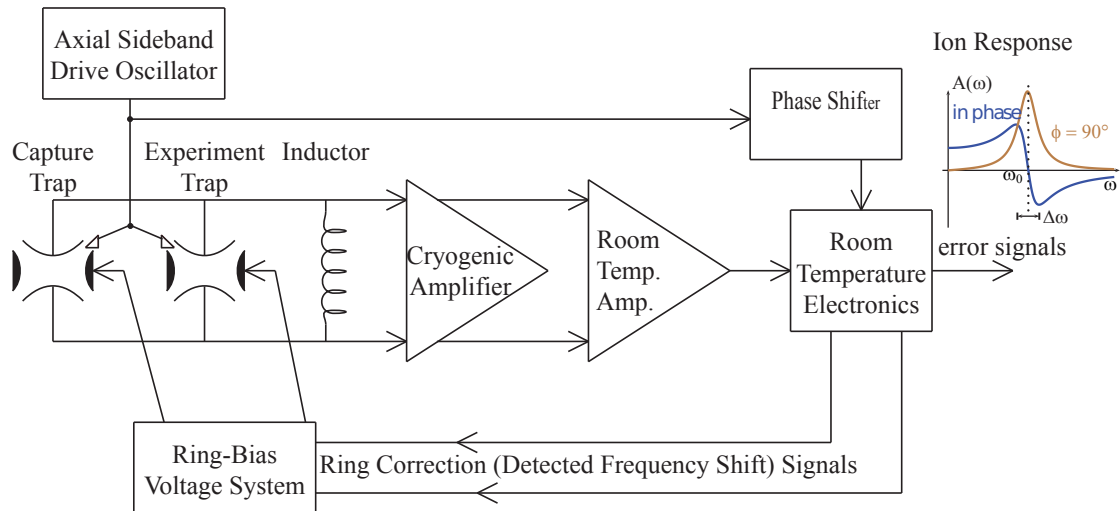


Figure 4.11: The basic detection scheme including two traps.

out of which 19 are connected. The feedthroughs are made by Ceramaseal and have alumina insulated rings brazed to copper inner conductors. Their sleeve is made from an alloy of 70% copper and 30% nickel. The feedthroughs were silver-soldered into the flange in an induction furnace. The feedthrough flange has introduced quite some experimental challenges both in Seattle and in Heidelberg. Already in Seattle, several feedthroughs did not withstand the cryogenic environment and developed cold-leaks. Therefore, three of the feedthroughs were encased in indium solder. But in Heidelberg another cryo-leak developed and fixing this problem cost several months of experimental time. Therefore, two replacement flanges were gold-plated and equipped with feedthroughs, utilizing soft-soldering on a hot-plate. The solder alloy utilized consists of 96.5% tin with an admixture of 3.5% silver that can be soldered at about 230 °C. Both replacement flanges were already tested with the experiment in the 4-K environment and did not show any vacuum problems.

4.2 Electronics

In order to meet the specific conditions for high-precision Penning trap experiments (tiny signals, cryogenic environment, high stability) it is often necessary to utilize custom-made solutions for the electronics of the experiment. E.g. all detection electronics were specifically designed for this experiment. The details of this electronics can be found in the thesis of Pinegar [Pin07], here only the basic concepts will be discussed.

The basic idea of the detection concept has already been presented in the sections 3.3 and 3.6.2. In this experiment, only the axial motion is detected directly, while the radial motions are detected via their couplings with the axial motion. All parameters of the system are chosen such that the axial frequency will be around 4 MHz, well above the $1/f$ -noise

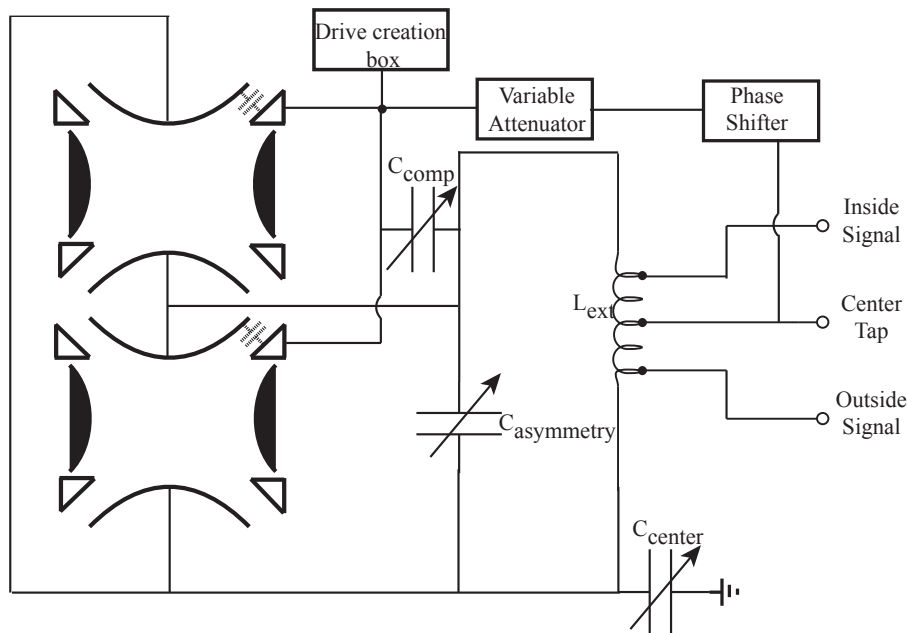


Figure 4.12: Concept of the external tuned circuit for a double-Penning trap configuration. Additional tunable capacitors are added for tuning the center frequency (C_{center}) and the asymmetry ($C_{asymmetry}$) of the differential arrangement. Their exact position depends on the asymmetry between the two differential inputs of the amplifier and hence can be either on the “inside” or the “outside”. Two possibilities for the compensation of the coupling of the external drive onto the tuned circuit exist: A tunable capacitor (C_{comp}) to symmetrize the coupling and a direct feedthrough of the attenuated and phase-shifted signal onto the amplifier.

corner of the utilized field effect transistors (FETs). The basic concept for the two trap case is illustrated in Fig. 4.11. The traps together with an inductor form the external tuned circuit for the ions. A cryogenic and a room-temperature amplifier stage amplify the signal from some nV up to some hundred mV. In order to detect a sufficiently large signal, the ions are driven at a side-band of their axial frequency. This sideband is created by modulating the ring-voltage. Room-temperature electronics picks the part of the signal within a certain bandwidth and at a specified phase with respect to the drive signal in order to create the error signal (the shape was already discussed in Eq. (3.41)) for the axial detection. For the detection of the radial modes, the frequency is locked to the zero-crossing of the error signal by applying a correction to the ring voltage.

Parameter	Typical value
Trap capacitance C_t	20 pF
External inductor L_{ext}	80 μH
Equivalent parallel resistance R_p	2 M Ω
Resonance frequency ν_{LC}	4 MHz
Quality factor Q_{ext}	1000

Table 4.2: Typical parameters of the tuned circuit. For details see section 3.3.1.

4.2.1 Trap connections and external tuned circuit

The external tuned circuit of the traps (see Fig. 4.12) is mainly formed by their capacitance to ground C_t and an external inductor L_{ext} (for typical values see Tab. 4.2). This commercially available air-coil inductor is housed in a gold-plated copper shield. The traps are connected such that two input signals are created for the differential amplifier. The signals from the inner endcaps of the traps create the “inside signal” and are connected to the upper part of the inductor. The signals of the outer endcaps of the traps create the “outside signal” and are connected to the lower part of the inductor. The termination of the endcaps was varied during the course of this thesis: For tests related to the ion transfers a system to switch the resistance to ground based on anti-parallel diode pairs was connected to the traps (for details see the diploma thesis of Höcker [Höc10]). For most of the ion work shown in chapter 6, this network was removed (originally for test purposes related to a noise problem) and the endcaps were kept at DC ground.

In order to tune the center frequency of the external tuned circuit and the asymmetry between the two halves of the detection system a variable capacitor to ground (C_{center}) and one between the “inside” and the “outside” ($C_{\text{asymmetry}}$) were inserted. As tiny changes in the capacitance (the total capacitances of the variable capacitors usually was on the order of 1-2 pF, while the changes were some percent of this) were needed, custom-made trim capacitors were utilized. However, the tuning of the frequency turns out to be quite unpredictable, when immersing the setup into liquid helium. Changes are expected due to the temperature change and the change in permittivity, but the center frequency of the tuned circuit fluctuates between 15 and 50 kHz quite randomly. The reasons for that can only be guessed but it might be due to mechanical differences for every lowering.

As the exact center frequency of the tuned circuit can be somewhat variable (within the range of the filters utilized in the drive system of about 100 kHz), this is not a major problem. However, often noise spikes are present on the tuned circuit at specific frequencies and can disturb the measurement procedure. So it is important to still be able to tune the center frequency, when the experiment is inside the magnet. This is realized by changing the source currents of the cryogenic amplifier. Changes here change the input capacitance of the transistors, which also contributes to the tuned circuit. Using this method changes on the order of 10 kHz are possible and sufficient.

4.2.2 Drive system

Several different drives can be applied to the ions in the trap, e.g. the axial drive, a drive at the modified cyclotron frequency or the cooling drives. All drives in this experiment are applied via the guard electrodes as all endcaps are part of the detection system, in contrast to the earlier UW-PTMS, where one endcap was utilized for the drive and one for the detection. The application via the guards in principle has the advantage, that the drives can be applied in a dipolar or quadrupolar configuration as the guards are split into halves. However, as the guards are situated close to the endcaps, which are utilized for the ion signal detection, capacitive coupling here is a major problem. Therefore, additional capacitors to tune out the coupling are utilized. As this tuning has been somewhat unstable (as in the case of the other tunable capacitors described in the last section), when lowering the experiment into the liquid helium, a simplified scheme, where all drives are applied to one of the guards is utilized. This also means that only one tunable capacitor (C_{comp} in Fig. 4.12) is necessary. So far, no limitation of this drive scheme became apparent.

Drive creation

All drives, except for the axial, are created directly by setting the output of a frequency synthesizer. Mainly PTS frequency synthesizers already in use with the Seattle experiment are utilized. They feature the possibility to use one synthesizer to fine-steer the output of another synthesizer and hence allow for a very fine setting of the frequency down to nHz. In addition, an Agilent 33250A arbitrary waveform generator was tested as the steering here is more flexible. Both synthesizers worked fine, a comparison of their specifications is given in Tab. 4.3.

The axial drive creation is more complicated and is directly linked to the phase-sensitive detection system. This imposes some requirements on the drives:

- The frequency step-size of the drive should be well-below the axial width of a single ion (≈ 100 mHz).
- The phase of the drive must be tunable with respect to the phase of the detection.
- The drive should not disturb the axial amplifier and hence needs to be off-center of the tuned circuit's center frequency.
- Two separate drives are needed in order to detect ions at different frequencies in the different traps.

Implementing solutions for all points results in the drive scheme of Fig. 4.13. Most of the operations shown here are carried out in a single box, called the mixer box. In a first step two different, so-called beat frequency oscillator (BFO), signals at a frequency around 100 kHz are created. In order to achieve a high-axial resolution, the 52 MHz output (V_{NBFO}) of two PTS synthesizers (called NBFO's) is divided by a factor of $N = 520$

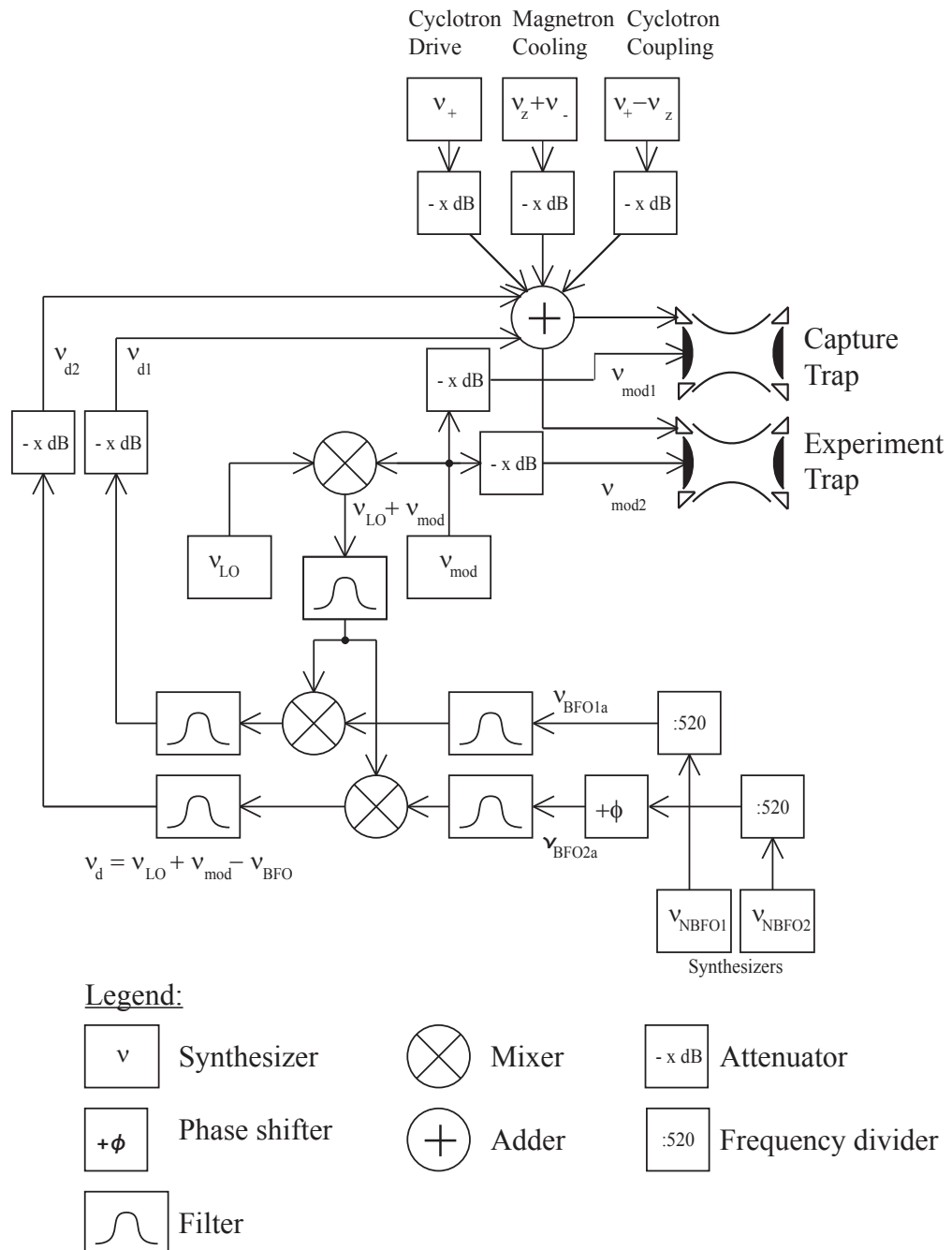


Figure 4.13: Drive scheme for the double-Penning trap. The axial drive is created by the combination of several synthesizer outputs, while the other drives are directly taken from the synthesizers. For more details see text.

Specification	PTS 160	Agilent 33250A	Quartzlock A8-M
Output frequencies	0.1-160 MHz	0-80 MHz	1, 5, 10 MHz
Frequency resolution	0.1 Hz	1 μ Hz	-
Frequency accuracy	-	-	$5 \cdot 10^{-14}$
Switching time	20 μ s	100 ms	-
Spurious output	-75 dB	-50 dB	-70 dB
Harmonic output	-35 dB	-30 dB	-60 dB

Table 4.3: Specifications of synthesizers and the frequency standard in use with the experiment.

(v_{BFO}), resulting in a frequency resolution of 1.9 mHz. The BFOs can be set to different frequencies, so different ions can be driven. To shift the phase of the drive with respect to the detected signal, phase shifters are installed, which can change the phase in steps of $(360/520)^\circ$. In order not to disturb the axial amplifier, it is necessary to shift the drive signal (v_d) from the detection frequency. This is achieved by modulating the ring-voltage with a 125 kHz signal (v_{mod}) and thus creating a side-band of the axial motion, where the drive can be applied. This sideband drive at 4.125 MHz is created by mixing a local oscillator signal at 4.1 MHz (v_{LO}) with the modulation signal and the BFO signals. In practice, the LO signal is tuned such that its frequency is 100 kHz above the center frequency of the tuned circuit, while the BFO signal is only changed in a small range around 100 kHz and the modulation signal remains unchanged. The ion's frequency is tuned via the ring voltage.

Axial drive compensation

As already mentioned above, the coupling of the axial drive signal (or any other signal) onto the axial amplifier is quite undesirable as it will hide the real signals from observation. A first important technique to avoid this problem has already been discussed with the introduction of a sideband drive. However, not only signals directly at the center frequency of the detection, but also several 100 kHz away still disturb the amplifier. The main source of coupling of these signals onto the amplifier comes from the parasitic capacitances between the guard electrodes and the endcaps. In order to compensate for this effect, two different approaches have been implemented into the setup as illustrated in Fig. 4.12. The first approach tries to balance the capacitive coupling by addition of tunable coupling capacitors (C_{comp}). The second approach feeds back an inverted part of the signal onto the amplifier in order to cancel the signal that is already fed through. The performance of both approaches will be discussed in section 6.1.2.

Frequency standard

The frequency stability and accuracy of the synthesizers is of great importance for the measurement technique. In fact, earlier measurements in Seattle were finally limited by the quartz-based frequency standard (see [Pin07]). Therefore, a GPS-disciplined Rb frequency standard, the Quartzlock A8-M, with a frequency stability of better than 1 part in 10^{11} on all time-scales longer than 1 second, is in use with the experiment now. The GPS antenna of the standard sits on top of the roof of the Gentner building in a plexiglass box. From there it is connected via 50 m of RG58 cable with the laboratory. The orientation of the antenna must be southwards. This direction is not quite ideal due to the hill-side close to the institute. Therefore, the standard sometimes loses track of the satellites. However, so far no limiting effect on the experiment could be observed. The specifications of the frequency standard are summarized in Tab. 4.3.

4.2.3 Axial amplifier

As typical voltage drops created by single ions across the inductor are on the order of nV, additional amplification of the signal is necessary. Therefore, several stages of amplification are implemented. In order to improve the signal-to-noise ratio of the first stages of the amplifier and the Q -value of the tuned circuit, these are immersed in the liquid helium bath of the magnet as well. At cryogenic temperatures special care has to be taken for the choice of the components utilized as in standard silicon-based transistors the charge carriers are frozen out at this temperature. Instead, GaAs-based field effect transistors are utilized, in this case Agilent ATF, that are normally used in cell phone applications. The exact amplifier design is discussed in detail in the thesis of Pinegar [Pin07]. Both traps share the same amplifier. The amplifier is designed as a differential amplifier, one input takes signal from the “inside” endcaps (EtCap and CbCap), the other from the “outside” endcaps (EbCap and CtCap). A third stage of amplification for the 4 MHz signal is outside the cryostat at room-temperature. A more specific characterization of the amplifier is planned.

4.2.4 Room-temperature electronics and frequency lock

As shown in Fig. 4.14, the 4 MHz axial signal created by the driven ions (for the drive creation see Fig. 4.13) is mixed with the local oscillator signal (v_{LO}) in order to create a signal at the frequency of the beat frequency oscillator (v_{BFO}). By convention in electrical engineering, this signal is called intermediate frequency signal (IF). This signal is filtered and amplified again in a box on top of the magnet. Then it is transferred to the Mix-to-DC-box, where all detection signals of the experiment are created. The error signal of the axial detection (see Eq. (3.40)) is created by mixing the IF signal with a phase-shifted BFO signal and filtering the resulting DC-signal with a variable low-pass filter (0.3-300 Hz bandwidth). In addition, a non-coherent detection is possible by utilizing a root-mean-square (RMS) detector. This allows to determine the gain profile of the tuned circuit in the noise. In order to lock the axial frequency, which is necessary for the triggered

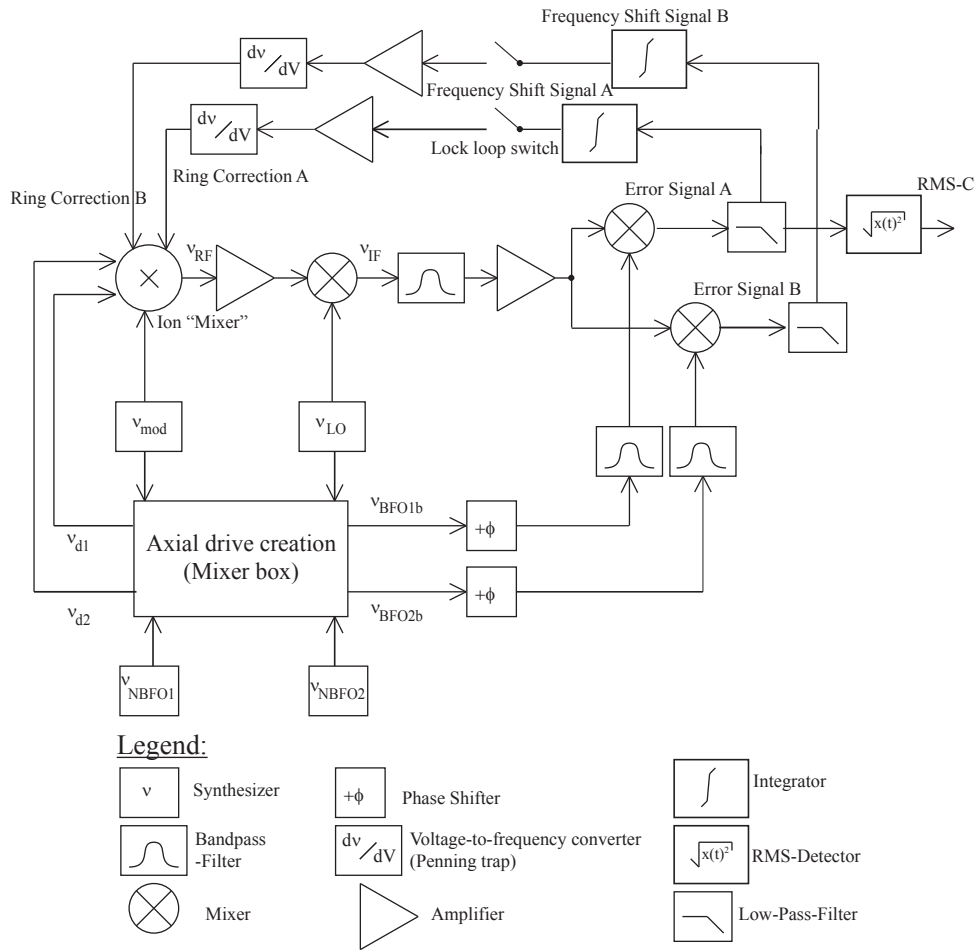


Figure 4.14: Overview on the detection system. The ion signal at 4 MHz is mixed down to a DC-signal. This signal can be utilized to lock the ions at a fixed frequency. For more details see text.

radial detection technique (see section 3.6.2) a phase-locked loop [HH89] is utilized. In this loop the ion in the Penning trap acts like a voltage-controlled oscillator. The control voltage is synthesized by the error signal, which is fed into a variable integrator (0.1-30 Hz bandwidth), then digitized and applied to a correction DAC (digital-to-analogue converter) in the precision voltage source, that applies a correction to the ring voltage:

$$V_{\text{ring}} = V_0 + V_{\text{corr}} \quad . \quad (4.2)$$

This correction keeps the ions at a fixed axial frequency defined by the zero-crossing of the error signal. Six correction ranges for the DAC can be chosen (from 20 mV full-range down to 66 μV full-range). Experimentally, so far only ranges down to 660 μV could be utilized as the locked loop was not stable enough in the smaller ranges. It was also found

that the nominal ranges do not exactly agree with the real ranges (e.g. the nominal 2 mV range utilized for most of the measurements only has 1.7 mV range in reality).

4.2.5 Voltage sources

In order to perform the $^3\text{H}/^3\text{He}$ mass measurement, several voltage sources are necessary. For all but the ring and the correction electrodes, the stability requirements are quite relaxed. In the original setup, most of these voltage sources were single-channel Fluke 415B power supplies that could deliver up to 5 kV. These were replaced by one CAEN crate SY1527LC equipped with an A1511B card that has 12 output channels, which can deliver 500 V each. These channels can be floated independently with respect to ground and with respect to each other, which is important for the voltage scheme of the external ion source. The CAEN power supply right now controls both the external ion source and the field emission point. In principle, it can also be utilized for wide-range voltage sweeps of the ring voltage. For more precise ring voltage sweeps, its resolution of only 100 mV per step is not sufficient. Here, either the precision voltage source or a Fluke 415B together with a fine-tunable custom-made analogue 10 V power supply are utilized.

For all precision ion work the custom-made ring voltage source is utilized [PBB⁺09]. It is based on a cascaded string of buried Zener diode 10 V references and is specified to achieve a voltage stability of below 1 part in 10^8 on all time-scales below 10^4 s. Within a span of 10 V, the power supply can be scanned in steps of $0.76 \mu\text{V}$. So far a voltage span of -80 V to -90 V was chosen as ^3H and ^3He are in resonance with the detector at about -89 V. The voltage source is an integral part of the locked loop (as explained in section 4.2.4). This means that the lock in principle only can be established utilizing the voltage source in the -80 V to -90 V region (without major modification of the voltage source). The voltage source is also attached to a precision voltage divider that delivers the voltages of the guard electrodes. In order to circumvent the -80 to -90 V limitation for the precision ring voltage, the output of this guard voltage divider has also been utilized as a ring voltage source and a lock for protons (≈ -30 V) could be established. The performance of the voltage source together with ions is discussed in section 6.3.1.

4.3 Automation and data acquisition

The original Seattle UW-PTMS already had a computer-control for the cyclotron data-taking, but apart from that the system relied on a highly-skilled experimenter, trained on the system for many years. Also, the system was based on an archaic Fluke experiment controller in combination with a NEXT computer system. Both systems are outdated for many years and so it was decided already in Seattle to migrate to a new computer-control system. This system is based on ordinary personal computers with the software LabWindows/CVI. This software is basically a C-compiler with additional libraries, drivers and a graphical user interface editor. It is specifically designed for the control of scientific in-

struments. It is distributed by National Instruments, which also produces the more popular LabView software. However, the support of both products is similar. In Seattle, the experiment control system for the new spectrometer, called Controller, was developed to the point, where most individual components of the setup were included in the software. However, apart from that, Controller had very little additional functionality, such as predefined procedures. Therefore, in Heidelberg a major redesign of Controller was started aiming in automating as many functions as possible in order to avoid errors of the experimenters and improve the time usage of the experiment by allowing for over-night measurements. This redesign also includes the replacement of all instruments, where the experimenter still has to turn knobs manually. The final goal of this still ongoing evolution is the full automation of single ion creation and the subsequent frequency measurements with only very little supervision by the experimenter.

4.3.1 Controller user interface

For the experiment about 50 different instruments and even more parameters have to be computer-controlled. Part of them are custom-made, such as the detection system, others are commercial instruments like the frequency synthesizers. In addition, not all instruments can be controlled by the same hardware interface. Obviously, these boundary conditions result in a quite complex program. The original version of Controller converted this complexity into a user interface that basically showed all instruments on one page and allowed full flexibility in the control of all components. While this was useful in the testing phase for all these components, it induced too much complexity to the work with the ions. In addition, new functions for the automation of many experimental procedures, were introduced and also occupied parts of the limited space on the screen. Therefore, Controller was converted into Controller 2.0. Now, only higher-level functionality and instrument controls that still have to be changed quite frequently by the experimenter are included in the front panel of the user interface. Most of the direct experiment control was moved to pop-up panels that can be opened from the front panel. This results in reduced complexity of the “every-day” user interface, while the underlying program routines are more powerful due to the automation of many experimental procedures.

4.3.2 Control architecture

The control system is centered around a personal computer (also called Controller). It acts as a GPIB controller and also controls computer cards that create logical output signals for the custom-made electronics. In addition it also acts as a server for the instruments controlled via ethernet. Fig. 4.16 shows a diagram of all the hardware controlled by Controller.

All synthesizers and the data acquisition devices, such as the multimeters and the oscilloscope are controlled via GPIB. The custom-made electronics and the precision ring voltage source is controlled by digital-to-analogue converters that get logical signals from the NI 6509 cards. The CAEN power supply is controlled via ethernet.

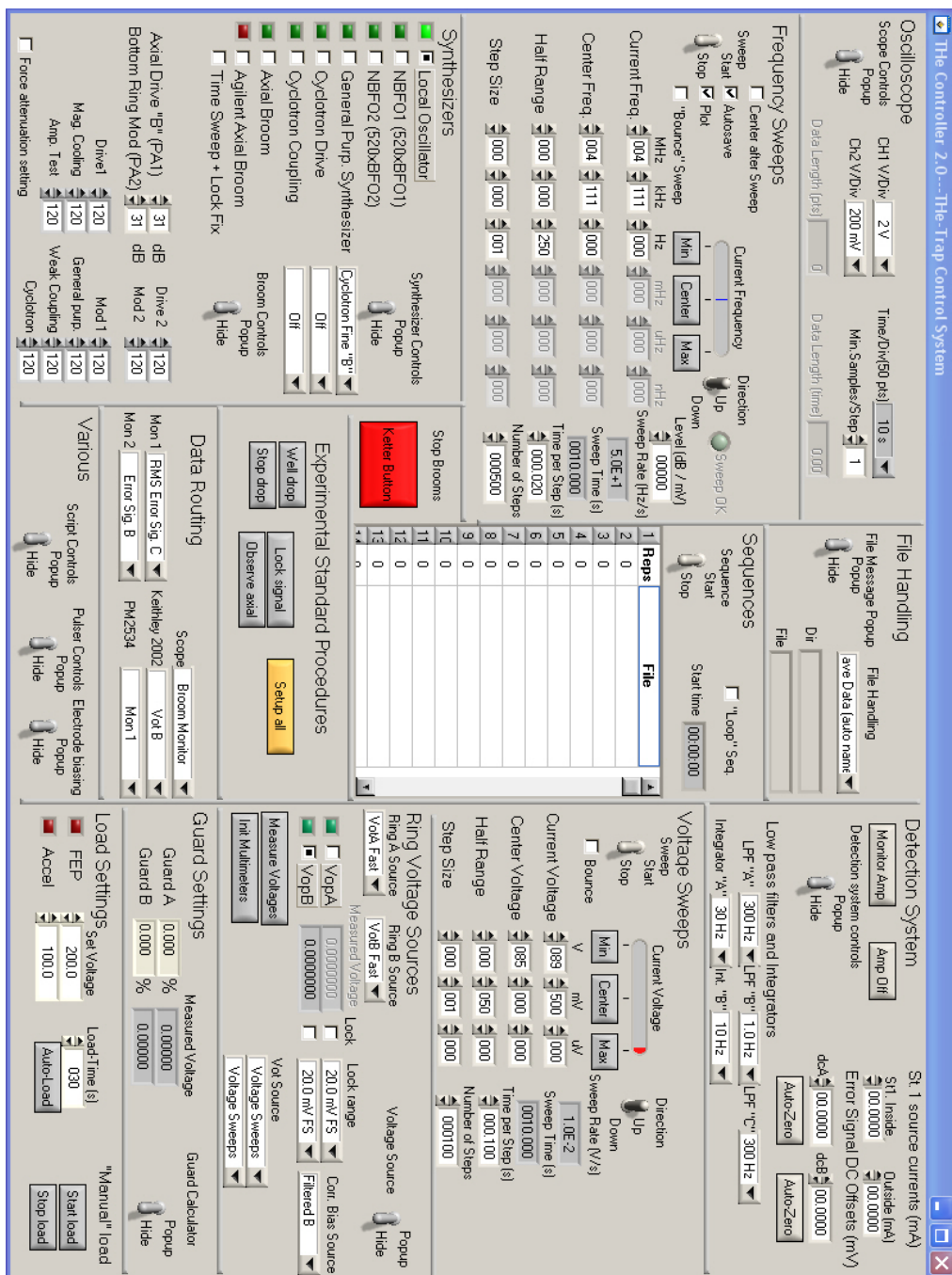


Figure 4.15: Screenshot of the experiment control program Controller 2.0.

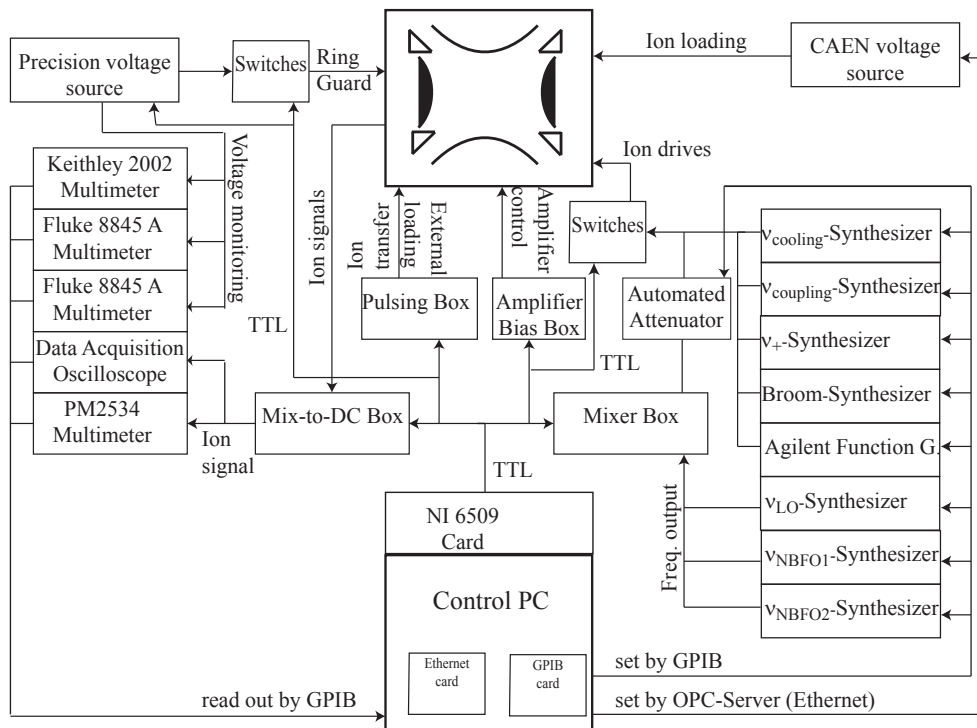


Figure 4.16: Architecture of the computer control system of the experiment.

4.3.3 Data acquisition and automated analysis

Several devices are available for the data acquisition. The standard case is the acquisition of a voltage (e.g. the error signals created in the Mix-to-DC box) as a function of a changing synthesizer frequency. Here, the digitization of two input channels is achieved by an Tektronix TDS410 oscilloscope. The data digitization of the oscilloscope is synchronized with the sweep of the frequency synthesizer and afterwards the data are exported to the program and automatically saved. In addition, all settings of Controller are saved and the voltages of the ring and guard electrodes are read out and saved to another file. The data files are called `.THed` files, while the settings are saved to `.THes` files. As huge amounts of data are accumulated this way over time, a standardized naming scheme was introduced. The file name includes the time the data were taken and the name of the two channels that were saved. They are saved in a folder structure that reflects the day, the month and the year the data were taken. For the analysis of the data, Controller has the functionality to start a MatLab-Script called `THEPlotter.m` [Höc13], which plots the data. Depending on the nature of the data, an automated fit algorithm is utilized, e.g. to fit the axial line-shape to error signal data. For a later reanalysis of the data, a graphical user interface is available that allows a variety of options for the plotting of the data, e.g. subtraction of offsets or merging of data from the settings files.

For the acquisition of a voltage versus another voltage, the original hardware xy-Plotter

was replaced by a small subprogram of Controller that reads out the multimeters that monitor the ring and guard voltages and the outputs of the mix-to-DC box. For the digitization of the voltages two Fluke 8845A (6.5 digit precision), a Keithley 2002 (8 digit precision) and a Philips PM2534 (6.5 digit precision) multimeter are utilized.

4.3.4 Automation of experimental standard procedures

The main changes to Controller regarding its functionality are in the field of automating procedures that have been previously tested manually by the experimenters. Where this was not possible with the existing hardware, new hardware was purchased or developed. One example is the switches utilized for switching the biasing lines of the experiment.

Auto-setup of controlled instruments

In order to avoid clicking through all controls of the Controller program an automated setup of the components has been introduced. Included is the possibility to load the values of all synthesizers and the amplifier settings from a specific .THes-file. This greatly speeds up the start-up procedure of the program and minimizes the risk of forgetting to set up important components of the experiment.

Automated ion loading

Originally, for loading the trap with the field emission point two power supplies had to be switched on and BNC connections to the trap had to be changed. Therefore, the CAEN power supplies were purchased and additional automated switches were added to the experiment. The automated loading procedure takes care of all the steps mentioned above and the experimenter only has to select the voltages and the loading time. This also makes the different loads more repeatable compared to the earlier procedure.

Voltage sweeps

Previously, sweeps of the precision voltage could only be performed in a very crude way by Controller, while sweeps of the non-precision voltage source only could be performed with a special manual sweep box. Therefore, a refined voltage sweep engine was included into Controller. This can sweep the precision voltage source over the full 10 V range in μV steps and the CAEN power supply in 100 mV steps. In addition, a calibration measurement of the precision voltage source is possible, in order to synchronize the voltage settings in Controller with the measured voltages.

Sequences of frequency sweeps and broom interface

For the preparation of the ion and in particular the sweeps to determine the modified cyclotron frequency it is important to be able to run several frequency sweeps with different

synthesizers in a row. Therefore, the possibility to run through a list of predefined sweeps was introduced into the program. These sweeps are also saved as .seq-files so that they can be loaded again. Another very important application related to sweeps is the utilization of contamination ion removal techniques, so-called brooms. As the frequency of these brooms depends on the voltage settings of the experiment, a tool that can auto-generate broom sequences was integrated into Controller. This results in a big improvement compared to the original Seattle setup, where the experimenter had to set the broom frequencies of the different ions manually.

The-Script scripting language

In order to further improve the automation of Controller just recently a scripting language, called THe-Script [Str12], was developed that allows to control the complete user-interface of Controller automatically. The scripting language includes conditional programming and loops, and hence is a powerful tool for further steps of automation. With well-written programs in THe-Script combined with MatLab data acquisition and analysis programs, it should be possible in the future to automate almost all experimental procedures.

Calculator subprograms

Often it is important to predict the voltages or frequencies, where the ion signals are expected. In order to avoid calculating these frequencies by hand, a MatLab program was written. It calculates the frequencies of all ions in all charge states up to chlorine. In addition, it also can create sweep files with these calculated frequencies. Another subprogram of Controller allows to adjust the precision ring voltage such that the axial ion resonance is centered on the tuned circuit.

5 The Heidelberg tritium laboratory

In order to be able to perform precision measurements on the mass ratio of ^3H to ^3He , a dedicated laboratory was installed at the Max-Planck-Institut für Kernphysik. First of all, the laboratory was equipped for the use of gaseous tritium, which entailed a lot of regulative and constructional efforts. Secondly, the existing laboratory rooms were revamped for precision measurements by installing a number of environment stabilization systems and avoiding the use of magnetic materials. And thirdly, the laboratory was also prepared to cater for the specific needs of the already existing Seattle spectrometer.

5.1 Tritium safety concept

From the point of view of radiation safety, tritium has ambivalent properties. On the one hand, its decay is very low in energy (6 keV average electron energy) and the β -electrons can therefore be easily shielded. On the other hand, this low energy makes it hard to detect a tritium contamination as no personal dosimeters are available at this energy range. In addition tritium is gaseous and therefore harder to contain than most radioactive substances and already small amounts can have high activities due to its short half-life of only 12.32 years [LU00]. The biological risk of tritium mainly lies in the incorporation of the gas via the lungs and the human skin. After incorporation, it has a biological half-life of only 10 days, due to the precipitation of tritiated urine. The dose per time for an average person breathing tritium is given as

$$D = C_{\text{tritium}} \cdot DF \cdot BR \quad . \quad (5.1)$$

Here, C_{tritium} is the activity concentration of tritium in the air, DF is the dose factor and BR is the breath rate. The dose factor is given as $DF = 1.8 \cdot 10^{-8}$ mSv/Bq [Sch08] and the breath rate is assumed to be $BR = 0.033$ m³/min through the lungs and the skin. Assuming a homogeneous distribution of all available tritium (of 185 GBq) in the 45 m³ large experiment room this results in a dose per time of 2.5 mSv/min. Comparing this to the average radiation exposure per year of about 3 mSv makes it clear that it is of paramount importance to prevent people from exposure to gaseous tritium. So one of the major activities before starting the tritium experiment in Heidelberg was to take safety precautions and to get the laboratory approved by the local authorities.

To avoid a contamination of the laboratory and the people working there with tritium in any case, strong safety regulations were taken. In close collaboration with the radiation safety group of the Max-Planck-Institut für Kernphysik a safety concept was developed [DSL09]. The main idea of the concept is to have multiple layers of safety precautions, in

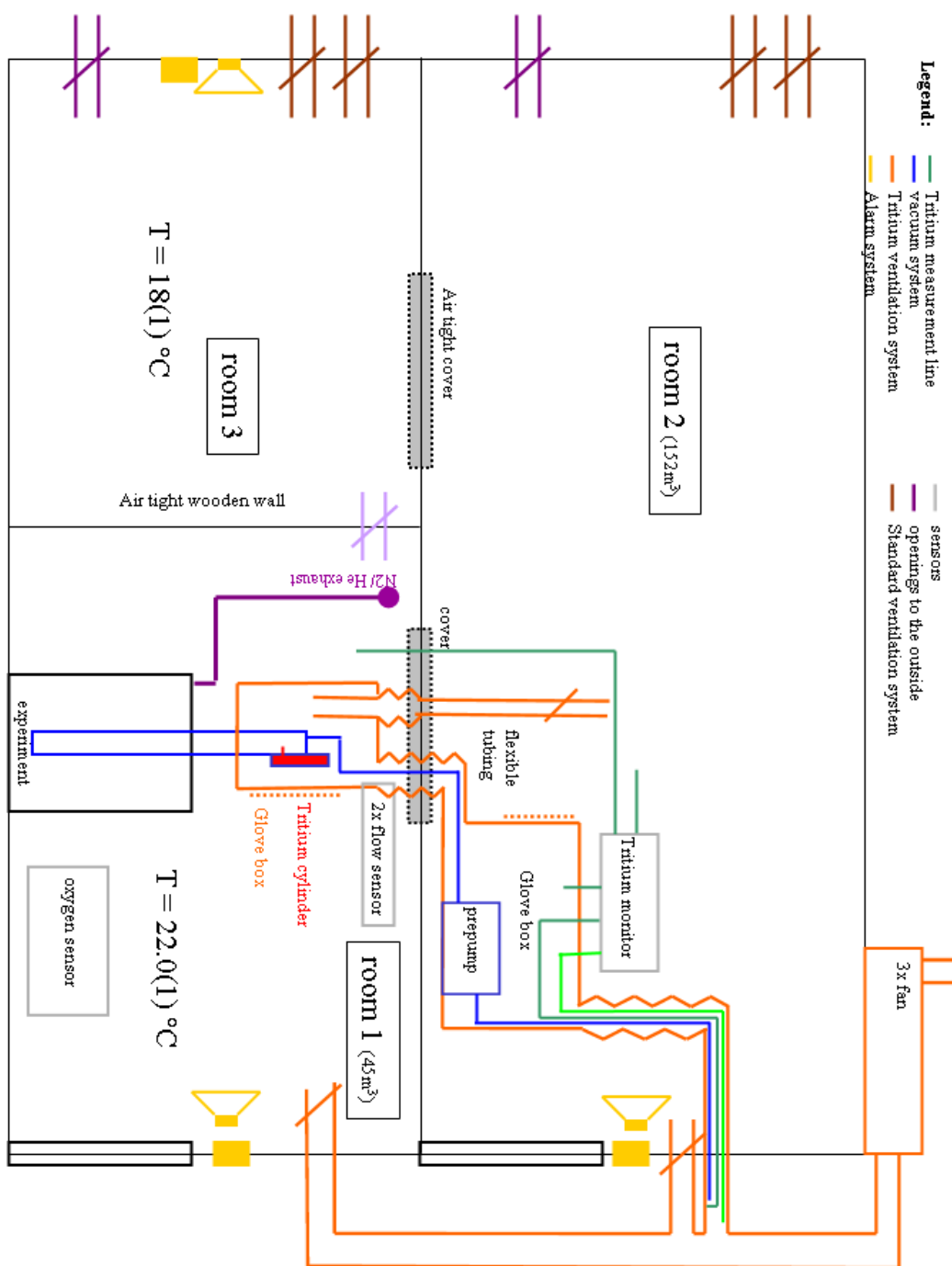


Figure 5.1: Schematic drawing of the safety system in the tritium laboratory. For more details see text.

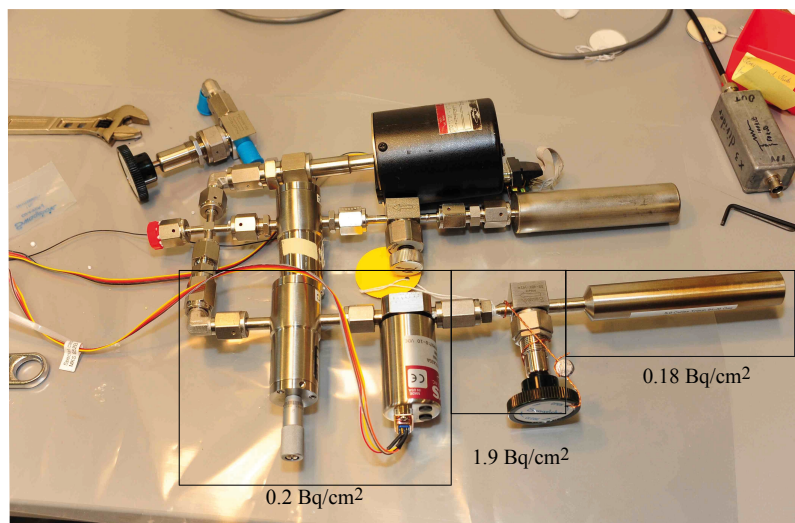


Figure 5.2: Photo of the tritium cylinder and the gas handling system. The boxes indicate the results of a wipe test, that was evaluated at the German Center for Cancer Research (DKFZ). The maximum allowed values according to German law (StrSchV) is 100 Bq/cm^2 . Courtesy of Ralf Lackner.

order to minimize the risk of tritium exposure to humans as much as possible. In Fig. 5.1 a schematic of the system is shown. The first safety layer is given by the experiment design, which contains the tritium completely inside the vacuum envelope (the blue lines in Fig. 5.1). The tritium cylinder attached to the gas handling system is shown in Fig. 5.2. So the only way the tritium can get out of the experiment, assuming there is no leak to the tritium cylinder, is through the exhaust of the vacuum prepump, which is released through a chimney on top of the building. This chimney is about three meters above the roof, so contamination of people working on top of the building is excluded. In a worst case scenario, when all tritium would be released through the chimney at once, it was estimated that the maximum dose an uninvolved person in one of the surrounding buildings could get is 0.1 mSv , which is below the accepted limit of 0.3 mSv/year .

The situation is different in the rather small and enclosed volume of the laboratory where the tritium would only spread to 45 m^3 in the case of the magnet room. Therefore, a second layer of safety (orange lines in Fig. 5.1) that also handles the problem of a leak of the tritium cylinder, is provided by a vented glove box system. A fan on top of the building vents this system with a flow rate of $100 \text{ m}^3/\text{h}$. To ensure permanent ventilation two additional redundant fans are installed to take over in case of a failure or maintenance of the first fan. The glove box system consists of two boxes, one put directly on top of the experiment (experiment box), while the other houses the prepump (pump box). The glove boxes are connected to the fan and to each other by flexible tubing with a diameter of 102 mm . Inside this tubing all electrical and vacuum connections to the ion source part of the experiment

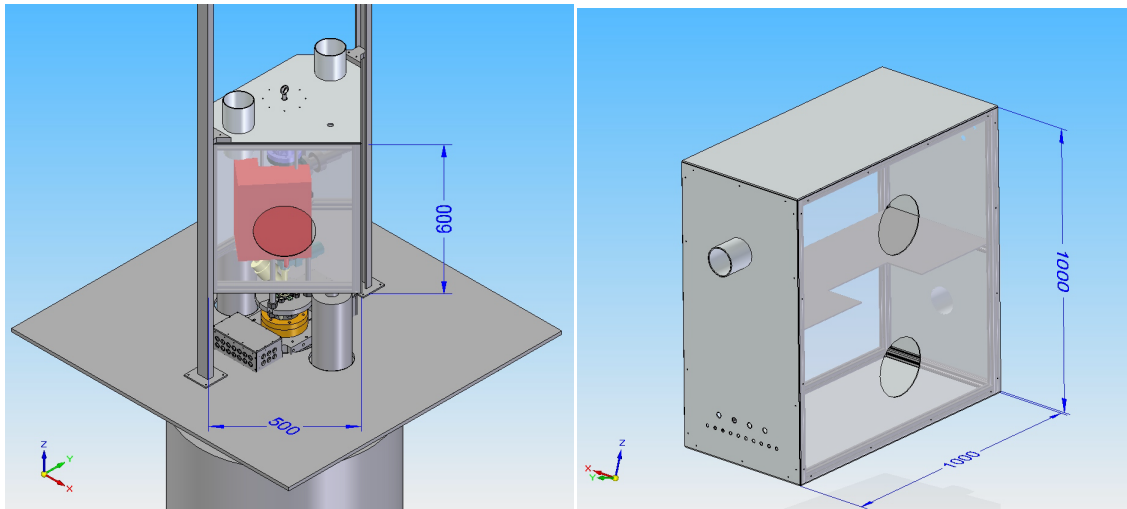


Figure 5.3: On the left hand side the glove box containing the gas handling system is shown. On the right hand side the glove box containing the prepump is shown. The lengths are given in mm.

are arranged. The design of the glove boxes was based on several boundary conditions, which are listed below:

- The glove boxes need to enclose the complete gas handling system and all parts downstream in the vacuum system.
- The experiment box needs to fit to the diameter of the hole in the ceiling and all connections to the box need to be flexible in order to allow lifting the experiment from room 1 to room 2 (see section 5.3).
- All relevant parts inside the glove boxes need to be reachable via the gloves.
- The glove boxes need to be stable enough, in particular the experiment box must provide an anchor point for the crane to lift the experiments.
- The experiment box needs to be close-fitting to the turbo pump in order not to waste available space for maintenance work on the amplifier system.
- The experiment box needs to be short enough not to interfere with the stacks of the magnet.

The designed glove boxes meeting these requirements are shown in Fig. 5.3.

Part of the second layer of safety are also two air flow sensors (from SLG), which are mounted inside the experiment glove box. They have a threshold that can be set from 1 to 10 m/s air flow velocity by a potentiometer. In case the flow velocity is smaller or the

sensors are out of order, a relay opens and a flow alarm is set off. In order to monitor the amount of tritium in the air of the glove box, a tritium monitor is installed. The monitor is a Canberra TAM100DSI with a sensitivity limit of 18 kBq/m^3 . It is based on an ionization chamber. A big advantage of the system is that it does not need any additional count gas, so that it can run with little maintenance (a pump and a filter need to be exchanged about twice a year). In case that a threshold of 90 kBq/m^3 is reached (this corresponds to a dose of 6 mSv for the experimenter, in case that he would breath the air of the glove box over 2000 h, which is a standard working time per year), an alarm is set off. This alarm also changes the settings of the ventilation system such that the air flow through the glove box is increased. Also the laboratories are decoupled from the standard ventilation system in order to prevent a possible contamination of tritium from diffusing into other parts of the building. For the very unlikely case that both layers of safety systems already described would fail, even a third layer is installed. The laboratory rooms were modified such that they are as air-tight as possible (about 1.5 air exchanges per hour were requested by the local authorities). To this end, special doors were installed and the windows were sealed. In addition, the rooms are kept at a slight under-pressure by the ventilation system. In a test carried out after these installations by DEKRA [Boe09], an air exchange rate of 1.72 times the volume of the room per hour for the upper laboratory (room 2) and 1.34 times the volume per hour for the lower laboratory (room 1) was measured. This meant an improvement by a factor of 3 compared to the original setting of the labs. In order to prevent air-tightness from being compromised by doors in a force-open state, an acoustic warning is sounded if a magnetic sensor detects a door to be open for more than 30 seconds. After an additional 70 seconds, the warning turns into an alarm. Not directly related to the tritium but part of the safety concept of the laboratory is the installation of oxygen sensors in room 1. These also give an alarm to the system in case the oxygen content in the air falls below 17%. The whole safety system as well as the ventilation control is coordinated by a Siemens DDC (direct digital control) system. This system automatically controls all components of the ventilation as well as the alarm system. In case one of the alarm conditions is met the system blows a signal horn and fires a flashlight in the laboratory. The system is also constructed redundant with two controllers that check that the other controller is still working. The whole system is part of the central building control system. In order to be safe from power failure, the vacuum system of the experiment, the tritium monitor and the air flow sensors are powered through a battery backup. For the ventilation system, a Diesel generator is available. Moreover, the ventilation flaps have a spring that brings them to a previously specified safe position in case of power failure.

5.2 Environment stabilization systems

Already with the Seattle experiment, it became clear that environmental effects, such as pressure and temperature changes, have an impact on the results of the high-precision measurements [VDFZS99]. These effects are attributed to changes in the mechanical ar-

Environmental parameter	Achieved stabilization
Room temperature	0.2 K/d at 24°C
Vibration velocity	1 $\mu\text{m/s}$ at 50 Hz
Liquid helium level of the traps	0.1 mm
Pressure inside the cryostat	0.1 Pa
Magnetic field drift	$< 1 \cdot 10^{-10}/\text{h}$

Table 5.1: Stabilization of environmental conditions in Heidelberg.

range of the spectrometer and most prominently to changes in the magnetic susceptibility of the materials surrounding the ions. Another disturbing factor are external magnetic fields, such as the earth's magnetic field. Therefore, a number of stabilization and shielding efforts were taken, both in Seattle and in Heidelberg (see section 5.2.1). A major improvement in Heidelberg stems from a computer-controlled data acquisition system. The system is based on a LabWindows/CVI program that reads out the 32 channels of an NI 6229 card. The NI card has a resolution of 16 bits in four different ranges: ± 0.2 , ± 1 , ± 5 and ± 10 V. In addition a box custom-made by the electronics workshop with 4 channels for resistance measurements (needed for the temperature sensors) is read out. Typically, one point per second is taken (up to 250000 points per second are possible), which should be sufficient as typical ion frequency measurements take on the order of minutes. All data are saved permanently, so that a later correlation with ion data is possible. Typical values of the stabilized quantities as achieved in Heidelberg are given in Tab. 5.1. A more detailed overview on the stabilization of environmental parameters can be found elsewhere [Str11].

5.2.1 Magnetic field stabilization

Most of the environmental stabilization concentrates on the stabilization of the magnetic field as it has direct influence on the mass measurements (see Eq. (3.72)). In a typical measurement, data are taken over several days and so it is important, that the magnetic field stays constant enough on these time scales. In addition it is also desirable to avoid short-term fluctuations between subsequent measurements. The major contribution to shifts and drifts in the magnetic field comes from the materials of the magnet and the trap. Here, the thermal insulator material of the magnet (G10) has the highest temperature dependence of the magnetic susceptibility [LFLM90]. Therefore, one approach for the stabilization of the magnetic field around the traps is to stabilize the temperature inside the magnet. This is achieved by stabilizing the level of the liquid helium and the pressure in the bore. Constant level and pressure result in a constant temperature distribution and hence in a constant magnetic susceptibility. The stabilization is based on controlling the flow of helium out of the bore and the liquid helium reservoir by electronically controlled valves. In order to control the liquid helium level a helical coil resonator is attached to the beam tube about 30 cm above the center of the magnetic field. The resonance frequency depends on

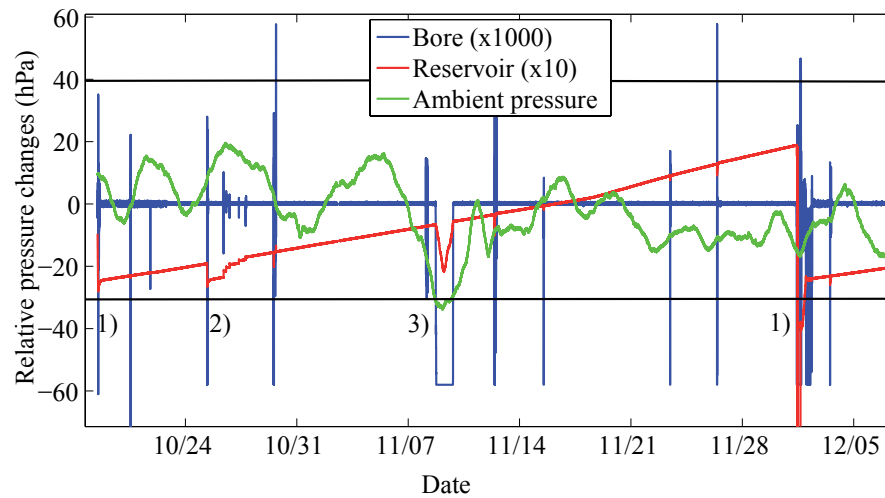


Figure 5.4: The change in ambient pressure, reservoir pressure and bore pressure between two fillings with liquid helium (indicated as 1)). In 2) tests with the stabilization system were carried out. In 3) an extremely low ambient pressure (below 980 hPa) caused a failure of the stabilization system. The black lines indicate the working range of the system. Courtesy of Sebastian Streubel.

the permittivity of the surrounding helium. Custom-made electronics measures the current resonance frequency and changes the pressure in the reservoir (that acts like a stamp) until a specified resonance frequency and hence a specified level is reached. The achieved level stability is about 0.1 mm.

The pressure inside the bore is controlled by an external pressure reference. An MKS Baratron 223 BD differential capacitance manometer compares this pressure to the pressure of a reference volume. Via another valve controlled by custom-made electronics this pressure difference is minimized and a pressure stability of 0.1 Pa is achieved. In order to avoid air from flowing into the magnet, the absolute pressure is set to 1050 hPa in order to always be significantly above the atmospheric pressure. However, the maximum pressure difference that can be obtained to the ambient pressure is 70 hPa, so in rare cases (about once per year) it can happen that the system fails. The performance of the pressure stabilization system is illustrated in Fig. 5.4.

In addition to the stabilization of the magnetic properties inside the superconducting magnet, shielding of external magnetic fields is applied. Part of it is a passive self-shielding superconducting coil [GT88] inside the solenoid that provides a shield factor of about 200. The other part is an active correction applied by a pair of Helmholtz coils. A custom-made fluxgate magnetometer measures changes in the magnetic field about 1.5 m apart from the superconducting magnet. The signal is then amplified and fed onto the Helmholtz coils. So far, this system has not been turned into operation in Heidelberg. All the stabilization efforts together resulted in a magnetic field drift as small as $1.7 \cdot 10^{-12}$ /h in Seattle, making

the magnet the most stable in the world. In Heidelberg so far a stability of about $10^{-10}/\text{h}$ has been achieved (see section 6.1.1).

5.2.2 Temperature stabilization

The room containing the superconducting magnet is temperature-stabilized as well. The stabilization is based on maintaining a temperature gradient between room 1 and room 3 (see Fig. 5.1) of about 4 K. A wooden wall is installed to allow a constant heat flow between the two rooms. In room 1 four rack heaters are installed in the corners in order to heat the room to 24 °C, while in room 3 cool water chillers are installed that keep the room at about 18 °C. A temperature sensor in room 1 gives feedback to a commercial control system based on the Siemens DDC technique, utilized for the alarm system as well. The system was customized by the engineering bureau IBV Mosberger. The typical stability is about 0.2 K; however, a stability of < 0.1 K was aimed for.

5.2.3 Vibration isolation

The vibration isolation is a passive system. The magnet is sitting on a glass-fiber reinforced concrete block that is decoupled from the foundation of the building. This way vibrations of the building, e.g. caused by pumps or transformers, should be significantly damped. Measurements by an engineering bureau [BB08] utilizing a vibration velocity sensor yielded that the most critical region concerning the vibrations is around 50 Hz. Here, maximum vibration velocities of about $1 \mu\text{m/s}$ were determined. It is assumed that this is much smaller than the vibrational amplitudes caused by the turbomolecular pump attached to the top of the experiment. Turning this turbo pump off for test purposes did not result in any measurable shift (on a 10^{-8} level at the time of the test) of the modified cyclotron frequency.

5.3 Adaption to the already existing spectrometer

As already mentioned, the MPIK/UW-PTMS was designed and assembled at the University of Washington. Therefore, the laboratory also had to be adapted to allow for the use of this particular instrument. A lot of difficulties arise here from different standards in the US and Germany. E.g. all screws of the experiment are non-metric and hence, it was necessary to get a supply of non-metric screws, but it was tried to switch to metric screws wherever possible. A major modification of the laboratory is introduced with the power supply of the experiment. While the standard European voltage is about 230 V, many parts of the experiment need 110 V. Therefore, a transformer with a maximum apparent power of 5000 VA was installed. As this transformer also causes a significant magnetic disturbance, it was installed as far from the experiment as possible in the corner of the neighboring experiment room.

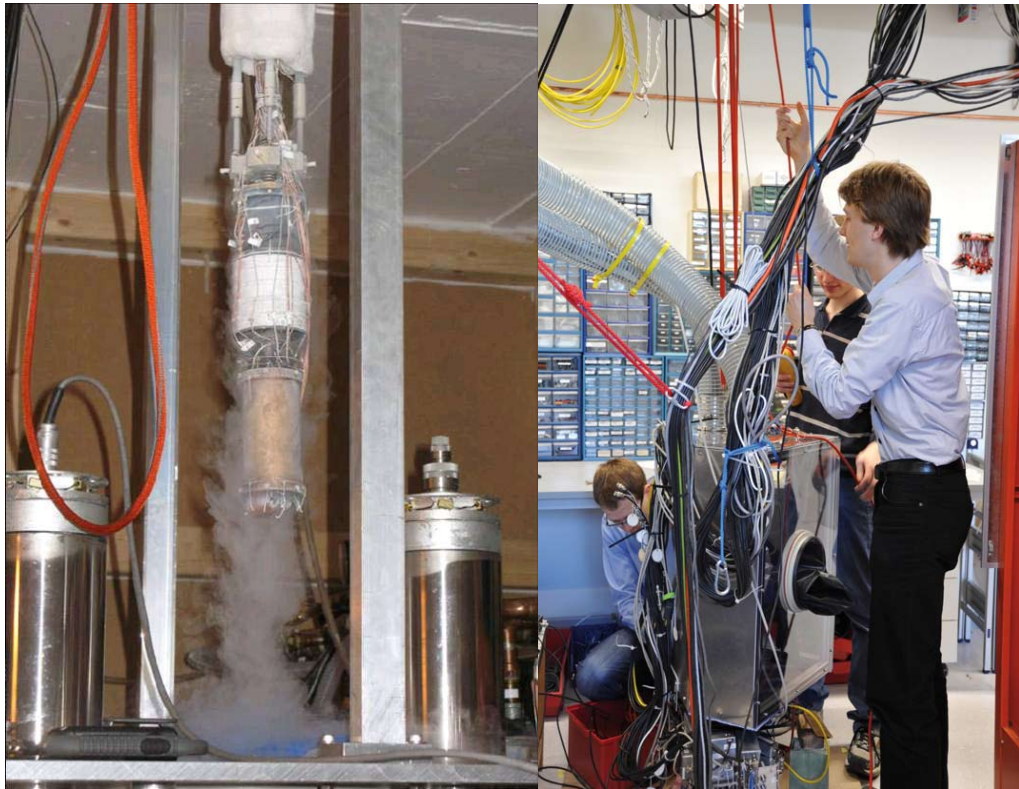


Figure 5.5: Moving the experiment between room 1 and 2. Typically, at least 3 person are needed for this job.

Another major difference between the Seattle and the Heidelberg lab is the height of the ceiling. While the Seattle experiment hall had a total height of more than 5 m, the rooms in Heidelberg are only 2.8 m high. This is not sufficient to lift the experiment out of the magnet. Therefore, a 80 cm diameter hole was drilled between the first and the second floor in order to lift the experiment out of the magnet. As the experiment weighs about 60 kg, a crane and a redundant pulley were installed for this purpose.

6 Experimental results

In this chapter, the results of commissioning experiments for the new spectrometer and the first test mass measurements will be reported. The new spectrometer was assembled in Seattle until the summer of 2007. Until then the first detection of several hundred ions was achieved. Thereafter, the experiment was stopped and shipped to Heidelberg in July 2008. Meanwhile, the old Seattle spectrometer was still running to take data until September 2008. The old spectrometer was shipped to Heidelberg in November 2008. The preparation of the laboratories in Heidelberg took until April 2009, when all tasks regarding the tritium safety precautions were completed. Since December 2008 the parts of the experiment (such as the racks and the magnet) were set up and tests of the electronics carried out. The magnet was switched on in February 2009. The first ion measurements with the spectrometer could be carried out in June 2009, but a number of experimental difficulties significantly slowed down the experimental progress. In August 2009, a cryo-leak in the trap chamber developed and the repair stopped the measurements until December 2009. From December 2009 until March 2010 the measurements suffered from anharmonic behaviour of the ion motion, believed to be caused by contamination of the trap surfaces. Since March 2010, the spectrometer has worked reliably, however for a couple of months recurrent problems with noise spikes occurred. It turned out that the noise was caused by switch-mode heaters that have worked reliably for many years in Seattle. Searching for the source of the noise the trap electrodes were connected in a “minimum” configuration to eliminate sources of noise pickup. In this configuration the loading via the field emission point and the basic trapping capabilities were available, while external ion loading and transfers between the traps could not be tested.

In the fall of 2010 the principle ability of the spectrometer to perform measurements with small clouds or even single ions could be demonstrated. It was possible to learn and improve the procedures necessary for precision mass measurements. The goal is to achieve data of a comparable or even better quality than the last Seattle data (see Fig. 6.1 for data taken just before the lab was taken down). So far, first tests of the current precision and accuracy for mass measurements were carried out. The measurements revealed the current limitations of the spectrometer (e.g. the precision voltage source stability) and are the basis for major maintenance work which started recently.

6.1 Commissioning experiments

Before experiments with ions could be carried out in Heidelberg, the spectrometer had to be prepared in several steps. The first step of this commissioning of the experiment included connecting the electronics and synthesizers with the experiment (the connection

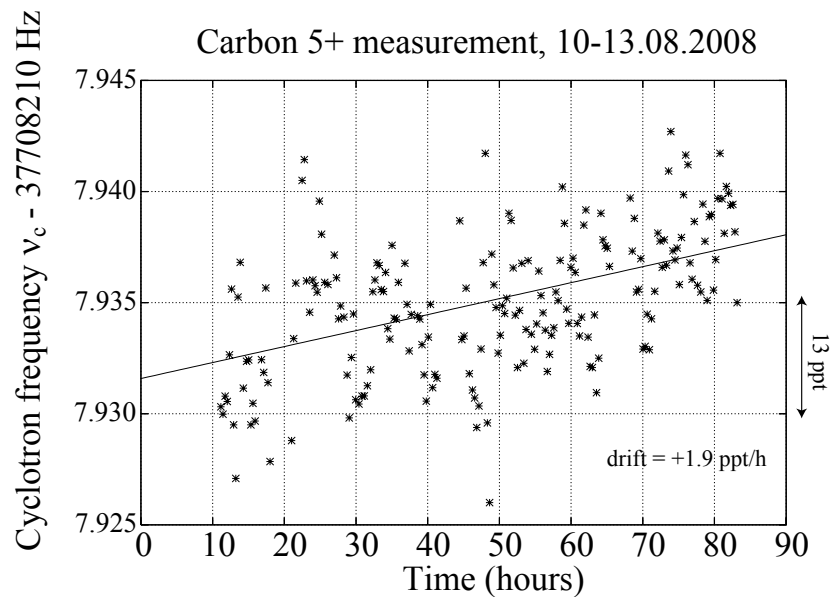


Figure 6.1: Cyclotron frequency measurements of $^{12}\text{C}^{5+}$ to determine the magnetic field drift of the superconducting magnet in Seattle, which is now in use in Heidelberg. The drift of the data is 1.9 ppt/h, attributed to the magnetic field drift. Typical single shot precision of these data is 1 part in 10^{10} . Courtesy of R. S. Van Dyck, Jr..

scheme mainly resembles the connections of Fig. 4.16). In particular in the electronics a lot of minor bugs (mainly broken connections due to the shipping) had to be fixed. After setting up the electronics properly, it is important to tune the center frequency of the tuned circuit and identify (and in the best case eliminate) noise sources. Another important step before working with ions is to compensate the coupling of the drive signals onto the amplifier as this mainly limits the drive amplitude at which the ions can be driven before saturating the amplifier system. Finally, also the alignment and the bake-out procedure for the traps as performed in the context of this thesis work are described in the following.

6.1.1 Tuned circuit and noise sources

Due to filters in the axial drive synthesis (with a width of about 100 kHz) and the -90 V maximum range of the voltage source, the axial frequency of the ions is supposed to be around 4 MHz by design. Therefore, it is necessary to tune the center frequency of the tuned circuit close to 4 MHz, as it was already described in section 4.2.1.

This procedure is additionally complicated by the occurrence of noise sources that make

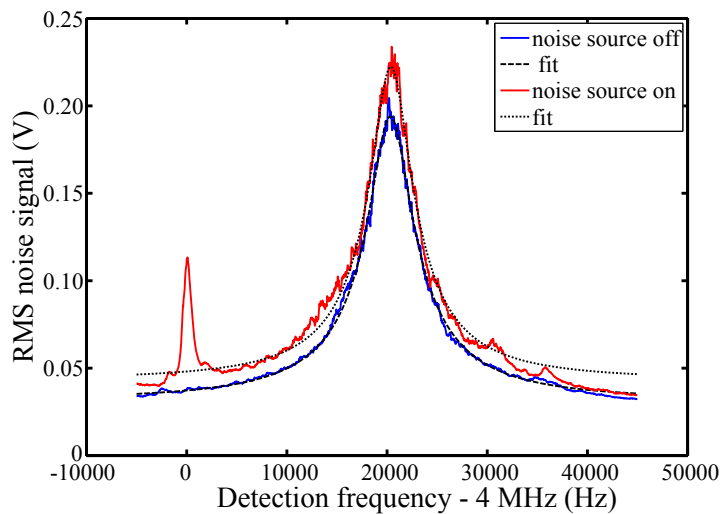


Figure 6.2: Tuned circuit with and without additional noise. The red line represents the tuned circuit, with the higher harmonics of the ADC clock on top, the blue line is without. The typical Q -value in the cryogenic region is around 1000 depending on the settings of the amplifier, compared to about 150 at room-temperature.

it necessary to move the center of the tuned circuit. In many cases, these can be identified as parts of the setup. Known noise sources so far are the CAEN power supply creating noise at 4 MHz, the Agilent function generators leaking out a signal even when their output is turned off, an ADC creating higher harmonics of its 100 kHz input and the switch-mode heaters, e.g. utilized for the liquid helium stacks of the magnet. Most noise sources identified so far have a rather sharp profile in frequency space and hence can be avoided by moving the detection frequency suitably. A typical tuned circuit with and without such a noise spike is illustrated in Fig. 6.2. Particularly detrimental for the experiment was the noise of the liquid helium stack heaters (see Fig. 6.3) as it is broad-band noise and shows oscillations with amplitudes comparable to ion amplitudes on varying time scales. Therefore, this noise made it impossible to observe ions. The exact mechanism how the noise of the heaters couples onto the tuned circuit is not yet clear, hence the heaters have been turned off, which can result in a decreased magnetic field stability. As a solution the utilization of linear controlled heaters is planned. During the search for the noise sources also the dc connection to the endcaps was disconnected in order to minimize noise pickup. This means that a biasing of the endcaps was not possible.

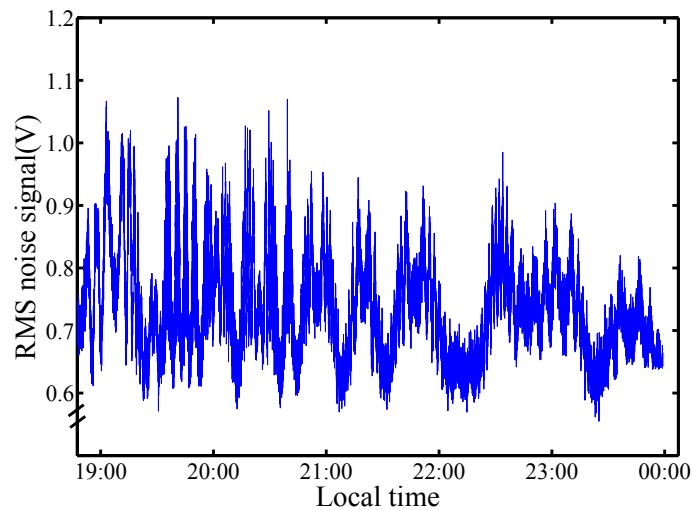


Figure 6.3: Noise induced by the liquid helium stack heaters at the center of the tuned circuit. Data taken on 31.08.2010.

6.1.2 Compensation of drive signals

The compensation of the coupling of drive signals (see section 4.2.2 for the different compensation schemes) onto the amplifier is important to allow as strong an axial drive as possible. While for the precision measurements as little drive as possible is desired due to drive-induced shifts of the axial frequency (see Eq. (3.55)), for the first detection of ions in a cloud of contamination it is helpful to be able to drive hard.

The figure of merit to be minimized for the drive compensation is the amount of pseudo-coherent signal generated by the drive in the detection system, measured via the error signal as defined in Eq. (3.38). Two approaches to adjust the coupling have already been described in section 4.2.2. The advantage of the utilization of coupling capacitors is the broad-band compensation. However, a major drawback is the inability to change the capacitors in-situ, when the trap is immersed into the liquid helium reservoir of the magnet. The achieved suppression with this method has been varying quite a lot between almost 0 dB and about 20 dB, as the capacitances changed rather randomly, when being immersed into liquid helium. Therefore, the second method, where part of the signal is phase-shifted, attenuated and fed back onto the amplifier, has been tested, even though the compensation usually only works over a small interval of several kHz, probably due to an additional frequency dependent phase shift, when coupling the compensation signal onto the amplifier. However, this is not a major limitation as the main source of disturbance for the amplifier is the axial drive signal, which is not changed by more than some kHz during the experiments. All other drive signals are much further away in frequency space and hence have less influence on the amplifier. For the optimization two parameters can be varied: The

length of the cable to the amplifier, which changes the phase by about $7^\circ/\text{m}$ (for 4 MHz), and the attenuation of the compensation signal. Typical values are cable lengths of about 12 m and attenuations of 20 dB. The achieved suppression of coupling with this method is about 20 dB and can be achieved quite reliably. Therefore, this method is favored over the original compensation concept developed in Seattle.

6.1.3 Alignment of the traps

A misalignment of the traps causes frequency shifts as explained in section 3.4.2. Therefore, properly aligning the traps is part of the preparation for precision mass measurements. The simplest method to align the traps with respect to the magnetic field is to run the FEP in a single pass mode (same settings as in Fig. 4.5 but with EtSkim at 0 V). This creates an electron beam of several nA, which can be detected by electrometers attached to several of the trap electrodes. The rods of the rotation stage are then turned until no more current on the trap electrodes is observed, corresponding to shooting all way through the trap. The sensitivity of this method can be estimated from the geometry of the traps to be better than 0.4° . A detailed description of this method is given in [Höc10]. One advantage of the method is that it does not rely on ions being loaded into the trap or the detection system and therefore is easy to apply. The main disadvantage of the method is that the surfaces of the trap can charge up due to the electron beam hitting them for hours. Therefore, after the alignment with this method it can be necessary to pull the traps out of the magnet, as the surface charges neutralize much faster at room temperature, and rely on the alignment being constant between two different lowerings.

A second method for the alignment is to make use of the dependence of the axial frequency on the tilt angle θ (see Eq. (3.61)). To this end, an ion or an ion cloud is brought into the axial frequency lock. Then the axial frequency is maximized as it should have a maximum for $\theta = 0$. The lock loop corrects for this frequency shift and a shift of the correction voltage is observed. The sensitivity of this method is very high. Even assuming the largest lock setting of 20 mV, a sensitivity to lock changes of about 1 mV is obtained. This corresponds to a sensitivity in θ well below 0.1° . However, in practice not the detection method, but rather the mechanical arrangement, will limit the sensitivity of this method. A realistic estimate here is that the mechanical tuning will not be much more accurate than 1/10 of a full turn of the alignment rods. This corresponds to an angle of 0.1° .

In practice the translation stage was not working properly during the last lowerings of the experiment due to backlash and friction in the translation stage. A first attempt to fix these problems failed as they only showed up at cryogenic temperatures. Eventually, one of the control rods could not be turned for the mass measurements described in section 6.4. So, the tilt angle of the experiment was fixed (see section 6.3.3 for a determination of the angle).

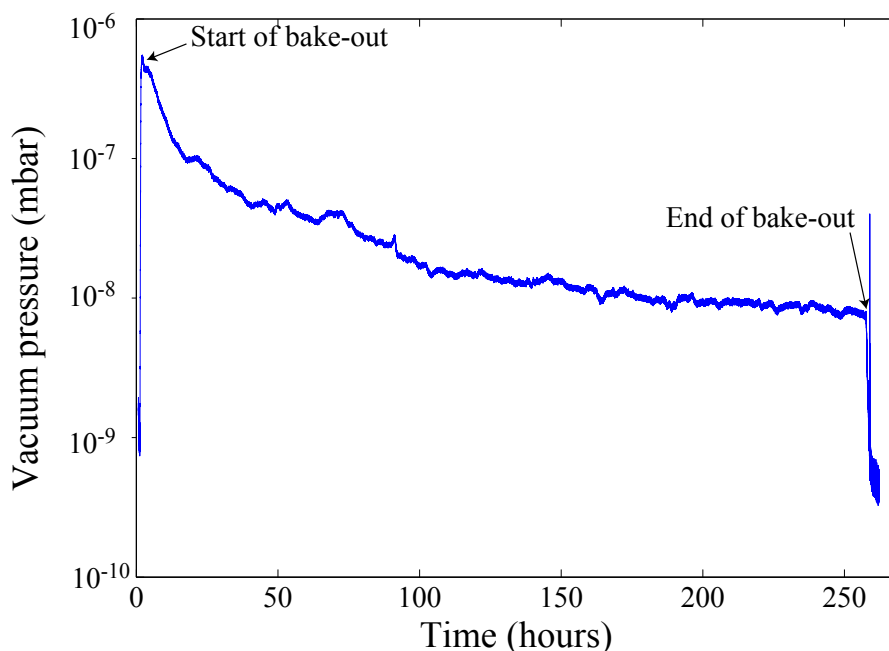


Figure 6.4: Pressure at the gauge close to the turbo pump during the bake-out of the traps after exposure to air.

6.1.4 Bake-out of the traps

As already mentioned in section 4.1.5, a cryo-leak in the feedthrough flange of the trap chamber occurred in Fall 2009. Therefore, the vacuum had to be broken and the traps were exposed to air for a period of more than two months. After the reassembly of the trap, it was pumped for about a week before being reinserted into the magnet. In the following months ion signals could be obtained but anharmonic behavior of the trap made precision measurements impossible. Particularly, the trap was not behaving reproducible at all. The solution was to bake out the trap for about ten days. Therefore, a small bake-out setup, consisting of two 100 Watt halogen light bulbs was installed, which allowed for a touch-free bake-out. The temperature for the bake-out was set to 80 °C in order not to damage any of the materials utilized in and around the trap chamber, in particular to stay clear off the melting point of the silver-solder utilized for the feedthroughs. During the bake-out, outgassing of the traps was observed by a degradation of the vacuum by more than three orders of magnitude (see Fig. 6.4). Another bake-out, when the traps had not been exposed to air before, only showed a change of one order of magnitude. After the bake-out the trap was behaving much more reliable. It is assumed, that contamination of the trap surfaces by water or oxides, which charged up during the loading of the trap, was causing the anharmonicity problems of the trap. A drawback of the bake-out was that one of the

electrodes (CbSkim) showed an internal short-circuit afterwards, which is not yet fixed. Therefore, in the future it is intended to only bake-out after breaking the vacuum.

6.2 Ion preparation

An important step towards performing mass measurements is the reliable preparation of single ions. Therefore, a large part of the work in this thesis was dedicated to learning and optimizing the necessary procedures. Although, most of the procedures have been described in earlier theses from Seattle [Far95, VL04] and part of them could be trained with the still running old spectrometer in Seattle, it still remained a big challenge to achieve single ions with the MPIK/UW-PTMS. Partly this is due to the fact that parts of the procedures are based on the intuition of the experimenter, which has to be trained over time, partly it was because of differences between the spectrometers (e.g. the drive scheme is different). In addition, some time was invested in implementing new and more efficient cleaning procedures to remove contaminant ions. Towards the end of the thesis work, it was tried to prepare the ions in a more standardized way, relying on simple heuristics (repeating the same steps in a semi-automated way) rather than on intuition. This worked very good and reliably and so in the future the single ion preparation might be almost fully automated as it is the case for other spectrometers as well [Red07].

6.2.1 Loading from the external ion source and the gas handling system

Loading the trap from the external ion source will be a cornerstone on the way to a $^3\text{H}/^3\text{He}$ mass-ratio measurement, as ^3H can only be loaded this way in this setup. Measurements with the external ion source have been complicated by poisoning of the dispenser cathode, a well-known effect for this kind of cathode [BJ57]. In Fig. 6.5 a typical measurement of the electron emission over time versus the vacuum pressure is shown. After turning the ion source on, the cathode is heated slowly in order to avoid damaging. It can be seen that during the heating up of the cathode the vacuum is quickly degrading. At the maximum electron emission of about 0.7 mA an equilibrium state for the vacuum is achieved. Then the electron current declines over time. Unfortunately, the steady phase is typically less than an hour, which does not allow reliable operation. Therefore, it is planned to investigate other cathode materials, such as pure tungsten wire [Tre11].

In order to test the external loading, ^4He was inserted into the gas handling system, when the ion source was running. Poisoning of the cathode due to degraded vacuum was a major problem of these tests, when the gas was let into the system. However, a current of several pA of ions could be detected for parts of a second by a pico-ammeter connected to the electrode EtSkim, when no transfer sequence was applied. Unfortunately, the poisoning killed the emission of electrons for about half an hour after every shot, making tests of the transfer sequences hard to carry out. However, it could be demonstrated that despite magnetic mirror effects a transport of particles is feasible from the ion source into the capture

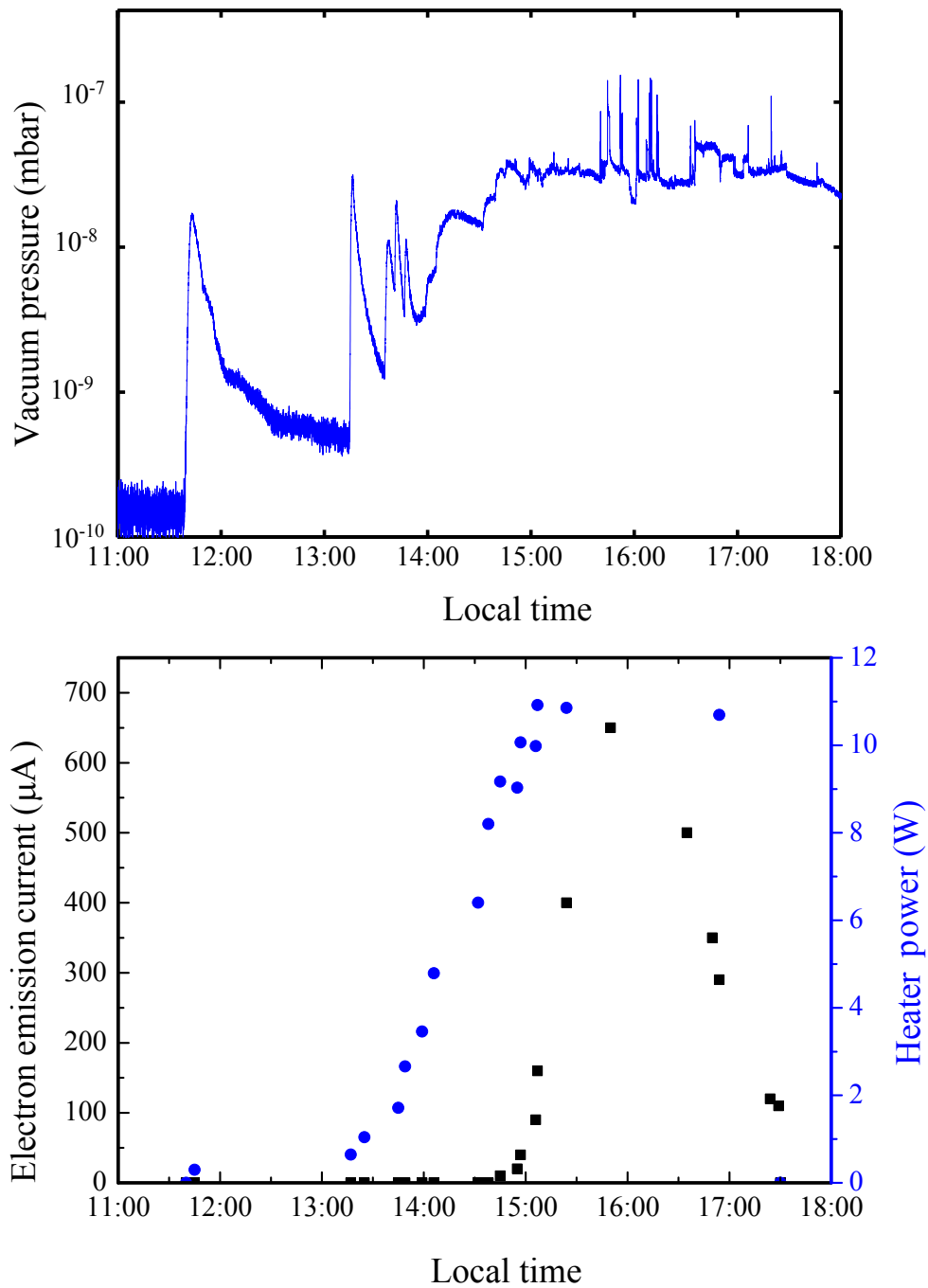


Figure 6.5: Upper figure: Vacuum pressure at the ion source gauge during the emission of electrons from the ion source. Lower figure: Electron emission current and heater power of the ion source.

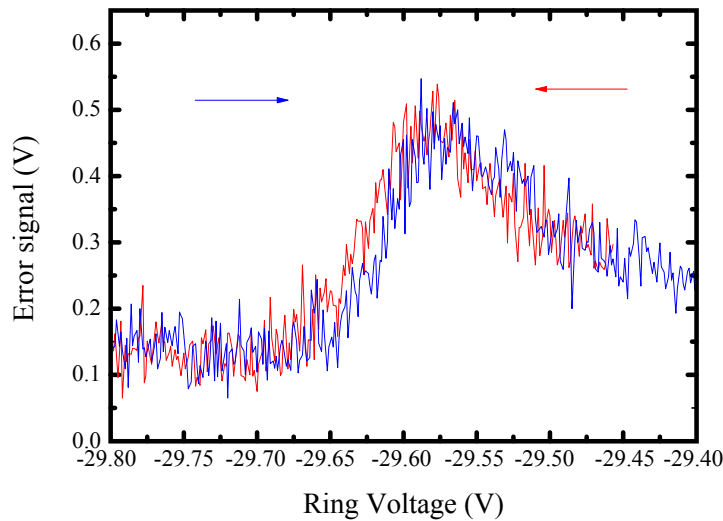


Figure 6.6: Coherent signal of protons in the capture trap. The protons were loaded inside the trap via electron impact ionization with electrons from the external ion source.

trap. It was concluded from these test measurements that both the cathode and the transfer sequence must be further investigated in a separate setup. Therefore, test measurements utilizing a tungsten cathode instead of the dispenser cathode and a micro-channel-plate detector or Faraday cup instead of a Penning trap for the detection are in progress [Tre11].

Another approach to load the traps was to use the electrons from the external ion source to ionize rest gas ions in the upper trap. Loading for about half an hour resulted in a measurable amount of protons in the capture trap (see Fig. 6.6). Unfortunately, this measurement was performed before the bake-out of the traps and so severe charging was present. So no further characterization of the capture trap could be performed. A later attempt failed as the alignment of the ion source with respect to the capture trap could not be changed due to the tilt- and translation stage not working properly.

A third approach for loading the traps uses the gas handling system in combination with the field emission point. For a test about 1 mbar ^4He was inserted in the vacuum system and ionized by the electrons from the field emission point. Afterwards, it was checked what ions were loaded in the experiment trap by performing mass scans. $^4\text{He}^{2+}$ ions were found, which are not loaded in large amounts in normal field emission point loading. It was concluded that this method could in principle be used for measurements of ^3He as well. However, a major limitation could arise by contamination of the trap surfaces due to the air that apparently also is inserted (what was concluded from loading ^{14}N , which otherwise is only seen in small amounts and for high electron currents). This could result in contamination of the trap surfaces with neutral gas and subsequent charge up the trap

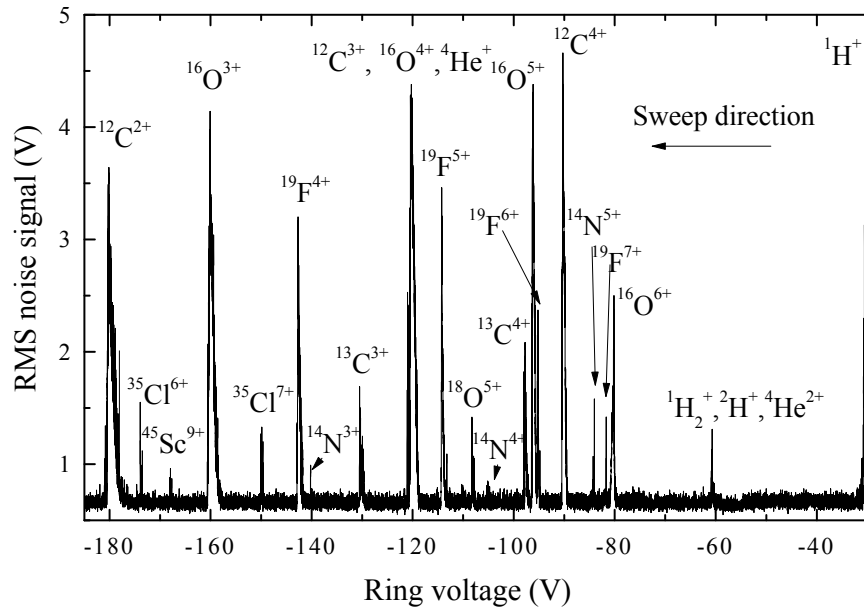


Figure 6.7: Mass spectrum from a loading procedure with the FEP. The assignment of the isotopes is based on calculations of the axial frequencies.

surfaces. In addition, this loading technique is not suitable for ^3H as it would entail massive radioactive contamination of the trap surfaces, which should be prevented by all means.

6.2.2 Loading from the field emission point

For loading the trap from the field emission point (see section 4.1.2) two voltages are relevant. First, the voltage difference between EbSkim and the field emission point defines the potential for the field emission and hence controls the available electron current. It has to be at least 300 V before measurable electron currents (of several nA) can be detected. Secondly, the difference between the field emission point voltage and the ring voltage defines the maximum energy of the electrons and hence allows to control the charge states that can be produced in the trap. Ionization can in principle take place everywhere on the flight path of the electrons (as long as the energy of the electrons is still high enough). However, a scenario where the ions are created close to the center of the trap seems to be most realistic as the likelihood for the ions to stay in the trap is the highest there. The neutral atoms can either come from the rest gas or from the surfaces of the trap electrodes that are hit by the electron beam. Unfortunately, this way of loading is neither mass- nor element-selective at all and large amounts of different contaminations can be produced. Depending on the ionization energy of the ion-of-interest, the difference of the field emission point voltage and the ring voltage could in principle be chosen just slightly above the ionization voltage, so that as little unnecessary contamination as possible is loaded. In practice

this approach does not work very reliably (often the ion-of-interest is not even loaded). Instead, energies at the maximum of the cross section at 3-4 times the ionization energy are chosen. The standard loading setting for the most commonly utilized $^{12}\text{C}^{4+}$ works with -200 V at the FEP, 120 V at the accelerator and -90 V at the ring (the ionization energy is 64.5 eV). A mass spectrum obtained with -500 V at the FEP and 20 V at EbSkim is shown in Fig. 6.7. The FEP voltage setting is the maximum achievable with the CAEN power supply in use and hence all ions that can be loaded without switching to a different power supply should be present. In order to observe the ions more efficiently a parametric drive (see section 3.3.4) was applied to the ions. The lower part of the spectrum (below -90 V), which is not available for the precision voltage source, is taken as a consistency check and to learn about the possible contaminations. The assignment of the peaks relies on the expected axial frequency for the ions, the ionization energies and likelihood estimations, e.g. it is very unlikely that exotic isotopes are created, when not even the most abundant isotope is seen in the trap. Quite surprisingly also somewhat unexpected ions of fluorine and chlorine are observed. This was already the case with the old UW-PTMS setup. A reasonable explanation is the use of a cleaning agent for the electrodes in Seattle that contained these two substances. One peak could only be assigned with $^{45}\text{Sc}^{9+}$, which seems unlikely, but not impossible. Some expected peaks have not been observed, namely the peak for $^{12}\text{C}^{5+}$. Possibly this is due to the ionization probability being significantly smaller as the electron energy was still too low [Cra81]. The loading procedure with the field emission point works quite reliably now, in particular with the new CAEN power supply, where the whole procedure is automated.

6.2.3 Application of different contaminant removal methods

Contamination of a sample of ions-of-interest with unwanted ions is a typical problem in mass spectrometry and also is one of the driving forces to develop mass spectrometric methods in the first place. In most cases the production mechanism of the ions causes this contamination as it is the case with loading from the field emission point. Many different techniques for contaminant removal have been tested in Penning traps [Moo89, E⁺08]. Most of them rely on excitation of the eigenmotions of the particle in order to increase its amplitude until it hits one of the electrodes. In this work several of these approaches for the axial motion were tested. Qualitative criteria for judging whether contaminants have been removed from the trap are the observability of the eigenfrequencies of the ions (as contaminant ions shift the eigenfrequencies and even can make the coherent detection of the axial frequency impossible directly after loading) and the results of direct searches for the contaminations by voltage scans in combination with a parametric drive (see section 3.3.4). A quantitative judgement is not possible as it is not clear whether the contaminants will always be detected in the voltage scans.

The simplest approach for contaminant removal is to apply an rf-signal (being called a broom), which is swept continuously over the axial frequency interval where ions are expected (determined by the limiting $q/m \approx 0.015$ e/u of the trap, see Eq. (3.16), and

$q/m = 1$ e/u for protons). The output amplitude of the synthesizer is typically between 1 to 10 V. In order to be more effective, the synthesizer output is modulated with white noise. As drive-dependent shifts in the axial frequency are expected (see section 3.4.1), the ions must be propelled through the anharmonic regions of the trap. A notch filter with an attenuation of about 40 dB at 4 MHz is installed in order to prevent the ion-of-interest from being lost. In addition, the tuned circuit should damp the motion of the ion-of-interest. However, interaction with hot contaminant ions still can remove ions-of-interest from the trap. Originally, also the former Seattle approach of splitting the rf-drive signal into two different frequency regions and leaving out a region of several hundred kHz around the axial frequency of the ion-of-interest was performed. However, no negative experiences were made with sweeping the broom over the axial frequency of the ion-of-interest and some contaminations were not hit by the wide-band brooms at all, so the standard approach is to have only one broom frequency region including all possible contaminant ions (from 800 kHz to 7 MHz). The performance of the unspecific wide-range broom alone is not too great. Typically, some but not all contamination is removed (mainly low charge state ions) and application of the broom over several minutes or even hours was necessary.

A more contaminant-specific alternative to the wide-range broom is an rf-signal that is swept over a narrow range (typically 20 kHz) around the expected axial frequencies of the contaminants (being called specific broom). This way, the power is used more efficiently. However precise knowledge of the axial frequencies and the contaminants in the traps is necessary. Typical contaminant ions are the ions found in the mass scans, but it cannot be excluded that other ions are loaded as well, so there always is the risk of missing a specific contaminant. So, typically the specific brooms are used in combination with the wide-range broom. The efficiency of the specific brooms was judged to be good by the parametric mass scans. A contaminant detected before brooming does not survive a specific broom (or at least cannot be detected any longer).

An alternative to the brooms that also applies the axial excitation of the ions is the SWIFT (Stored Waveform Inverse Fourier Transform) technique [GM96]. Here, a desired shape of the signal in the frequency domain is defined and translated into the time-domain by an inverse Fourier transformation. This time-domain signal is created by a programmable function generator. The shape in the frequency domain can be more or less arbitrary (limited by the specifications of the function generator in the time-domain), in order to replace the wide-range broom, a flat distribution over the expected range of frequencies was chosen. Only a small interval of 50 kHz around the axial frequency of the ion-of-interest was left out.

The big advantage of the SWIFT technique is that it produces much sharper profiles in frequency space than the sweep techniques described above. Hence, the risk to lose the ion-of-interest is minimized. In addition, the cleaning procedure should be sped up, as all ions can be excited at the same time. Unfortunately, the available frequency synthesizer was not able to deliver enough power in order to throw the ions completely out of the trap and so contaminant ions were still detected by the parametric excitation after applying SWIFT pulses.

The so far most efficient technique for contaminant removal is the combination of the brooms with a lowering of the ring potential (being called well-drop) to 20 to 50 mV. The broom already removes some of the contaminant ions or at least heats up their axial motion. Lowering the ring potential, and hence the trap depth, kills the remaining contaminant ions quite efficiently. In addition, also the number of ions-of-interest is reduced (see next section).

With the techniques described in this section, it is assumed that all contaminations can be removed from the trap (often by repeatedly applying the techniques). However, a definite proof is hard to give. Remaining contamination should make the trap behave somewhat randomly (changes in the eigenfrequencies depending on the position of the contaminant relative to the ion-of-interest should occur). So, mainly a lot of experience with the normal behavior of the trap is necessary in order to judge, whether contamination is still present or not.

6.2.4 Preparation of small ion clouds

Creating a single ion-of-interest is of utmost importance in order to achieve the smallest possible uncertainties in Penning trap mass spectrometry. More than one ion will create shifts in the eigenfrequencies and hence limit the accuracy of the measurements. Therefore, techniques to get rid of all but one ion are necessary. A typical single-ion preparation sequence (see Fig. 6.8) includes the following steps (assuming that all relevant parameters, such as the eigenfrequencies, have already been determined in earlier measurements):

1. Load the ions.
2. Find the ions-of-interest and try to center them on the tuned circuit in order to achieve efficient resistive cooling.
3. Apply wide-band and specific brooms, then perform a well-drop to about 50 mV.
4. Find the ions again (typically several mV shift occur after the first drop) and center them on the tuned circuit again.
5. Apply about one minute of magnetron cooling and one minute of modified cyclotron cooling.
6. Tune the guards in order to achieve a harmonic potential.
7. Take axial resonances and determine the approximate ion number from the signal width.
8. Apply brooms again, then drop to about 25 mV.
9. Repeat the steps 3.-7. with decreasing voltage on the ring. Typically ions are lost completely between 15 and 20 mV.

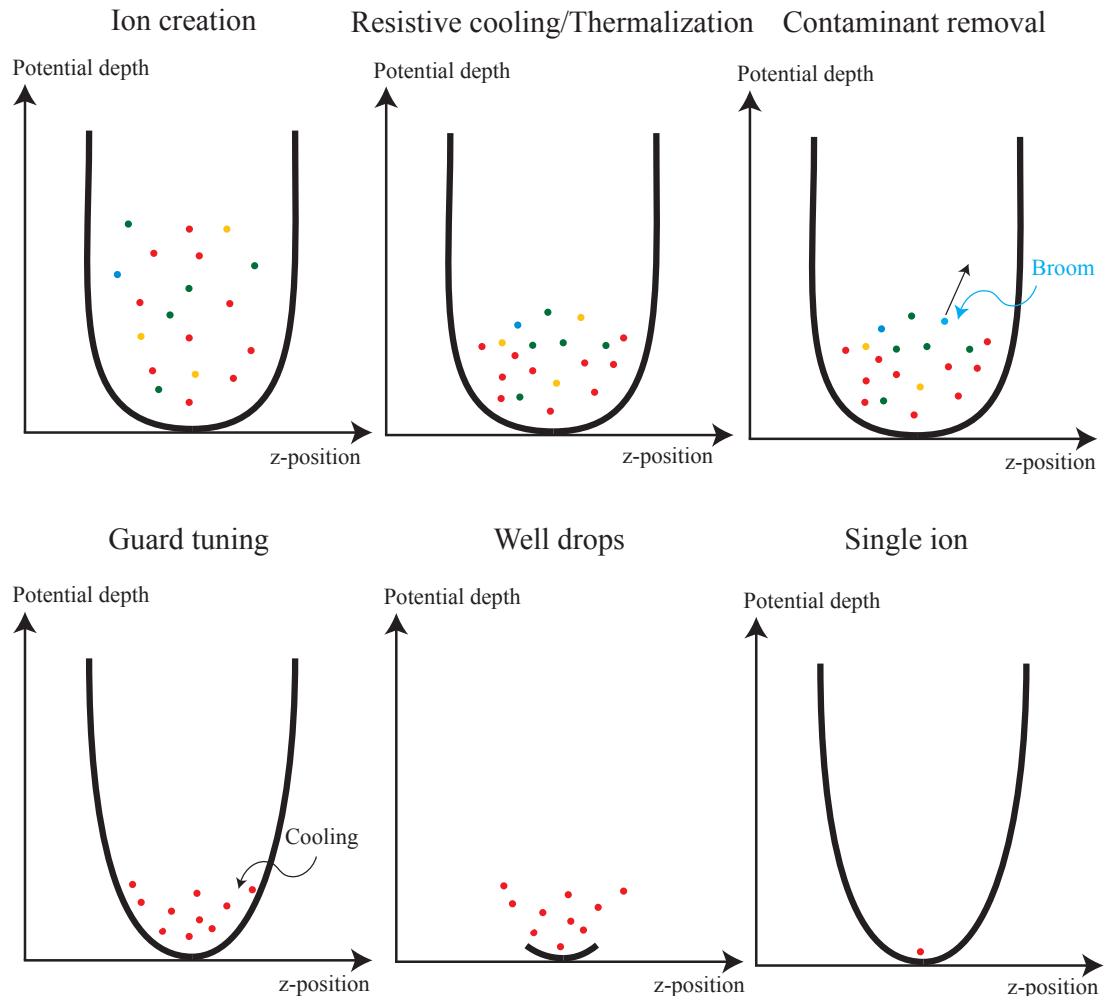


Figure 6.8: Pictogram of the steps necessary for single ion preparation. Red dots symbolize ions-of-interest, other dots are contaminant ions.

The above steps often are varied based on the experimenters' intuition, but they are the essentials of every preparation of small ion clouds. The whole procedure typically takes about an hour now, compared to several days in the beginning of the measurements in Heidelberg. The Seattle procedure also took several hours.

6.3 Measurement of the eigenfrequencies and optimization of trap parameters

Before performing mass measurements it is necessary to sufficiently characterize and tune the parameters of the trap with ions. This includes determining the ring voltage stability, the magnetic field and the optimum settings of the guards. All characterization measurements necessitate the measurement of at least one of the eigenfrequencies. Therefore, details on the measurements of all three will be discussed here. Almost all measurements described in this section have been carried out with $^{12}\text{C}^{4+}$ ions as they have an almost identical charge to mass ratio as $^3\text{H}^+$ and $^3\text{He}^+$, and hence, is a good test candidate. The main difference to measurements with $^3\text{H}^+$ and $^3\text{He}^+$ comes with the line-width, which is a factor of 4 larger due to the higher charge of $^{12}\text{C}^{4+}$. Also, $^{12}\text{C}^{4+}$ as a reference allows for absolute mass measurements (see section 6.4), as the mass of the carbon atom defines the atomic mass unit (see Eq. (2.24)).

6.3.1 Axial frequency measurements

Two different kinds of measurements of the axial motion are possible: First, the ring voltage can be kept fixed and the detection frequency is swept in order to find the axial resonance. Secondly, the detection frequency can be kept fixed, while the ring voltage is swept. The latter is particularly important in the case of the axial frequency lock, where the ring voltage is changed automatically in order to keep the axial frequency at the detection frequency (see section 4.2.4). Voltage sweeps and frequency sweeps are mainly equivalent and from differentiating Eq. (3.11) the relation

$$\frac{dv_z}{dV_0} = \frac{v_z}{2V_0} \quad (6.1)$$

can be obtained. Here, v_z is kept constant and V_0 is only changed over a small interval for a particular ion, so that dv_z/dV_0 can be handled like a constant property of the trap for a given ion. For values of several ions see Tab. 6.1.

As discussed in section 6.2.4, a typical measurement starts with finding the ions after loading. This is achieved by scanning the ring voltage over an interval several hundred mV around the expected ring voltage and looking at the RMS of the error signal (without any drive as the ions are still hot after loading) in order to see the influence of the

Ion of interest	$^{12}\text{C}^{4+}$	$^1\text{H}^+$	$^{16}\text{O}^{6+}$	$^3\text{H}^+/^3\text{He}^+$
$\frac{dv_z}{dV_0}$ at 4 MHz (Hz/mV)	22.3	66.6	25.0	22.3
$\gamma_{z,1}/(Q \cdot 2\pi)$ (mHz)	0.199	0.148	0.336	0.050

Table 6.1: Helpful quantities for axial frequency measurements. The linewidth of a single ion $\gamma_{z,1}$ is divided by 2π to convert from ω - to ν -space.

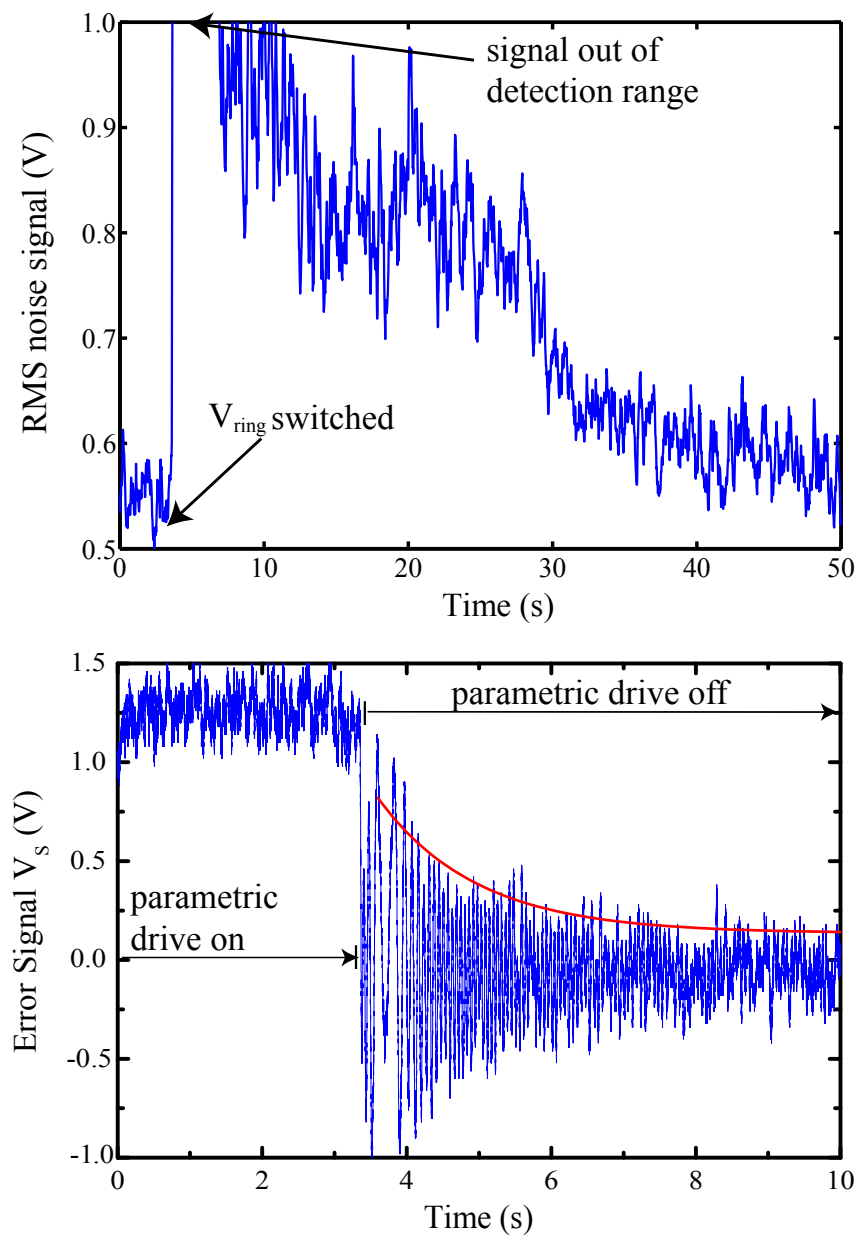


Figure 6.9: The upper figure was taken directly after loading the trap. When the voltage was switched to the correct ring voltage the ions equilibrate with the tuned circuit (and change their resonance frequency as well). This results in a decay of the signal. The lower figure was taken after some preparation of the ions. In the left part of the figure the ions were driven parametrically, then the drive is turned off and the signal is decaying exponentially with a time-constant of $1.4(1)$ s. The red line is an exponential fit to the data.

ions on the noise (see section 3.3.4). Depending on the number of ions and the amount of contamination in the trap, it can also be necessary to additionally apply a parametric drive in order to see the ions at all. When the ions are in resonance with the tuned circuit, resistive cooling will bring their axial motion into thermal equilibrium (see upper part of Fig. 6.9). The time constant of this damping in principle is linked to the ion number via γ_z (see Eq. (3.23) and Eq. (3.42)). However, directly after loading several effects, such as contamination ions, incoherent behavior and massive changes in the axial frequency during the cooling, disturb this measurement. A more precise determination of the cooling time constant can be achieved by parametrically heating the ions and observing the decay after turning the parametric drive off. This is demonstrated on the lower part of Fig. 6.9. Once the parametric drive is turned off the axial amplitude starts decaying exponentially (like a damped oscillator). On top, there is a beating, attributed to the difference between the axial frequency of the ions and the detection frequency.

After the first preparation steps, it is also possible to detect the ions coherently by sweeping the detection frequency and the axial drive. This results in the typical dispersion shapes (see Eq. (3.41) and upper part of Fig. 6.10), when the phase is set correctly. However, in some cases the signals do not look as nice, but have oscillations on top (see lower part of Fig. 6.10), differ by several Hz depending on the sweep direction and have different phases. A qualitative explanation of this process is the following: The oscillations again are explained by a damped decay. During the sweep of the drive, the ions' oscillation frequency changes from the driven frequency to a different frequency and is no longer driven. This could be explained by anharmonic frequency shifts, interaction with contaminant ions or short-term fluctuations in the ring voltage. However, the exact reason is still under investigation. When the ion is no longer driven, its motional amplitude at this frequency decays due to resistive cooling. The beat node with a changing frequency reflects the axial drive being swept further away from the eigenfrequency of the ions.

Even more delicate is finding a sound explanation for the frequency difference between the up- and downsweeps, which is not a random effect but always has the same sign. Effects of the detection system or the synthesizers have widely been checked and could be excluded. Recent studies did show a correlation with the voltage source stability. However, the exact mechanism, how random changes in the ring voltage could induce this effect is still unclear and further investigations will be necessary.

While the effects described above are undesirable and certainly need further investigation, they do not directly interfere with the ability of the experiment to perform mass measurements. For these measurements the drive frequency is not swept, but kept constant and the axial frequency locked loop is utilized. Therefore, the mean axial frequency is exactly the detection frequency (which not necessarily needs to be the natural axial frequency due to the numerous shifts discussed in section 3.4). The observable in this kind of axial frequency measurement therefore is the correction voltage V_{corr} applied to the ring (see Eq. 4.2).

In the following, several characterization measurements for the trap and the ions based on axial frequency measurements will be discussed.

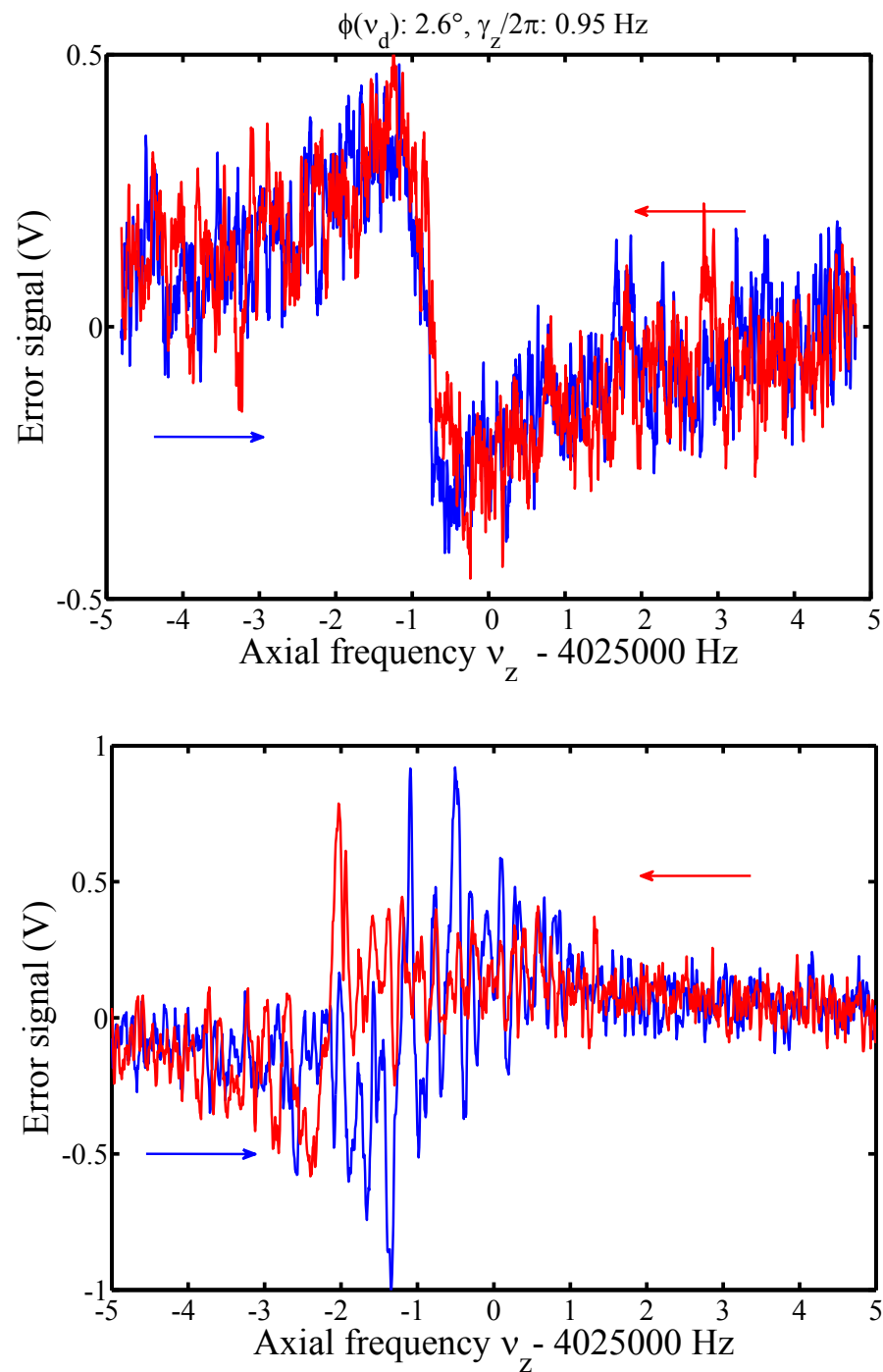


Figure 6.10: The upper figure shows a nice example of an axial frequency sweep. The lower figure is an example for problems observed frequently in the axial sweeps: beating and an offset between the two sweep directions.

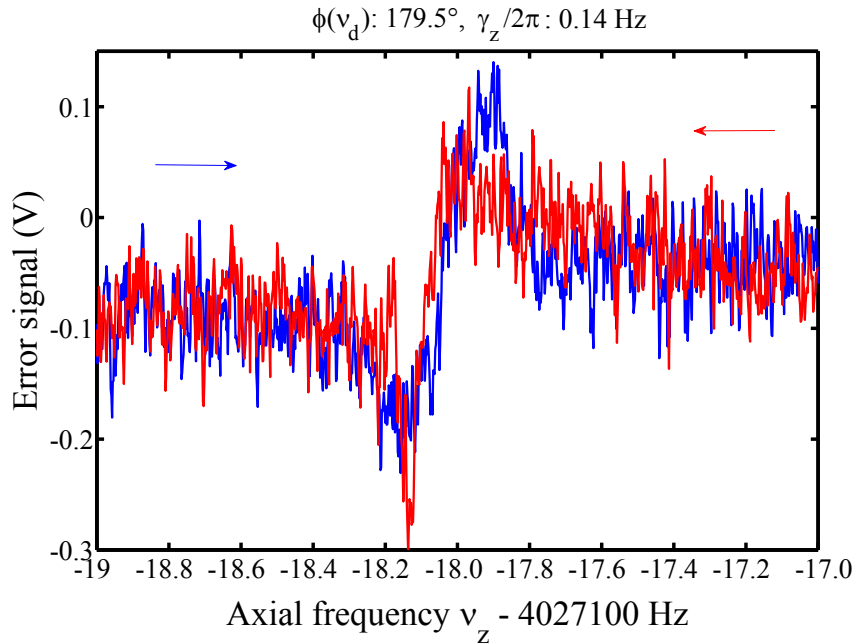


Figure 6.11: Narrow axial resonances. The line-width of 140 (50) mHz suggests the resonance is from a single ion only.

Ion number

The basis for all attempts to determine the ion number is Eq. (3.42). Typical values for the single ion line-widths are given in Tab. 6.1. For any given ion (and a given trap) the line-width is only a function of the number of ions N and the Q -value of the tuned circuit. As the ion number is a discrete quantity, discrete steps in the line-width should be observed. Two approaches to determine $\gamma_z/(2\pi)$ (the 2π are for the change from ω to ν) have been tested. The most straight-forward approach is to take axial resonances as shown in Fig. 6.10 and Fig. 6.11 and to evaluate the width of the resonance, which directly gives $\gamma_z/(2\pi)$ (see Fig. 3.8). For a good calibration the line-widths of several ion numbers should be determined to see discrete steps. In the old Seattle spectrometer, which has identical trap dimensions, but different trap capacity, the step size per ion (for $^{12}\text{C}^{4+}$) was 0.181 mHz $\cdot Q$ and showed a good agreement with the theoretical expectations [VD10]. For the MPIK/UW-PTMS the theoretical estimation is 0.199 mHz $\cdot Q$. So far, it was not possible to perform a measurement of discrete steps for several reasons. First of all, the experimental approach to clean the trap from contaminations always seem to result either in clouds of tens of ions, where it is really hard to tell the exact ion number within the accuracy of the fit, or in samples of 1-2 ions with a line-width below 500 mHz (for a Q of typically about 1000). In addition, in many cases the beating on top of the axial signal makes it hard to tell the exact width and up- and downsweeps deviate in width. Also, the

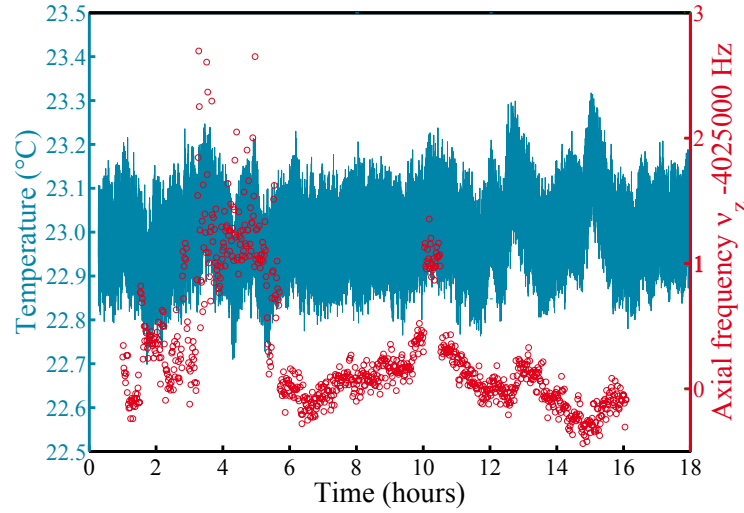


Figure 6.12: Centers of axial resonances and temperature close to the voltage source taken over one night (measurement started at 6 pm).

determined width is a function of the sweep rate as well, as there are some delays, e.g. due to the low pass filters of the detection system. Therefore, slow sweeps (sweep rates below 50 mHz/s) are desirable. However, for such slow sweeps fluctuations of the voltage source distort the measurement. Assuming the old calibration from Seattle to be still valid, we typically work with either 1 or 2 ions as the observed line widths range from about 150 mHz to 500 mHz with uncertainties in the determination of about 50 mHz. A resonance, as narrow as is expected for a single ion is shown in Fig. 6.11 with a line-width of 140(50) mHz (for a Q -value of 1000).

Ring voltage stability and lock loop performance

The stability of the ring voltage has several effects on the obtainable precision with this experiment, especially on the axial frequency (see Eq. (3.11)). Here, a fluctuation ΔV_{ring} of V_{ring} directly translates into a fluctuation of v_z . However, measuring ΔV_{ring} directly is not possible in the axial frequency lock. Here, V_{ring} is given as $V_{\text{ring}} = V_0 + V_{\text{corr}}$. What complicates the determination is that V_{corr} is a function of V_0 . As a change in V_0 changes the axial frequency, this also results in a change in V_{corr} . Assuming the locked loop works perfectly and infinitely fast this would result in $\Delta V_{\text{ring}} = 0$. In reality the lock will damp the fluctuations in V_0 , but due to its finite reaction time some fluctuation will remain. In order to quantify the fluctuations further investigations of the locked loop are planned. Another effect of the ring voltage stability is that it determines the minimum lock range that can be used. The smaller the lock range is, the smaller the drives for the radial detection can be. While the radial drive strengths do not change the radial frequencies (at least not on a 10 ppt

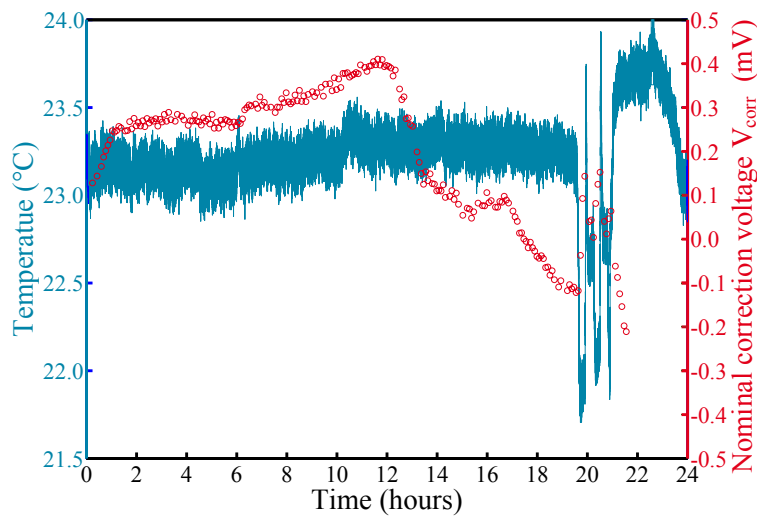


Figure 6.13: Change of the lock voltage (nominal full scale lock range: 2 mV, measured full scale range: 1.7 mV) and the temperature close to the voltage source during a long-term magnetron frequency measurement (measurement started at 6 pm). The large temperature changes at the end are due to liquid nitrogen filling of the magnet.

level), they change the distance between the corner frequencies in up- and downsweeps (see section 6.3.2), which increases the risk of systematic errors in the detection of their center.

Several approaches to determine the ring voltage stability are available. The stability of the precision voltage V_0 (without lock) can be measured directly by monitoring it with a precision multimeter (Keithley2002). An overnight measurement yielded a standard deviation of 1000 ppb for this method. However, this is only an upper limit as the thermal fluctuations of the multimeter reading should be on the same order. So, to further utilize this method, additional temperature stabilization of the multimeter would be necessary.

An alternative approach relying on the ions as a probe is to take axial resonances with identical settings over longer time intervals and plot the evolution of their center frequencies. This also gives an upper limit for the fluctuations of the precision voltage V_0 (as other unknown drift sources could be present as well). A measurement cycle over one night with this technique (see Fig. 6.12) shows a lot of fluctuations. While there are some rather quiet periods of several hours (from 6 to 10 in the figure) with a relative standard deviation of only 40 ppb (after removing a linear drift of 81 ppb/h), the overall range spanned during the whole night is 1590 ppb.

A measurement of the stability of V_{corr} is obtained from monitoring at which voltage the resonances start during modified cyclotron or magnetron data runs. Fig. 6.13 shows

the data of one overnight run, but other runs show similar behavior. The strong fluctuations at the end of the data-taking period are caused by a LN₂ filling of the magnet and the corresponding temperature change. During the night a rather slow drift of 10 $\mu\text{V}/\text{h}$ (110 ppb/h) is observed. Subtracting this drift a standard deviation of the data of 15 μV (160 ppb) remains. But even this is an order of magnitude larger than the voltage stability of the previously used Weston cells.

Concerning the fluctuations of V_{ring} an upper limit can be derived from the fluctuations of the modified cyclotron and the magnetron frequencies via Eq. (3.15). A typical standard deviation of a single data point was $\Delta\nu_{+} \approx 50$ mHz for $^{12}\text{C}^{4+}$. This corresponds to an upper limit for the relative fluctuation of V_{ring} of 162 ppb. The smallest measured standard deviation for the modified cyclotron frequency was $\Delta\nu_{+} = 10$ mHz. This corresponds to 32 ppb. For the magnetron frequency the smallest standard deviation was 40 mHz, resulting in an upper limit for the relative fluctuation of V_{ring} of 126 ppb.

The combined results for the ring voltage stability show that it is a limiting factor for the experiment right now. First of all, the fluctuations and in particular the drift are so big, that the lock loop can only be utilized nicely in the 2 mV full range setting. This results in the need for driving the radial eigenmotions harder in order to observe changes in their energy. Secondly, the fluctuations in the ring voltage potentially also affect the uncertainty in the frequency of the eigenmotions. Part of the explanation for the performance of the voltage source certainly is the broken temperature stabilization of the precision voltage source. This was concluded from the correlation with temperature changes in the room, where the voltage source is placed. Also the discrepancy between the measurements in Seattle (not performed with ions though), yielding fluctuations below 1 part in 10^8 , and the latest results in Heidelberg has to be clarified before aiming for ultra-high precision measurements. In order not to contribute to the uncertainty of the measurement on a 10^{-11} level the voltage stability in lock ΔV_{ring} needs to be on a 10^{-9} level. For making effective use of the smallest possible lock range with a full scale of 66 μV a stability of V_0 of some parts in 10^8 is needed. So, basically an improvement by one order of magnitude is needed for both quantities.

Optimization and determination of electrostatic trap parameters

An important step in the preparation of the ions is to tune out drive-dependent shifts and hence, the anharmonicity of the trap. Here, the leading order contribution is the C_4 term. The tuning works via finding the optimum guard compensation voltage V_c (see Eq. (3.58)). The optimization typically is a two-step process. Normally, the guards are not perfectly tuned directly after loading, even if the previous value of V_c is utilized. This can be attributed to two effects: First of all, after loading, the ion cloud and the contaminations distort the potential and secondly, unavoidable charging of the electrodes changes the potential for every load of ions. The result are anharmonic resonances. Therefore, in a first step the guard voltage is changed and the shape and the width (anharmonic resonances have different widths in up- and downsweeps) of the resonances are optimized (see Fig. 6.14).

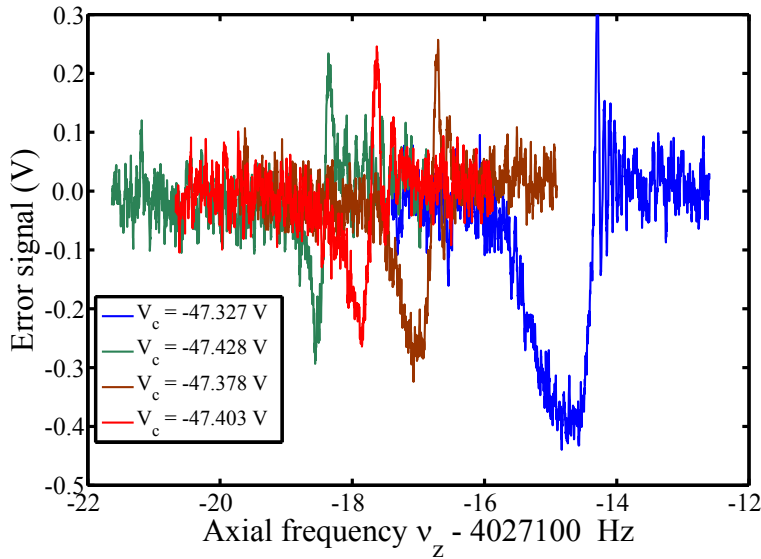


Figure 6.14: Axial resonances (all upsweeps) and the effect of guard tuning on their resonance shape. The effects of anharmonic pulling and the non-orthogonality of the trap are clearly visible.

With this method, the optimum guard setting can be determined to about 100 mV. However, the method is quite tedious, as the trap is non-orthogonal (resulting in the need to search the ions again after tuning) and each sweep takes about one minute. Consequently, as soon as an axial frequency lock can be achieved, the ions are brought into lock. Then the correction voltage is measured for two different axial drive strengths. For a perfectly harmonic trap, the change in the correction voltage should be exactly zero. The measurement is repeated for different guard voltages, and the guard setting with minimum change in the correction voltage is determined (see Fig. 6.15). However, in a real trap this setting does not result in a vanishing C_4 as higher order terms are present as well. With this method the optimum guard setting can typically be determined to about 25 mV. Assuming a D_4 of $-9 \cdot 10^{-3}$ (see section 4.1.1) and C_4 to be the dominant higher order correction, then C_4 can be minimized to about $5 \cdot 10^{-6}$ with this method.

A side effect of the tuning is a change in the other C -coefficients of the trap via the other non-zero D -terms. Here, D_2 is the leading order contribution due to the non-orthogonal design of the trap. The resulting shift in the ring voltage is traced as a function of the guard voltage. This can be accomplished in one measurement with the guard optimization by determining the slope of the change in the correction voltage. In lab jargon the quantity

$$c_{\text{guard}} = \frac{\Delta V_{\text{ring}}}{\Delta V_c} \quad (6.2)$$

is called the “guard constant”, even though it is not really a constant as can be inferred

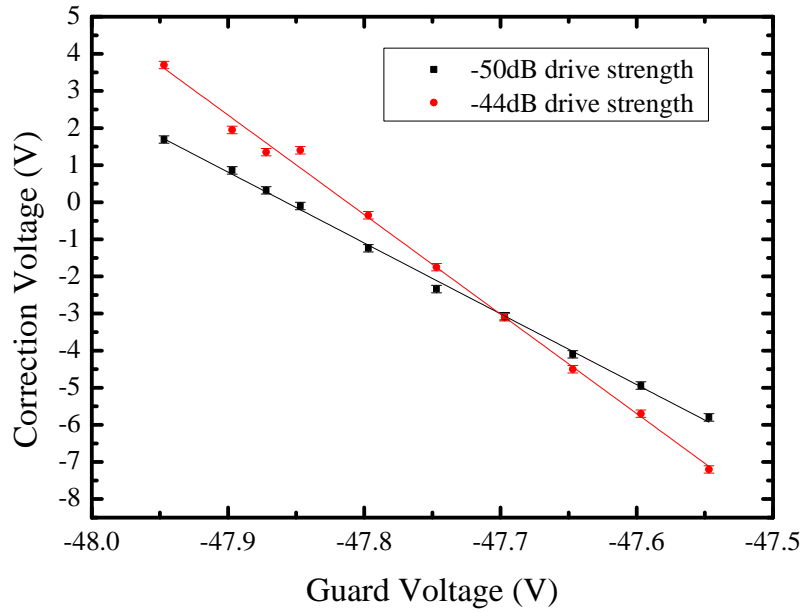


Figure 6.15: Finding the optimum guard voltage by comparing changes in the correction voltage (nominal full scale lock range: 2 mV) for different drive strengths. The drive strengths are given relative to the output of the synthesizer. A linear fit is applied to the data according to Eq. (3.58).

by the different slopes for different drives. This is caused by the higher order coefficients, which cause the axial frequency to become drive-dependent. In the limit of vanishing drive (and actually even vanishing amplitude of the ion) the slope would only depend on the D_2 term. In Fig. 6.15, the guard constant for the -50 dB setting of the drive is $1.62(3) \cdot 10^{-3}$ and for twice as strong setting of -44 dB it is $2.28(5) \cdot 10^{-3}$. But even for a given drive strength, the guard constant exhibits a non-constant behavior, which already has been mentioned in earlier Seattle work [VL04]. It is claimed that contamination will change the effectively measured guard constant due to space-charge distortions of the trapping potential. Obviously, it is very hard to verify this as the contamination cannot be detected directly. A more pronounced effect in the measurements is a strong change (by at least an order of magnitude) in the guard constant after cooling drives were applied to the ion cloud. This is due to the smaller magnetron and cyclotron radii, which brings the ions into the more harmonic volume of the trap.

A third quantity that can be determined from the guard optimization is an effective characteristic trap dimension d_{eff} . This quantity is important for predictions of the eigenfrequencies. It accounts for all harmonic contributions to the trap potential (e.g. including the guards) and is given as

$$d_{\text{eff}} = \sqrt{\frac{qV_h}{m\omega_z^2}} . \quad (6.3)$$

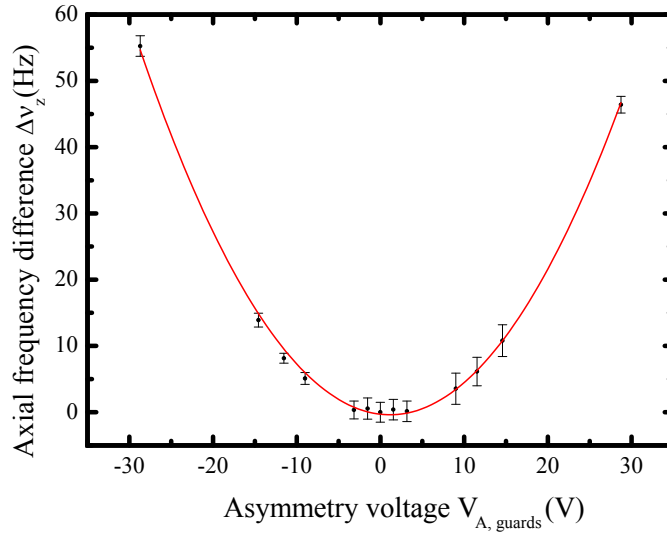


Figure 6.16: Measurement for the determination of the electric center of the trap. The frequency difference is given to an arbitrary reference point. The data points are the average of an up- and a downsweep, the error bars are given by the difference of the two sweep directions. The red line is a parabolic fit to the data. The minimum is found at $V_{A,guards}=1.17(16)$ V, the curvature is $0.062(1)$ Hz/V².

Here, V_h is the voltage when the trap is harmonic, given by the ring voltage at the crossing in Fig. 6.15 (89.7755(1) V). This leads to $d_{eff} = 2.123(3)$ mm, which is larger than the geometric d .

Finding the electric center of the trap

Effects such as patch potentials on the trap electrodes or imperfections in the manufacturing and assembly process of the electrodes can induce unwanted odd order contributions to the potential (see section 3.4.1). These can be mapped out by applying an asymmetric potential V_A across the trap. Typically, this was done by biasing one of the endcaps, however this was not possible for the configuration utilized in this measurement cycle. Therefore, the guard electrodes were run in an asymmetric configuration instead. The corresponding $V_{A,guards}$ is defined as the difference between the voltages of the lower and the upper guard electrodes. The electric center of the trap is found by determining the shift in the axial frequency as a function of $V_{A,guards}$ (see Eq. (3.57)) and finding the minimum of the resulting parabola (see Fig. 6.16). The center of the parabola is almost the symmetric configuration and so a shift about 80 mHz in the axial frequency is expected when using the symmetric configuration.

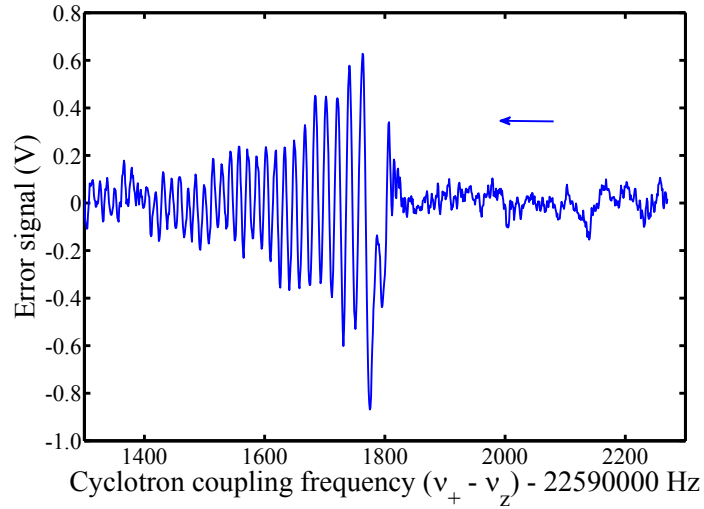


Figure 6.17: Modified cyclotron cooling resonance in the error signal. The modified cyclotron motion was excited before. Then, energy is transferred from the modified cyclotron mode into the axial mode and is dissipated in the tuned circuit. Typically, several of these sweeps are necessary before no more energy is transferred.

6.3.2 Measurements of the modified cyclotron frequency

The modified cyclotron frequency gives the dominant contribution to the determination of the free-space cyclotron frequency (see Eq. (3.71)). Therefore, the uncertainty of its determination finally determines the uncertainty of the mass measurements in the Penning trap. Hence, it is important to properly prepare the ions before every measurement in order to create reproducible results and minimize systematic errors. The steps of a typical measurement sequence are the following:

1. The ions are brought into axial frequency lock, so that they are in resonance with the tuned circuit.
2. The axial drive is turned 1 MHz away in order to bring the axial temperature in equilibrium with the tuned circuit. It is not turned off completely in order to avoid a systematic shift due to a change in the electrode temperatures discovered at the FSU/MIT-Trap [Red07].
3. Modified cyclotron cooling: Five cycles of a 250 Hz wide up- and down-sweep around the expected modified cyclotron cooling frequency $\nu_+ - \nu_z$ are applied. A typical response in the axial signal is shown in Fig. 6.17.

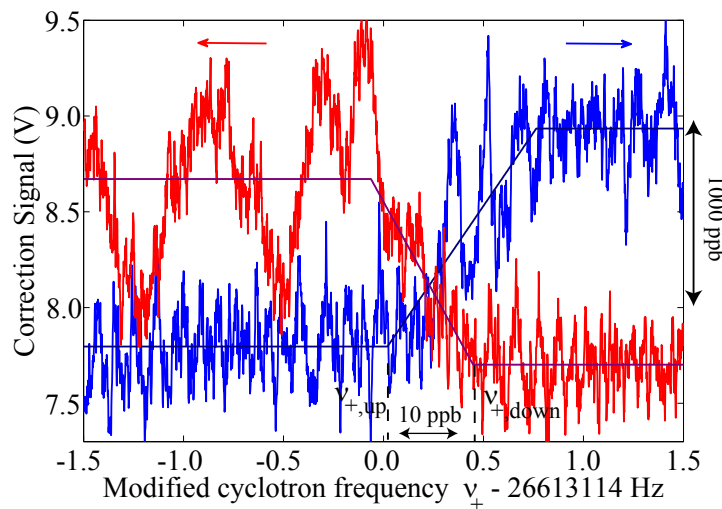


Figure 6.18: Modified cyclotron resonances for $^{12}\text{C}^{4+}$. Between the up- and downsweep the ions were cooled again, as described in the text. For the upsweep, beating, as expected from the theoretical treatment, is observed.

4. Magnetron cooling: Five cycles of a 250 Hz wide up- and downsweep around the expected magnetron cooling frequency $\nu_- + \nu_z$ are applied.
5. The axial drive is turned on again and an axial frequency lock is reestablished.
6. A cyclotron drive is swept (either up- or downsweep) and the response of the lock is recorded.

A typical sequence for the determination of one modified cyclotron data point includes an up- and a downsweep of the drive and takes about 5-10 minutes depending on the sweep rate in the modified cyclotron measurements. Fig. 6.18 shows an up- and a downsweep, which fit with the theoretically expected shape (see section 3.6.2). The modified cyclotron frequency is determined by finding the center frequency between the edges of the up- and the downsweep. The difference in frequency between the start of the up- and downsweeps is a function of the sweep settings and in particular the modified cyclotron drive strength. Typically, in Heidelberg differences of 250 mHz were achieved while in Seattle differences of down to 2 mHz were utilized. This is due to the higher modified cyclotron drive, which needs to be utilized as the axial frequency lock range cannot be set smaller than 2 mV due to the problems with the voltage source (see section 6.3.1). However, the center frequency determined from the two sweeps should remain the same. This is also supported by the long-term measurement series (see Fig. 6.21), where the standard deviation of the data points is 20 mHz or better. However, not all modified cyclotron resonances recorded so far, can be fitted as nicely as the ones shown in Fig. 6.18. Sometimes the behavior right

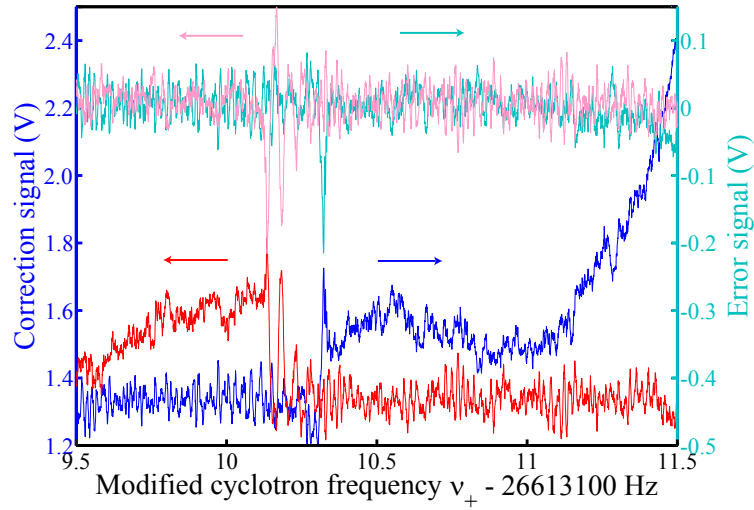


Figure 6.19: Modified cyclotron resonances in the error and the correction signal. The error signals are given in light colors, the correction signal in bright colors. As the correction signal deviates from the expected shape coincidence with the error signal helps to find the edges.

after triggering the excitation is rather random as the axial lock is lost and the correction signal wanders around freely. Again, this is attributed to the need for a too high cyclotron drive due to the limited lock range of the precision voltage source. In order to still be able to make use of these modified cyclotron sweeps, a semi-automatic fitting program [Höc13], relying on the expertise of the experimenter in finding the onset of the excitation, is utilized. The determinations of the program can also be checked by looking at the error signals, where also a signature of hitting the modified cyclotron resonance can be found (see Fig. 6.19).

Determination of the magnetic field

The determination of the modified cyclotron frequency and the resulting cyclotron frequency also allows to measure the magnetic field very accurately. The basis is Eq. (3.70). In fact, utilizing the ions is the only way to determine the relevant magnetic field as the magnetic susceptibilities of the trap modify the magnetic field at the location of the ions. As the influence of the magnetron frequency on the determination of the magnetic field is very small and only small shifts of ν_- have been observed in a long-term measurement, it typically is only measured about once per day. The measurement series for monitoring the magnetic field hence consists of a series of modified cyclotron frequency measurements as the axial frequency is fixed by the axial frequency lock. Modified cyclotron data with one measurement about every 5 minutes could be taken over several weeks during

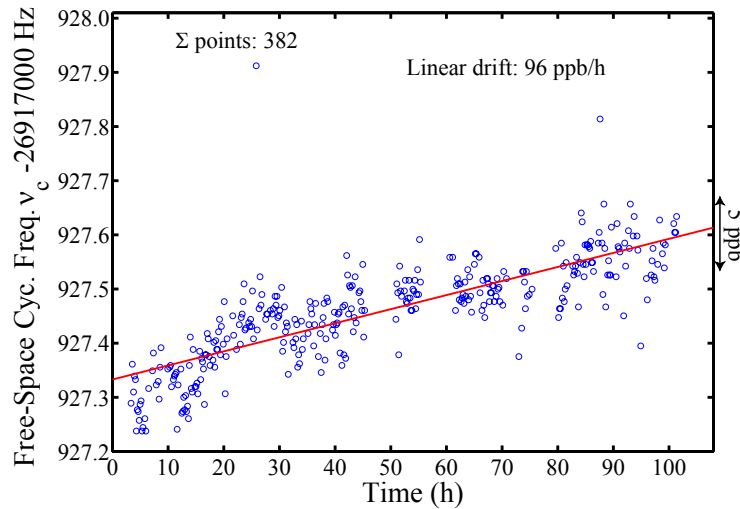


Figure 6.20: The drift of the magnetic field over 100 hours, observed by measuring cyclotron resonances for $^{12}\text{C}^{4+}$.

this work. The absolute size of the magnetic field can only be determined for a specific instant in time from these data as a filling of the magnet with liquid helium changes the modified cyclotron frequency irreversibly by several Hz (corresponding to shifts on the order of hundreds of ppb). From the longest almost continuous measurement, the magnetic field can be determined to be 5.2577749(3) T directly after a filling of the magnet. Higher precision in the magnetic field determination is inhibited by the poor knowledge of the elementary charge (only known to 25 ppb) and the conversion factor from the atomic mass unit to the kilogram (only precise to 50 ppb) [MTN08]. A recent NMR measurement [Tre11] yielded a field of 5.2580272(4) T. This measurement was performed without the traps and shows that the magnetic susceptibility of the traps makes a clearly observable difference in the magnetic field. The relative magnetic field drift is 92 ppt/h. Evaluating other data sets yields drifts in a range of 100(50) ppt/h. The last Seattle measurements, shown in Fig. 6.1, yielded a stability of 1.7 ppt/h. The difference is attributed to a recently discovered linear pressure increase in the absolute pressure reference of the stabilization system of about 40 hPa in three months (corresponding to an average drift of 1.85 Pa/h). The dependence of the modified cyclotron frequency on a pressure shift was determined to be 2.36(37) mHz/Pa (for $^{12}\text{C}^{4+}$) [Str11]. Hence, the drift of the pressure reference corresponds to an average drift of 162 ppt/h and can fully explain the additional drift in the data. Further studies of environmental effects on the cyclotron data are in preparation [Str12].

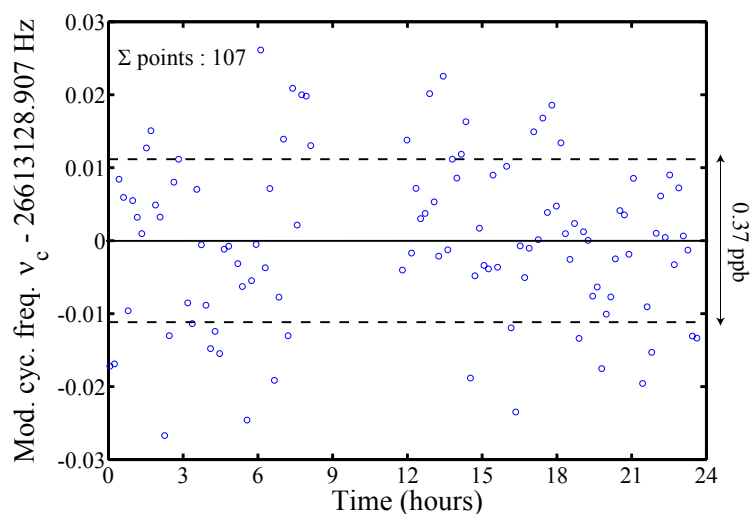


Figure 6.21: Modified cyclotron data after removing a linear drift of 150 ppt/h. The standard deviation of a single point is 0.375 ppb (dashed line) and an error in the center frequency of 0.038 ppb. The gap in the data after 9 hours is caused by other tests with the ions, carried out in this time.

Current precision of the spectrometer

Subtracting the linear drift from the data of Fig. 6.20 it is possible to determine the present level of precision achieved with the spectrometer. The standard deviation of the residual data is 58 mHz (2 ppb). The standard deviation of the mean value is 0.1 ppb as 380 cyclotron data points were taken. The highest precision in the modified cyclotron determination achieved with the spectrometer was 0.04 ppb in a similar, but shorter measurement series of 100 data points over one day (see Fig. 6.21). This is less than one order of magnitude away from the values achieved in Seattle (see Fig. 6.1).

6.3.3 Magnetron frequency measurements

Magnetron frequency measurements are often neglected in high-precision Penning trap mass spectrometry. The reason is the low weight of the magnetron frequency ν_- in the determination of ν_c (see Eq. (3.71)). The basic measurement technique for the determination of the magnetron frequency is similar to the already described modified cyclotron frequency measurements. The ion is brought into axial frequency lock, prepared (by the same steps as for the modified cyclotron motion) and a drive is scanned in order to transfer energy to the magnetron motion. However, not the direct magnetron drive is utilized as the ions could be lost due to the instability of the mode, but a drive at the magnetron cooling frequency (see section 3.5). A typical measurement of the magnetron frequency is shown

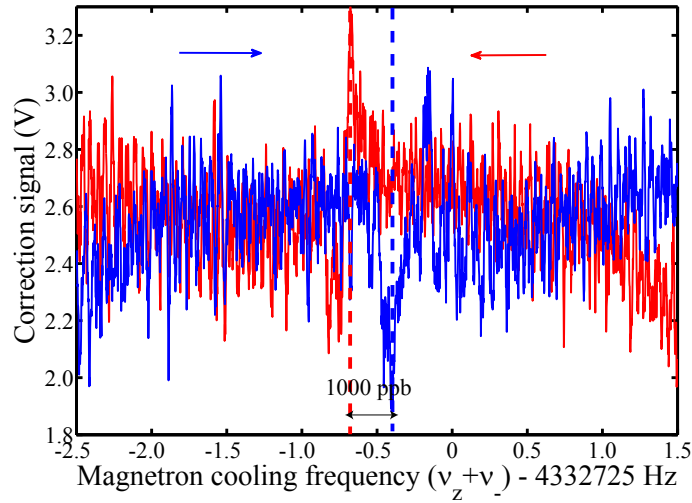


Figure 6.22: Magnetron cooling resonances of $^{12}\text{C}^{4+}$. The dashed lines indicate the up- and down-sweep positions of the magnetron frequency.

in Fig. 6.22. The quickly regenerating drop in the lock is attributed to the energy transferred into the axial mode during the sweep, which quickly is damped again. The shape is in good agreement with earlier Seattle measurements [VL04].

In a typical mass measurement series, the magnetron frequency is only measured about once per day, however in order to ensure that the magnetron frequency is really as stable as one would expect a long-term measurement of the magnetron cooling frequency was performed. The result is shown in Fig. 6.23.

Effective trap angle measurement

Two methods for determining the trap angle in-situ have been described in section 6.1.3. A check of the results of these methods is possible by utilizing measurements of the magnetron frequency. The method relies on measuring the three eigenfrequencies and inserting them in Eq. (3.62). This way the misalignment angle θ can be determined, assuming $\varepsilon \approx 0$. Measurements for $^1\text{H}^+$, $^{12}\text{C}^{4+}$ and $^{16}\text{O}^{6+}$ are summarized in Tab 6.2. The results are in

Ion	Trap angle θ in degree
$^1\text{H}^+$	0.781(9)
$^{12}\text{C}^{4+}$	0.777(3)
$^{16}\text{O}^{6+}$	0.779(1)

Table 6.2: Result of trap angle measurements via the magnetron frequency.

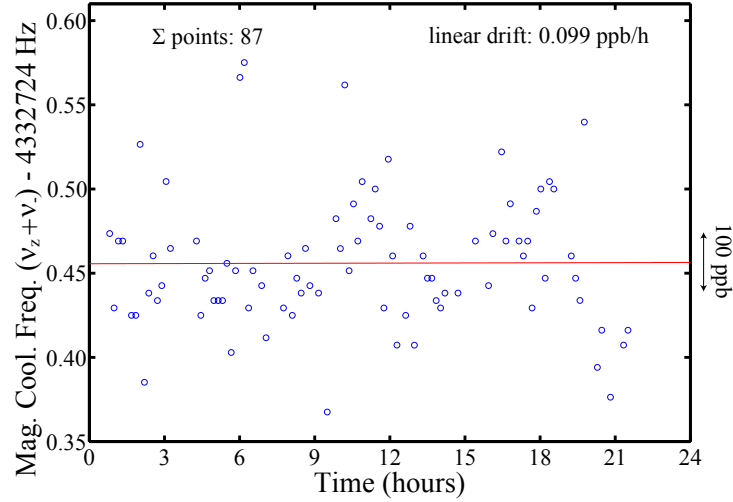


Figure 6.23: Magnetron cooling frequency $\nu_z + \nu_-$ of $^{12}\text{C}^{4+}$ over time. The center was fitted to be 4332724.45 Hz. The relative standard deviation of a single data point (compared to ν_-) was 127 ppb. The temporal drift was 0.099 ppb/h as indicated by the red fit line. The axial drive frequency was 4027800 Hz.

good agreement within their error bars. A measurement with the electron beam from the field emission point yielded a verification of this result, as EtSkim was hit. From the geometry of the traps it can be derived that the angle hence has to be between 0.60° and 0.91° . This result also poses an upper boundary on the ellipticity $\varepsilon < 3 \cdot 10^{-2}$. Both ε and θ will not influence the uncertainty in the mass measurements as long as they are stable and all three eigenfrequencies are measured according to the invariance theorem given in (Eq. 3.70).

6.4 Mass measurements

The ultimate figure of merit for a mass spectrometer is the precision and accuracy that is achievable. Therefore, first mass measurements on $^1\text{H}^+$ and $^{16}\text{O}^{6+}$ were performed in the context of this thesis despite several problems already discussed above. Both these masses are known to an uncertainty of at least 1 part in 10^{10} [VDZS01, VDPVLZ06, SBN⁺08]. Therefore, the measurements of these masses serve as a strong test for the accuracy achieved with the MPIK/UW-PTMS so far. The current precision and accuracy of the spectrometer and in particular their limitations also give important input for further improvements of the spectrometer.

Before performing the analysis of the mass ratio, the cyclotron data have to be reconstructed from the available measurements of the eigenfrequencies. This is achieved by

utilizing the invariance theorem (Eq. (3.70)). The mass ratio $R = q_B/q_A \cdot CFR$ of two ions is then derived from their cyclotron frequency ratio (CFR). When the two ions have not been measured simultaneously, it is important to account for drifts in their cyclotron frequencies, being caused by drifts in the magnetic field. The functional dependence of the magnetic field wander is not understood very well; the flux creep should be a logarithmic decay [And62], but other parameters such as the pressure in the magnet also play an important role. Therefore, normally a polynomial is fitted to the data. Different groups came to different results on the optimum order (varying from first to sixth order) [VL04, Red07].

The latest Seattle fits were second order fits (though the quadratic component was fairly small) to the magnetic field with addition of a term representing the external pressure data [VL04]. For the analysis presented here, it was decided to utilize a linear fit only, as more data would be necessary to judge whether higher orders will give a more realistic picture of the fluctuations in the data.

The predicted cyclotron frequencies are hence assumed to be given as

$$v_{c,A}(t) = v_{c,A}(0) \cdot (1 + c_1 \cdot t) \quad (6.4)$$

$$v_{c,B}(t) = CFR \cdot v_{c,A}(0) \cdot (1 + c_1 \cdot t) \quad (6.5)$$

Here, CFR is the cyclotron frequency ratio, c_1 is the linear drift in the cyclotron frequency, t is the time difference to an arbitrary zero-point in time and $v_{c,A}(0)$ is the cyclotron frequency of ion A at $t = 0$. The fit parameters of a least-squares fit performed on the data are CFR , $v_{c,A}(0)$ and c_1 . Two different approaches for the fit have been considered: Firstly, the parameters c_1 and $v_{c,A}(0)$ can be determined from data of ion A only (in this work, ion A would always be $^{12}\text{C}^{4+}$), then CFR is determined from the data of ion B. Secondly, a fit of all three parameters at a time can be performed, taking both data of ion A and B into account. So far, the second approach was followed, differences in the results of the two approaches are discussed in section 6.4.3.

The statistical error of the free-space cyclotron frequency can be determined from the individual statistical errors of all three eigenfrequencies by Gaussian error propagation (when the errors are independent)

$$\Delta v_c = \sqrt{\left(\frac{v_+}{v_c} \Delta v_+\right)^2 + \left(\frac{v_z}{v_c} \Delta v_z\right)^2 + \left(\frac{v_-}{v_c} \Delta v_-\right)^2} \quad (6.6)$$

The statistical error of the modified cyclotron frequency Δv_+ is determined by the single-point standard deviation of the fit residuals. This is a conservative estimate, in principle also the standard deviation of the mean value of the residuals can be utilized (which scales down with \sqrt{N} , where N is the number of measurements).

The statistical error of the axial frequency is determined by the fluctuations of the ring voltage ΔV_{ring} (see section 6.3.1). Again an upper limit, determined from the standard deviation of the fit residuals of the modified cyclotron frequency, is utilized as a conservative estimate due to the problems with the precision voltage source. Effectively, this results

in an contribution to the statistical error exactly equal to that of the modified cyclotron frequency.

The statistical error in the determination of the magnetron frequency is given by the uncertainty of its determination (as it typically is only measured once), so by the frequency difference between an up- and a down sweep (see Fig. 6.22). This error typically does not contribute significantly to the overall statistical error.

As the statistical errors of the modified cyclotron frequency and the axial frequency are not independent in this approach, the statistical error is estimated as $\Delta v_c = 2\Delta v_+$. The statistical error of the frequency ratio is then determined by Gaussian error propagation from the errors of the cyclotron frequencies.

6.4.1 The proton mass measurement

The determination of the ${}^1\text{H}^+ / {}^{12}\text{C}^{4+}$ cyclotron frequency ratio, and hence the proton mass m_p , was the very first mass measurement carried out with the MPIK/UW-PTMS. They were carried out with a cloud of protons (3.9(5) Hz line-width correspond to about 30 protons) as it was not possible to isolated single protons. The measurement consists only of some data points for the protons as the axial lock for the protons was very unstable and could not be established automatically. This was caused by the non-standard way of achieving the lock: Instead of using the precision voltage source directly, which is not possible due to the limited range, the output of the guard voltage divider was utilized as a source for the ring. The disadvantage of this approach is the long RC time of about 30 s, which makes the axial frequency lock very unstable. Therefore, the data points for the protons were taken manually. For the carbon reference data automatic data-taking was available (actually for the first time since the MPIK/UW-PTMS was started). One night of reference data was available and hence the magnetic field drift is mainly determined from these data. The data are shown in Fig. 6.24. The fit to the data yields a cyclotron frequency ratio of 2.977 783 65(11). The precision of the measurement is 36 ppb, dominated by the error of the proton measurement. The deviation from the best measured value of 2.977 783 718 335(74) [VDZS01, SBN⁺08] is 20 ppb. The statistical errors of the measurement are summarized in Tab. 6.3.

	${}^1\text{H}^+$	${}^{12}\text{C}^{4+}$
Δv_+ (Hz)	1.46 (18 ppb)	0.01 (0.4 ppb)
Δv_z (Hz)	28.98 (7 ppm)	0.65 (0.2 ppm)
Δv_- (Hz)	2 (19 ppm)	1 (3 ppm)
Δv_c (Hz)	2.91 (36 ppb)	0.02 (0.7 ppb)

Table 6.3: Absolute and relative statistical errors for the proton measurement.

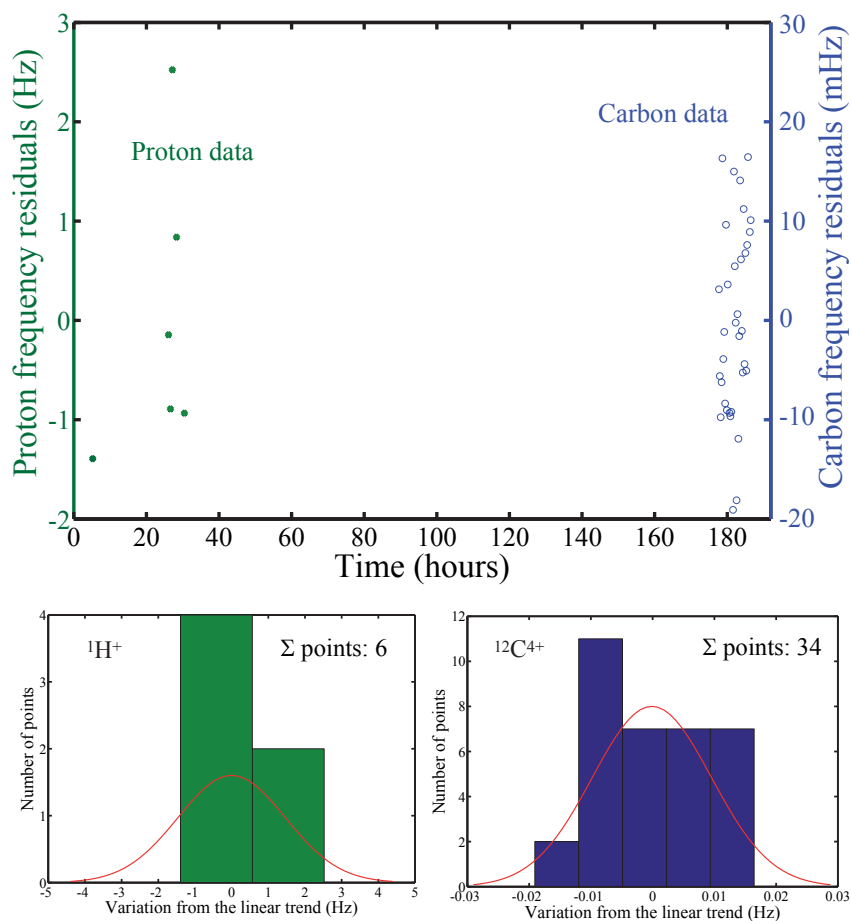


Figure 6.24: The proton data set. A linear trend of 51.7 ppt/h was removed from the data. The fitted cyclotron frequency ratio is 2.977 783 65(11). The long time between the measurements was caused by a number of other tests carried out in between.

	$^{16}\text{O}^{6+}$	$^{12}\text{C}^{4+}$
Δv_+ (Hz)	0.044 (1.5 ppb)	0.068 (2.6 ppb)
Δv_z (Hz)	0.323 (80 ppb)	0.444 (110 ppb)
Δv_- (Hz)	0.25 (0.9 ppm)	1 (3 ppm)
Δv_c (Hz)	0.087 (2.9 ppb)	0.135 (5.0 ppb)

Table 6.4: Absolute and relative statistical errors for the oxygen measurement.

6.4.2 The oxygen mass measurement

The oxygen mass determination was carried out in a more systematic way than the proton mass determination. By adjusting the detection frequency such that it coincides with the ion's natural frequency in the 80-90 V range of the voltage source, it was possible to achieve an axial lock for both ions. Therefore, automated data-taking was available for all data points. For the oxygen a line-width of 300(50) mHz was measured, which probably corresponds to two ions, however no extensive studies on this issue were performed. The result for the cyclotron frequency ratio is 1.125 383 451(7). The precision of the measurement is 7 ppb. The deviation from the best measured value of 1.125 383 463 469(24) [VDPVLZ06] is 10 ppb. The statistical errors are summarized in Tab. 6.4, the data after removing a linear drift are shown in Fig. 6.25.

6.4.3 Systematic shifts

Important for achieving not only highly precise but also highly accurate mass measurements is a profound knowledge of the systematic shifts and errors on both the single frequency measurements and their ratio *CFR*. Years of studies have been invested in determining these effects at the University of Washington [VDPVLZ06]. As the traps of the MPIK/UW-PTMS have been manufactured the same way and the dimensions are identical, many of the systematic effects should be very similar. However, some of the systematics have not yet been investigated in Heidelberg and have to be studied further in the future. Also, so far systematic studies have only been carried out for the $^{12}\text{C}^{4+}$ ion. A number of systematic shifts and errors on all eigenfrequencies will be presented here (and summarized in Tab. 6.6) before a final discussion of the mass measurements follows.

Image charge shift

The image charges induced on the electrodes by the charge of the ions shifts the eigenfrequencies of the ion (see section 3.4.3). The overall shift in the cyclotron frequency [Por01] is given as

$$\delta_c = \frac{2\Delta_\rho + \Delta_z}{\omega_c + \sqrt{\omega_c^2 - (2\Delta_\rho + \Delta_z)}} \approx \frac{2\Delta_\rho + \Delta_z}{2\omega_c} = C_e \frac{Q}{B} . \quad (6.7)$$

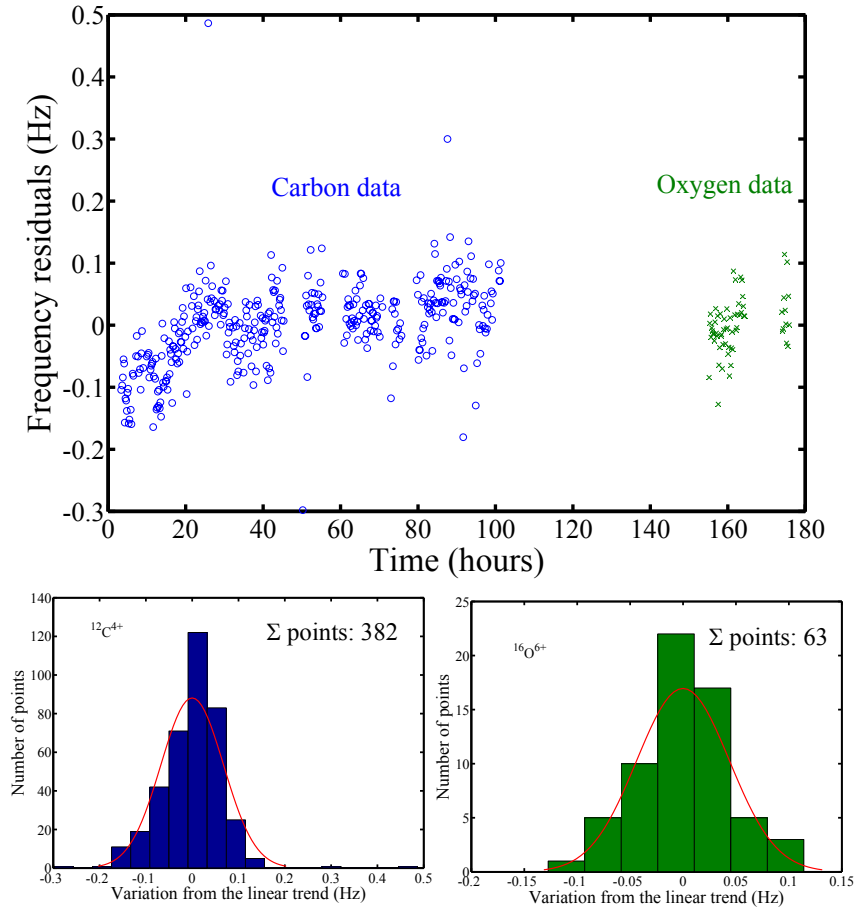


Figure 6.25: The oxygen data set. A linear trend of 53.1 ppt/h was removed from the data. The fitted cyclotron frequency ratio is 1.125 383 451(7).

Here, C_e is a characteristic constant of the trap, depending on the geometry only and Q is the overall charge in the trap given as $Q = N \cdot q = n_q \cdot e$, where N is the number of ions, q is the charge of a single ion and n_q the total number of charges in the trap. As C_e has neither been calculated nor measured for the MPIK/UW-PTMS so far, old Seattle values are taken in this evaluation. For the UW-PTMS measurements a quantity called $\xi = C_e/B$ was determined as a constant of the trap (which is true for a given magnetic field B). The reported value is $\xi = 2.23(9)\text{mHz}/n_q$. Scaling this value by the magnetic field of the UW-PTMS (derived to be 5.8966 T from [VL04]) results in $C_e = 0.37(2)\text{mHz}\cdot\text{T}/n_q$. For the MPIK/UW-PTMS this results in $\xi = 1.95(1)\text{mHz}/n_q$. As ξ has not been determined in the MPIK/UW-PTMS and the number of ions N could not be determined exactly, it will not be taken as a correction to the data (as it was the case for the Seattle data), but as a full systematic error.

Ion-of-interest	$^{12}\text{C}^{4+}$	$^1\text{H}^+$	$^{16}\text{O}^{6+}$	$^3\text{H}^+, ^3\text{He}^+$
$\frac{\delta\nu_c}{\nu_c}(B_2, E_+) [\text{m}^2/(\text{eV}\cdot\text{T})]$	$7 \cdot 10^{-15}$	$1 \cdot 10^{-15}$	$3 \cdot 10^{-15}$	$29 \cdot 10^{-15}$
$\frac{\delta\nu_c}{\nu_c}(\text{rel}, E_+) [1/\text{eV}]$	$-90 \cdot 10^{-12}$	$-1066 \cdot 10^{-12}$	$-68 \cdot 10^{-12}$	$-360 \cdot 10^{-12}$
$\frac{\delta\nu_c}{\nu_c}(C_4, E_+) [1/\text{eV}]$	$-2.16 \cdot 10^{-6}$	$-0.08 \cdot 10^{-6}$	$-1.50 \cdot 10^{-6}$	$-2.20 \cdot 10^{-6}$
$\frac{\delta\nu_c}{\nu_c}(B_2, E_z) [\text{m}^2/(\text{eV}\cdot\text{T})]$	$2.4 \cdot 10^{-9}$	$28.8 \cdot 10^{-9}$	$1.8 \cdot 10^{-9}$	$9.6 \cdot 10^{-9}$
$\frac{\delta\nu_c}{\nu_c}(\text{rel}, E_z) [1/\text{eV}]$	$-45 \cdot 10^{-12}$	$-532 \cdot 10^{-12}$	$-34 \cdot 10^{-12}$	$-179 \cdot 10^{-12}$
$\frac{\delta\nu_c}{\nu_c}(C_4, E_z) [1/\text{eV}]$	$-93.5 \cdot 10^{-6}$	$-31.4 \cdot 10^{-6}$	$-83.1 \cdot 10^{-6}$	$-94.0 \cdot 10^{-6}$
$\frac{\delta\nu_c}{\nu_c}(B_2, E_-) [\text{m}^2/(\text{eV}\cdot\text{T})]$	$4.9 \cdot 10^{-9}$	$57.8 \cdot 10^{-9}$	$3.6 \cdot 10^{-9}$	$19.5 \cdot 10^{-9}$
$\frac{\delta\nu_c}{\nu_c}(\text{rel}, E_-) [1/\text{eV}]$	$2.0 \cdot 10^{-12}$	$2.6 \cdot 10^{-12}$	$1.2 \cdot 10^{-12}$	$8.1 \cdot 10^{-12}$
$\frac{\delta\nu_c}{\nu_c}(C_4, E_-) [1/\text{eV}]$	$-2.16 \cdot 10^{-6}$	$-0.08 \cdot 10^{-6}$	$-1.50 \cdot 10^{-6}$	$-2.20 \cdot 10^{-6}$

Table 6.5: Shifts in the cyclotron frequency due to the coupling of the eigenmotions. The shifts can be calculated by multiplying the energies and the coefficients B_2 or C_4 with the values given in the table. For the relativistic shifts (rel) only the energy has to be multiplied.

Energy-dependent shifts

The coupling terms utilized for the radial detection B_2 , C_4 and the relativistic coupling (see section 3.4.1) also induce shifts in all eigenfrequencies (see the thesis of Farnham [Far95] for a summary of all shifts). These shifts depend on the energies E_+ , E_z and E_- . An evaluation of the resulting shift in the free-space cyclotron frequency ν_c is given in Tab. 6.5 for different ions-of-interest. Due to the cooling of the eigenmotions, their energies are determined by the energy of the axial mode via the relations Eq. (3.68) and (3.66). The axial energy was determined in Seattle for electrons to be slightly above the energy expected from the 4-K environment. An effective temperature of 12 K fitted best in these studies [Far95]. As a different amplifier is utilized now, this temperature can be different and will be determined in the future. Also the axial energy of the driven ions should be somewhat higher than their thermal energy. From comparing the signal-to-noise ratio in axial frequency sweeps it can be estimated that the drive energy is about a factor of 2 larger. Energies in the cooling limits for 4 K are given in Tab. 3.1.

C_4 was estimated to be about $5 \cdot 10^{-6}$, when the guards are properly tuned (see section 6.3.1). B_2 could only be determined by an NMR-measurement without the traps so far [Tre11] to be 0.2 T/m^2 . Typical B_2 values for the magnet systems with the traps inserted in Seattle were around 1 T/m^2 . However, this was for a shimmed magnet and a different distribution of magnetic materials around the ion, so a higher B_2 seems inevitable. A way to determine the B_2 with the traps inserted in the magnet, is to properly map the field by moving the ion in the trap. This can be achieved by asymmetrically biasing the endcaps, which was not possible so far due to the endcap bias lines not being connected.

Analyzing Tab. 3.1 for $C_4 \leq 10^{-5}$ and $B_2 \geq 0.1 \text{ T/m}^2$ shows that the leading shift for all analyzed isotopes in the free-space cyclotron frequency is the $\frac{\delta v_c}{v_c}(B_2, E_z)$ -term. In the Seattle measurements, this shift therefore was corrected for. For a conservative estimation an axial energy of 7 meV and a B_2 of 10 T/m^2 are assumed. This corresponds to the axial temperature being ten times the liquid helium temperature, the drive being two times as strong as the thermal energy and a B_2 ten times worse than in Seattle. For more accurate mass measurements this shift should be mapped and removed from the data.

Shifts due to the detection system

Recently, a shift due to the modulation of the ring potential (as discussed in section 3.4.3) was measured. The axial frequency is shifted by $-6.7(7) \text{ Hz}$ (for $^{12}\text{C}^{4+}$) for the modulation amplitude chosen for the experiment. This corresponds to a $\chi^2 = 2.7(3) \cdot 10^{-5}$ and a modulation amplitude $V_{\text{mod}} = 0.46(2) \text{ V}$. The effect on the cyclotron frequency for a single ion is given by

$$\omega'_c = \omega_c \left[1 - \frac{1}{16} \left(\frac{\omega_z}{\omega_c} \right)^2 \cdot \chi^2 \right] . \quad (6.8)$$

This results in a 40 ppb shift of the cyclotron frequency of $^{12}\text{C}^{4+}$. Fortunately, it can be shown that the shift cancels for a cyclotron frequency ratio measurement because the relative correction is the same for both species. Utilizing Eq. (3.11) and Eq. (3.14) results in

$$\left(\frac{\omega_z}{\omega_c} \right)^2 \cdot \chi^2 = \left(\frac{V_{\text{mod}}}{\omega_z \cdot B \cdot d^2} \right)^2 . \quad (6.9)$$

Here, V_{mod} was constant for all measurements, while the changes in ω_z and B were so small that the change in the cyclotron frequency ratio is well below the 1 ppt level. However, the modulation also affects the modified cyclotron motion and the magnetron motion. Calculating this shift [Ket11] results in

$$\Delta\omega_{+,-} \approx \mp \frac{\omega_c}{8} \cdot \left(\frac{\omega_z}{\omega_c} \right)^4 \cdot \chi^2 . \quad (6.10)$$

This shift does not cancel in the frequency ratio. For $^{12}\text{C}^{4+}$ it is an effect of 2 ppb. For future measurements weaker modulation will be utilized in order to completely avoid this shift. The minimum useful modulation is finally limited by the coupling of the axial drive signal onto the amplifier as stronger drive is needed to compensate for the weaker modulation.

Two other potential errors related to the detection system have become evident. The first is given by the difference in frequency between axial frequency up- and downsweeps, which often is observed (see section 6.3.1). The differences observed were up to 2 Hz. As the cause of the difference is not yet clear, it is also not clear on what frequency the axial locked loop is locking (upsweep frequency, downsweep frequency or something in

between) and whether the frequency is shifted with respect to the natural frequency. Until the issue is resolved, a systematic error of 2 Hz in the axial frequency will be assumed.

The second error is related to setting the correct phase for the detection. This was complicated by the different shapes and hence different phases in the fit in the axial up- and downsweeps as discussed in section 6.3.1. An incorrectly set detection phase ϕ_{det} causes the locked loop to lock to an incorrect phase $\phi(\omega_{\text{d}})$ between drive and ion. This causes a lock to a frequency different from the natural axial frequency, as can be seen by inverting Eq. (3.39) and assuming $\delta\omega_z = \omega_{\text{d}} - \omega_z \ll \omega_z$. This results in

$$\Delta\omega_z \approx -\gamma_z \tan(\Delta\phi_{\text{det}}) \quad . \quad (6.11)$$

A conservative estimate is a detection phase error $\Delta\phi_{\text{det}} \approx 30^\circ$, for the particle line-widths a factor of 2 is multiplied to the measured widths due to the distortion by the beating. With an improved signal shape (e.g. like in Fig. 6.11), an improvement down to about 1° seems feasible. Also this systematic can be mapped by taking cyclotron resonances at different phase settings of the detector.

Shifts due to magnetic and electrostatic gradients

A shift in the electrostatic center positions of the different ions with respect to the magnetic field center can cause a systematic shift in the cyclotron frequency ratio due to the higher order terms in the magnetic field (see Eq. (3.51)). These result in a change of the magnetic field strength depending on the spatial position. The mean spatial position of the ion can be changed by asymmetrically biasing the endcaps. However, this measurement was not possible due to the endcap bias lines not being connected for reduced noise pickup, as discussed in section 6.1.1. A rough estimate of the maximum displacement between two loads is given by the well-drops. As these can be performed down to 20 mV typically an asymmetric potential V_{A} at the endcaps (e.g. due to patch potentials) should be well below 100 mV. The resulting shift in axial position Δz is given by Eq. 3.56.

From the Seattle measurements, it is known that B_1 was about $7 \mu\text{T/m}$, being compensated by the correction coils wound around the trap chamber. However, before compensation, the B_1 was a factor of 200 worse [VDPVLZ06, Far95]. Without the traps being inserted a B_1 of 0.1 mT/m was determined in the most homogeneous part of the magnetic field in a recent NMR measurement [Tre11]. For the estimation of the shift due to the magnetic gradient an assumption of a B_1 of 7 mT/m (a factor 1000 larger than in Seattle) is made. The error in the magnetic field can be determined from $\Delta B = B_1 \cdot \Delta z$, the error in the cyclotron frequency via error propagation. The sign of the shift depends on the signs of B_1 and ΔV and hence is unknown right now.

An asymmetric electric potential also causes a shift in the axial motion. As already discussed in section 6.3.1, this shift was about 80 mHz in the axial frequency for the $^{12}\text{C}^{4+}$. It was not determined for the other ions (as it is no relevant effect at the current level of precision) and is estimated from the ratio of $V_{0,\text{C}}/V_{0,\text{ion}}$.

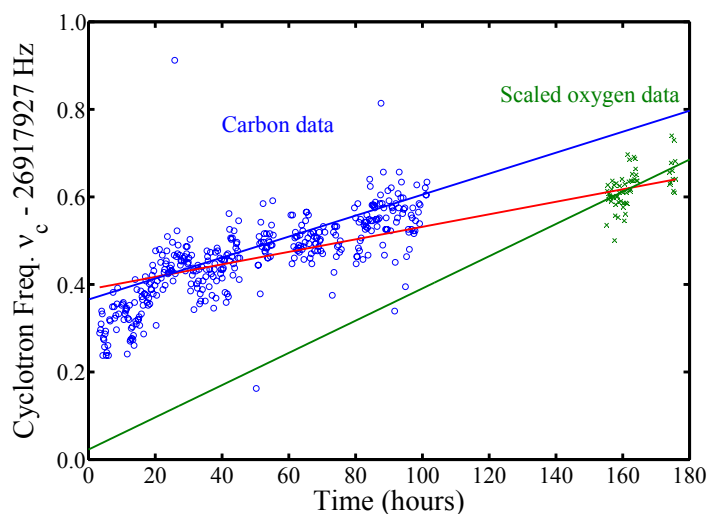


Figure 6.26: The oxygen data set before removing a linear drift. The red line indicates a fit of 53.1 ppt/h and a cyclotron frequency ratio of 1.125 383 451(7). The blue line is a separate fit to the linear drift of the carbon data only, the green line a separate linear fit to the drift of the oxygen data only.

Errors due to the fitting routine and a possible non-linearity of the magnetic field drift

Other systematic errors can be induced from the modified cyclotron fitting routine. E.g. for the Seattle data acquisition system a systematic shift in the fitting routine depending on the range of the modified cyclotron sweeps was determined. For the semi-automated fitting system currently utilized, a systematic human bias factor could in principle be present. Typical widths of the modified cyclotron frequency sweeps are 2 Hz. An accuracy of better than 10% of the full sweep range in finding the edge of the resonance seems realistic, in particular comparing this to the clearly discernible overall difference between the up- and downsweeps of 250 mHz or below for the data obtained so far (in Seattle even smaller differences of some mHz could be obtained for smaller modified cyclotron drives). Also partly the finding of the edge will be a random process for a human evaluator and so it will be also covered by the statistical error. However, before further investigations an systematic error of 10% of the sweep width will be assigned. Improvement is expected from a higher voltage source stability, which will allow much narrower sweep ranges.

Also the global linear magnetic field fit can contribute to the error. It is not clear at all, that the magnetic field necessarily changes linearly at all times. The global fit for the three parameters R , $v_{c,A}$ and c_1 for the oxygen and carbon data e.g. results in a c_1 of 53 ppt/h, which fits the data best. However, separately fitting the c_1 of the carbon data results in 92 ppt/h, separately fitting the c_1 for the oxygen in 136 ppt/h (see Fig. 6.26). Fixing c_1 in

the global fit to the 92 ppt/h of the carbon (ignoring the drift of the oxygen), e.g. results in a change in the mass ratio of 4 ppb (further away from the literature value though). Assuming that c_1 changed from 92 ppt/h to 136 ppt/h between the carbon and the oxygen measurement yields another possible error of about 4 ppb. For a conservative estimate the error due to the magnetic field drifts is estimated to be below 10 ppb. Improving the magnetic field stabilization further to the Seattle value, minimizing the fluctuations of the data and the time differences between the measurements should help to eliminate this effect. Also more statistics on the magnetic field behavior and more data points in the mass measurements will improve the situation for future measurements.

Other possible shifts

Of course other systematic shifts cannot be excluded, even though the UW-PTMS data at a precision level of 1 part in 10^{11} are likely to have revealed many of these. However, the measurements in the UW-PTMS claim to have had single ions with no contamination. Therefore, more than single ions and contamination can in principle induce systematic shifts via their space-charge. Estimations on upper limits for these effects can be made from a comparison between a load of a larger cloud (line-width 4 Hz) and a load of only 1-2 ions (line-width 150 mHz) within one day. The difference in the modified cyclotron frequency was below 100 mHz (the resolution of the measurement with the cloud was no better than this) and the same held true for the magnetron frequency. Hence, no shift bigger than some ppb in the modified cyclotron frequency is expected from contamination and cloud effects.

6.4.4 Summary of the mass measurements

For a final evaluation of the proton and oxygen mass measurements it is important to include both the statistical (see sections 6.4.1 and 6.4.2) and systematic errors (see section 6.4.3). For the conservative estimates taken on both the modified cyclotron and the axial frequency error, the overall statistical error reaches a level of 10 ppb. In the proton measurement it is somewhat worse, but this is easily understood by the difficult conditions of this measurement. Gaining more confidence (and improving on) both in the precision voltage source and the magnetic field stability, probably the standard deviation of the mean value of the fitted modified cyclotron residuals would be taken as the statistical error (being a factor \sqrt{N} smaller, where N is the number of measurements). For some of the measurements presented here, this has already reached a 0.1 ppb level or even below. However, it seems pointless to state uncertainties on this level before the systematics of the spectrometer have been fully determined on a sub-ppb level.

The evaluation of the systematic errors is more complicated at the current state of the experiment. Many shifts can only be estimated and hence might significantly differ in reality. Here, it was always tried to perform a conservative estimation of the effects. The results for the systematic errors are summarized in Tab. 6.6. No overall systematic error

	$^{16}\text{O}^{6+}$	$^{12}\text{C}^{4+}$	$^1\text{H}^+$
Image Charge Shift	-0.024(0.8)	-0.016(0.6)	-0.060(0.7)
Axial drive dependent shift	< +0.004(0.1)	< +0.005(0.2)	< +0.159(2.0)
Axial phase error	< 0.046(1.5)	< 0.026(1.0)	< 0.226(2.8)
Axial freq. diff. error	< 0.267(8.8)	< 0.299(11.1)	< 0.101(1.2)
Mod. cyc. modulation shift	-0.040(1.3)	-0.044(1.6)	-0.015(0.2)
Magnetic gradient (B_1) error	< 0.039(1.3)	< 0.031(1.2)	< 0.276(3.4)
Electrostatic gradient shift	+0.013(0.4)	+0.012(0.4)	+0.036(0.4)
Mod. cyc. fitting error	< 0.200(6.6)	< 0.300(11.1)	< 2.0(25.0)
Magnetic field drift /global fit error	< 0.301(10)	< 0.269(10)	< 0.802(10)

Table 6.6: Systematic errors and their absolute and relative contribution to the cyclotron frequencies. For shifts the sign of the shift (as compared to the true cyclotron frequency) is given. The values are calculated based on the measured magnetic field and an axial frequency of 4 MHz. All shifts are given in Hz, in brackets the relative shifts in ppb are calculated. The < - sign denotes that a conservative estimation was taken and the error could be smaller.

will be stated as the uncertainties in the errors are still too large.

Several of the systematic errors can be on a level of some ppb or even above 10 ppb. The dominating systematic error is hard to identify without further measurements. For future sub-ppb measurements it will be important to either eliminate the systematic effects or to map them out and correct for them (as it was the case in the Seattle measurements [VDPVLZ06]). The fit errors and the errors due to the problems in the axial detection are likely to be improved by enhancements in the precision voltage source stability and the magnetic field drift down to the Seattle values. The image charge shift, the axial drive dependent shift and the shifts due to magnetic and electrostatic gradients will have to be mapped and corrected for.

To summarize: Both the proton and the oxygen mass measurement agree reasonably well with the literature values. A more precise determination is mainly limited by the poor determination of the systematical effects in the spectrometer. This determination was complicated by problems with the precision voltage source, the magnetic field drift and the minimum configuration of the trap.

7 Conclusions and outlook

The MPIK/UW-PTMS, now being called THe-Trap, has come a long way (not only geographically). A dedicated tritium laboratory was installed in Heidelberg, the experiment was installed, commissioned and test measurements with ions were carried out. Finally, also the first mass measurements in the new setup were performed. Many new components, having been designed in Seattle and partly in Heidelberg, were tested for their applicability with single ions for the first time. This includes the detection system and the precision voltage source, two components, which have been completely redesigned compared to the original Seattle spectrometer. In addition, the computer-control system of the experiment and the data analysis tools were upgraded to allow for highly automated measurement routines. On the way to the first mass measurements several problems significantly slowed down or even stopped the experimental progress, however, most of them could be solved so far and in particular towards the end of this work the experimental progress sped up considerably.

The first mass measurements and many other measurements with ions in the trap demonstrated the fundamental ability of the trap to perform high-precision mass measurements on a competitive level. Even though the overall uncertainty of the measurements is on a 10^{-8} level, the statistical uncertainty (when being defined as the standard deviation from the mean value) in the modified cyclotron frequency was already below 1 part in 10^{10} . The experience from the earlier Seattle measurements and other Penning trap facilities shows that from the statistical point of view this uncertainty ultimately limits the precision of a Penning trap mass spectrometer. Concerning the systematic errors of the experiment, their analysis was limited by the problems with the precision voltage source and the endcap bias lines of the experiment not being connected. However, the extensive studies in Seattle on this issue allow to estimate that systematic effects will not limit the ability of the spectrometer to measure with uncertainties below 1 part in 10^{10} . Also, the insights from the mass measurements triggered several activities for the now upcoming revision phase of the experiment. This will include the improvement of the magnetic as well as electric field stability by upgrades to the magnetic field stabilization and the precision voltage source. First results for the voltage source point towards a tenfold improvement in the stability with the temperature stabilization being repaired. From the Seattle results for the magnetic field stabilization an improvement by at least an order of magnitude can also be expected. For the precision voltage source two possible alternatives might be investigated: The first is the use of the original Weston cells from the old UW-PTMS, the second is a new precision voltage source with a specified stability of $10^{-9}/h$ at 100 V, developed in cooperation with the Physikalisch-Technische Bundesanstalt (PTB) [Böh12].

The results of this thesis also initiated several new projects. One will be the more de-

tailed investigation of environmental effects on the modified cyclotron frequency [Str12], which became possible due to the high resolution already achieved. Another is the further investigation of the ion transport from the external ion source to the trap [Tre11] and between the traps [Höc13]. Also, simulation studies on the electrostatic properties of the traps [Sch11] will be carried out in order to complement the experimental findings on these issues.

After the revision period, the next step towards a ${}^3\text{H}/{}^3\text{He}$ mass measurement will be the test of two-ion techniques, which should significantly shorten the time between the measurements with different ions from days down to minutes. With this approach and the improvements already discussed above, uncertainties of 1 part in 10^{10} for mass measurements should be achieved within the next year. Interesting test candidates for the precision and accuracy achievable with the spectrometer could be identified in the mass spectra taken in this work. Possible candidates include absolute mass measurements on ${}^{14}\text{N}^{5+}$ or ${}^{19}\text{F}^{7+}$. Also measurements determining the mass ratio of ${}^{12}\text{C}^{5+}$ or ${}^{12}\text{C}^{6+}$ to ${}^{12}\text{C}^{4+}$ would provide a strong test for the uncertainty achievable with the spectrometer and strengthen the confidence in its experimental results. In parallel, the ion transport from the external ion source should be optimized so far that loading ions created from gas samples into the capture trap will be possible. Then, the next logical step will be measurements involving the ${}^3\text{He}^+$ ion. An appealing measurement would be the verification of its absolute mass by performing a measurement against ${}^{12}\text{C}^{4+}$. The final goal of this project then will be to load ${}^3\text{H}^+$ and perform the Q -value measurement that are so highly desirable for the KATRIN experiment and the search for the neutrino mass.

Bibliography

- [A⁺04] J. ANGRİK ET AL. *KATRIN Design Report*, 2004.
- [A⁺11] B. ANDREAS ET AL. *Determination of the Avogadro Constant by Counting the Atoms in a ²⁸Si Crystal*. *Phys. Rev. Lett.*, volume 106(3):030801, 2011.
- [AEE08] F. T. AVIGNONE, S. R. ELLIOTT AND J. ENGEL. *Double beta decay, Majorana neutrinos, and neutrino mass*. *Rev. Mod. Phys.*, volume 80(2):481, 2008.
- [AGG85] G. AUDI, R. L. GRAHAM AND J. S. GEIGER. *Evaluation of the ³H-³He Atomic Mass Difference*. *Z. Phys. A*, volume 321:533, 1985.
- [And62] P. W. ANDERSON. *Theory of Flux Creep in Hard Superconductors*. *Phys. Rev. Lett.*, volume 9(7):309, 1962.
- [Ast19] F. W. ASTON. *The Mass-Spectra of Chemical Elements*. *Phil. Mag.*, volume 38:707, 1919.
- [Ast22] F. W. ASTON. *The Atoms of Matter; their Size, Number, and Construction*. *Nature*, volume 110:702, 1922.
- [AWT03] G. AUDI, A. H. WAPSTRA AND C. THIBAUT. *The 2003 atomic mass evaluation: (II). Tables, graphs and references*. *Nucl. Phys. A*, volume 729(1):337, 2003.
- [BB08] K. BEYER AND F. BUSCH. *Schwingungsmessungen zur Aufstellung eines Penningfallen-Massenspektrometers*. Technical report, 2008.
- [BESW01] S. BRUNNER, T. ENGEL, A. SCHMITT AND G. WERTH. *Determination of the helium-4 mass in a Penning trap*. *Eur. Phys. J. D*, volume 15:181, 2001.
- [BG82] L. S. BROWN AND G. GABRIELSE. *Precision spectroscopy of a charged particle in an imperfect Penning trap*. *Phys. Rev. A*, volume 25(4):2423, 1982.
- [BG86] L. S. BROWN AND G. GABRIELSE. *Geonium theory: Physics of a single electron or ion in a Penning trap*. *Rev. Mod. Phys.*, volume 58(1):233, 1986.

- [Böh12] C. BÖHM. *to be announced*. PhD Thesis, University of Heidelberg, 2012.
- [BJ57] I. BRODIE AND R. O. JENKINS. *The nature of the emitting surface of barium dispenser cathodes*. Brit. J. Appl. Phys., volume 8:27, 1957.
- [Bla06] K. BLAUM. *High-accuracy mass spectrometry with stored ions*. Phys. Rep., volume 425(1):1, 2006.
- [BNW10] K. BLAUM, Y. NOVIKOV AND G. WERTH. *Penning traps as a versatile tool for precise experiments in fundamental physics*. Contemp. Phys., volume 51:149, 2010.
- [Boe09] F. BOESSELMANN. *Gutachten zur Luftdichtigkeit des Tritiumlabor*, 2009.
- [C⁺89] E. A. CORNELL ET AL. *Single-ion cyclotron resonance measurement of $M(\text{CO}^+)/M(\text{N}_2^+)$* . Phys. Rev. Lett., volume 63(16):1674, 1989.
- [CAC49] S. C. CURRAN, J. ANGUS AND A. L. COCKROFT. *The Beta-Spectrum of Tritium*. Phys. Rev., volume 76(6):853, 1949.
- [COTW06] R. G. COOKS, Z. OUYANG, Z. TAKATS AND J. M. WISEMAN. *Ambient Mass Spectrometry*. Science, volume 311(5767):1566, 2006.
- [Cra81] D. H. CRANDALL. *Electron Impact Ionization of Multicharged Ions*. Phys. Scripta, volume 23:153, 1981.
- [CRH⁺56] C. L. COWAN, JR., F. REINES, F. B. HARRISON, H. W. KRUSE AND A. D. MCGUIRE. *Detection of the Free Neutrino: A Confirmation*. Science, volume 124:103, 1956.
- [D⁺09] J. DUNKLEY ET AL. *Five-Year Wilkinson Microwave Anisotropy Probe Observations: Likelihoods and Parameters from the WMAP Data*. Astrophys. J. Suppl. Ser., volume 180(2):306, 2009.
- [Deh68] H. DEHMELT. *Radiofrequency Spectroscopy of Stored Ions I: Storage*. volume 3:53, 1968.
- [Deh69] H. DEHMELT. *Radiofrequency Spectroscopy of Stored Ions II: Spectroscopy*. volume 5:109, 1969.
- [Deh90] H. DEHMELT. *Experiments with an isolated subatomic particle at rest*. Rev. Mod. Phys., volume 62:525, 1990.
- [Dem35] A. J. DEMPSTER. *New Methods in Mass Spectrometry*. Proc. Am. Phil. Soc., volume 75(8):755, 1935.

- [DFC⁺01] G. DOUYSET, T. FRITIOFF, C. CARLBERG, I. BERGSTRÖM AND M. BJÖRKHAGE. *Determination of the ^{76}Ge Double Beta Decay Q Value*. Phys. Rev. Lett., volume 86(19):4259, 2001.
- [DSL09] C. DIEHL, J. SCHREINER AND R. LACKNER. *Tritiumsicherheitskonzept*. handed in to: Regierungspräsidium Karlsruhe, 2009.
- [E⁺08] T. ERONEN ET AL. *Preparing isomerically pure beams of short-lived nuclei at JYFLTRAP*. Nucl. Instr. Meth. B, volume 266:4527, 2008.
- [E⁺10] S. ELISEEV ET AL. *Direct mass measurements of ^{194}Hg and ^{194}Au : A new route to the neutrino mass determination?* Phys. Lett. B, volume 693:426, 2010.
- [E⁺11] S. ELISEEV ET AL. *Resonant Enhancement of Neutrinoless Double-Electron Capture in ^{152}Gd* . Phys. Rev. Lett., volume 106(5):052504, 2011.
- [Ear42] S. EARNSHAW. *On the nature of the molecular forces which regulate the constitution of the luminiferous ether*. Trans. Camb. Phil. Soc, volume 7:97, 1842.
- [EHM87] S. R. ELLIOTT, A. A. HAHN AND M. K. MOE. *Direct evidence for two-neutrino double-beta decay in ^{82}Se* . Phys. Rev. Lett., volume 59(18):2020, 1987.
- [Ein05] A. EINSTEIN. *Zur Elektrodynamik bewegter Körper*. Annalen der Physik, volume 322:891, 1905.
- [F⁺95] B. FRANZKE ET AL. *Schottky mass spectrometry at the experimental storage ring ESR*. Phys. Script., volume 59:176, 1995.
- [F⁺04] M. FISCHER ET AL. *New Limits on the Drift of Fundamental Constants from Laboratory Measurements*. Phys. Rev. Lett., volume 92(23):230802, 2004.
- [Far95] D. L. FARNHAM. *A determination of the proton/electron mass ratio and the electron's atomic mass via Penning trap mass spectroscopy*. PhD Thesis, University of Washington, 1995.
- [Fer34] E. FERMI. *Tentativo di una Teoria Dei Raggi ?* Il Nuovo Cimento, volume 11:1, 1934.
- [FGM08] B. FRANZKE, H. GEISSEL AND G. MÜNZENBERG. *Mass and lifetime measurements of exotic nuclei in storage rings*. Mass Spectrom. Rev., volume 27(5):428, 2008.

- [G⁺99] G. GABRIELSE ET AL. *Precision Mass Spectroscopy of the Antiproton and Proton Using Simultaneously Trapped Particles*. Phys. Rev. Lett., volume 82(16):3198, 1999.
- [G⁺07] S. GEORGE ET AL. *Ramsey Method of Separated Oscillatory Fields for High-Precision Penning Trap Mass Spectrometry*. Phys. Rev. Lett., volume 98(16):162501, 2007.
- [Gab83] G. GABRIELSE. *Relaxation calculation of the electrostatic properties of compensated Penning traps with hyperbolic electrodes*. Phys. Rev. A, volume 27(5):2277, 1983.
- [Gab09a] G. GABRIELSE. *The true cyclotron frequency for particles and ions in a Penning trap*. Int. J. Mass Spectr., volume 279(2-3):107, 2009.
- [Gab09b] G. GABRIELSE. *Why Is Sideband Mass Spectrometry Possible with Ions in a Penning Trap?* Phys. Rev. Lett., volume 102(17):172501, 2009.
- [GDG10] N. GUISE, J. DISCIACCA AND G. GABRIELSE. *Self-Excitation and Feedback Cooling of an Isolated Proton*. Phys. Rev. Lett., volume 104(14):143001, 2010.
- [GK78] G. GÄRTNER AND E. KLEMPT. *A direct determination of the proton-electron mass ratio*. Z. Phys. A, volume 287:1, 1978.
- [GKT80] G. GRÄFF, H. KALINOWSKY AND J. TRAUT. *A direct determination of the proton electron mass ratio*. Z. Phys. A, volume 297:35, 1980.
- [GM96] S. GUAN AND A. G. MARSHALL. *Stored waveform inverse Fourier transform (SWIFT) ion excitation in trapped-ion mass spectrometry: Theory and applications*. Int. J. Mass Spectr., volume 157:5, 1996.
- [GMRW68] G. GRÄFF, F. G. MAJOR, R. W. ROEDER AND G. WERTH. *Method for Measuring the Cyclotron and Spin Resonance of Free Electrons*. Phys. Rev. Lett., volume 21:340, 1968.
- [GT88] G. GABRIELSE AND J. TAN. *Self-shielding superconducting solenoid systems*. J. Appl. Phys., volume 63(10):5143, 1988.
- [GWW90] C. GERZ, D. WILSDORF AND G. WERTH. *A high precision Penning trap mass spectrometer*. Nucl. Instr. Meth. B, volume 47(4):453, 1990.
- [H⁺00] M. HAUSMANN ET AL. *First isochronous mass spectrometry at the experimental storage ring ESR*. Nucl. Instr. Meth. A, volume 446:569, 2000.

- [HFG08] D. HANNEKE, S. FOGWELL AND G. GABRIELSE. *New measurement of the electron magnetic moment and the fine structure constant*. Phys. Rev. Lett., volume 100(12):120801, 2008.
- [HH89] P. HOROWITZ AND W. HILL. *The Art of Electronics, 2nd ed.* Cambridge, 1989.
- [Höc10] M. HÖCKER. *Ion Transfer Studies in the UW/MPIK Double-Penning Trap Experiment*. Diploma Thesis, University of Heidelberg, 2010.
- [Höc13] M. HÖCKER. *to be announced*. PhD Thesis, University of Heidelberg, 2013.
- [HTW06] S. HANNESTAD, H. TU AND Y. Y. Y. WONG. *Measuring neutrino masses and dark energy with weak lensing tomography*. J. Cosm. Astrop. Phys., volume 2006(06):025, 2006.
- [HZH⁺95] T. P. HEAVNER, M. ZUO, P. HAYES, G. H. DUNN AND S. R. JEFFERTS. *The JILA Penning trap mass spectrometer*. Phys. Script. A, volume 1995:414, 1995.
- [IR50] M. G. INGRAM AND J. H. REYNOLDS. *Double Beta-Decay of ^{130}Te* . Phys. Rev., volume 78(6):822, 1950.
- [J⁺93] R. JERTZ ET AL. *Direct determination of the mass of ^{28}Si as a contribution to a new definition of the kilogram*. Phys. Script., volume 48:399, 1993.
- [K⁺05] C. KRAUS ET AL. *Final results from phase II of the Mainz neutrino mass search in tritium β -decay*. Eur. Phys. J. C, volume 40:447, 2005.
- [K⁺09] J. KETELAER ET AL. *Recent developments in ion detection techniques for Penning trap mass spectrometry at TRIGA-TRAP*. Eur. Phys. J. A, volume 42:311, 2009.
- [KDHK01] H. V. KLAPDOR-KLEINGROTHAUS, A. DIETZ, H. L. HARNEY AND I. V. KRIVOSHEINA. *Evidence for Neutrinoless Double Beta Decay*. Mod. Phys. Lett. A, volume 16:2409, 2001.
- [Ket11] J. KETTER. *Calculations on the modulation shift*. Private communication, 2011.
- [L⁺85] E. LIPPMAA ET AL. *Precise ^3H - ^3He Mass Difference for Neutrino Mass Determination*. Phys. Rev. Lett., volume 54(4):285, 1985.
- [L⁺01] V. M. LOBASHEV ET AL. *Direct search for neutrino mass and anomaly in the tritium beta-spectrum: Status of Troitsk neutrino mass experiment*. Nucl. Phys. B Proc. Suppl., volume 91(1-3):280, 2001.

- [LFLM90] J. LOCKHART, R. FAGALY, L. LOMBARDO AND B. MUHLFELDER. *Magnetic susceptibility of instrument materials below 10 K*. Physica B, volume 165-166:147, 1990.
- [LL76] L. LANDAU AND E. LIFSCHITZ. *Lehrbuch der theoretischen Physik I - Mechanik*. Akademie-Verlag Berlin, 1976.
- [LM52] L. M. LANGER AND R. J. D. MOFFAT. *The Beta-Spectrum of Tritium and the Mass of the Neutrino*. Phys. Rev., volume 88(4):689, 1952.
- [LP06] J. LESGOURGUES AND S. PASTOR. *Massive neutrinos and cosmology*. Phys. Rep., volume 429(6):307, 2006.
- [LU00] L. L. LUCAS AND M. P. UNTERWEGER. *Comprehensive Review and Critical Evaluation of the Half-Life of Tritium*. J. Res. NIST, volume 1045(4):541, 2000.
- [M⁺06] A. MONFARDINI ET AL. *The microcalorimeter arrays for a rhenium experiment (MARE): A next-generation calorimetric neutrino mass experiment*. Nucl. Instr. Meth. A, volume 559(2):346, 2006.
- [M⁺07] R. N. MOHAPATRA ET AL. *Theory of neutrinos: a white paper*. Rep. Prog. Phys., volume 70(11):1757, 2007.
- [M⁺08] M. MUKHERJEE ET AL. *ISOLTRAP: An on-line Penning trap for mass spectrometry on short-lived nuclides*. Eur. Phys. J. A, volume 35:1, 2008.
- [Mat68] E. MATHIEU. *Mémoire sur le mouvement vibratoire d'une membrane de forme elliptique*. J. Math. Pure Appl., volume 13:137, 1868.
- [MGW05] F. G. MAJOR, V. N. GHEORGHE AND G. WERTH. *Plasma properties*. In *Charged Particle Traps*, volume 37 of *Atomic, optical, and plasma physics*, 263. Springer Berlin Heidelberg, 2005.
- [MH34] J. MATTAUCH AND R. HERZOG. *Über einen neuen Massenspektrographen*. Z. Phys., volume 89:786, 1934.
- [Moo89] F. L. MOORE. *High resolution mass spectroscopy in a quadring Penning trap*. PhD Thesis, University of Washington, 1989.
- [MRM09] B. J. MOUNT, M. REDSHAW AND E. G. MYERS. *Q Value of $In^{115} \rightarrow Sn^{115}(3/2+)$: The Lowest Known Energy β -Decay*. Phys. Rev. Lett., volume 103(12):122502, 2009.
- [MTN08] P. J. MOHR, B. N. TAYLOR AND D. B. NEWELL. *CODATA recommended values of the fundamental physical constants: 2006*. J. Phys.Chem. Ref. Data, volume 37:1187, 2008.

- [N⁺10] K. NAKAMURA ET AL. *Review of particle physics*. J. Phys. G, volume 37:075021, 2010.
- [NFB⁺06] S. NAGY, T. FRITIOFF, M. BJÖRKHAGE, I. BERGSTRÖM AND R. SCHUCH. *On the Q-value of the tritium β -decay*. Europhys. Lett., volume 74:404, 2006.
- [Nie47] A. O. NIER. *A Mass Spectrometer for Isotope and Gas Analysis*. Rev. Sci. Instr., volume 18:398, 1947.
- [NKS77] D. E. NELSON, R. G. KORTELING AND W. R. STOTT. *Carbon-14: Direct Detection at Natural Concentrations*. Science, volume 198(4316):507, 1977.
- [OBW06] E. W. OTTEN, J. BONN AND C. WEINHEIMER. *The Q-value of tritium β -decay and the neutrino mass*. Int. J. Mass Spectr., volume 251(2-3):173, 2006.
- [OHR34] M. L. E. OLIPHANT, P. HARTECK AND L. RUTHERFORD. *Transmutation Effects Observed with Heavy Hydrogen*. Proc. Roy. Soc. London A, volume 144(853):692, 1934.
- [Ott94] E. OTTEN. *The Mainz neutrino mass experiment*. Prog. Part. Nucl. Phys., volume 32:153, 1994.
- [OW08] E. W. OTTEN AND C. WEINHEIMER. *Neutrino mass limit from tritium β -decay*. Rep. Prog. Phys., volume 71(8):086201, 2008.
- [P⁺92] A. PICARD ET AL. *A solenoid retarding spectrometer with high resolution and transmission for keV electrons*. Nucl. Instr. Meth. B, volume 63(3):345, 1992.
- [Pau90] W. PAUL. *Electromagnetic traps for charged and neutral particles*. Rev. Mod. Phys., volume 62(3):531, 1990.
- [PBB⁺09] D. B. PINEGAR, K. BLAUM, T. P. BIESIADZINSKI, S. L. ZAFONTE AND R. S. VAN DYCK, JR. *Stable voltage source for Penning trap experiments*. Rev. Sci. Instr., volume 80(6):064701, 2009.
- [Pen36] F. PENNING. *Die Glimmentladung bei niedrigem Druck zwischen koaxialen Zylindern in einem axialen Magnetfeld*. Physica, volume 3(9):873, 1936.
- [Pie49] J. R. PIERCE. *Theory and Design of Electron Beams*, chapter 3. D. van Nostrand Co., 1949.

- [Pin03] D. B. PINEGAR. *Design of THe-Trap ion source*. unpublished, 2003.
- [Pin07] D. B. PINEGAR. *Tools for a precise tritium to helium-3 mass comparison*. PhD Thesis, University of Washington, 2007.
- [Pon58] B. PONTECORVO. *Mesonium and Antimesonium*. Sov. J. Exp. Theor. Phys., volume 6:429, 1958.
- [Por01] J. V. PORTO. *Series solution for the image charge fields in arbitrary cylindrically symmetric Penning traps*. Phys. Rev. A, volume 64(2):023403, 2001.
- [PRSZ04] B. POVH, K. RITH, C. SCHOLZ AND F. ZETSCHKE. *Teilchen und Kerne*. Springer, 2004.
- [PS53] W. PAUL AND H. STEINWEDEL. *Ein neues Massenspektrometer ohne Magnetfeld*. Z. Naturf. A, volume 8:448, 1953.
- [R⁺05] S. RAINVILLE ET AL. *A direct test of $E = mc^2$* . Nature, volume 438(7071):1096, 2005.
- [R⁺08] S. RAHAMAN ET AL. *Q values of the ^{76}Ge and ^{100}Mo double-beta decays*. Phys. Lett. B, volume 662:111, 2008.
- [Red07] M. REDSHAW. *Precise Measurements of the Atomic Masses of ^{28}Si , ^{31}P , ^{32}S , $^{84,86}\text{Kr}$, $^{129,132,136}\text{Xe}$, and the Dipole Moment of PH^+ using Single-Ion and Two-Ion Penning Trap Techniques*. PhD Thesis, FSU, 2007.
- [RMM08] M. REDSHAW, J. MCDANIEL AND E. G. MYERS. *Dipole Moment of PH^+ and the Atomic Masses of Si-28, P-31 by Comparing Cyclotron Frequencies of Two Ions Simultaneously Trapped in a Penning Trap*. Phys. Rev. Lett., volume 100(9):093002, 2008.
- [RTP04] S. RAINVILLE, J. K. THOMPSON AND D. E. PRITCHARD. *An Ion Balance for Ultra-High-Precision Atomic Mass Measurements*. Science, volume 303(5656):334, 2004.
- [RVJM10] B. A. REID, L. VERDE, R. JIMENEZ AND O. MENA. *Robust neutrino constraints by combining low redshift observations with the CMB*. J. Cosm. Astrop. Phys., volume 2010(01):003, 2010.
- [RWMM07] M. REDSHAW, E. WINGFIELD, J. MCDANIEL AND E. G. MYERS. *Mass and double-beta-decay Q value of Xe-136*. Phys. Rev. Lett., volume 98(5):053003, 2007.

- [S⁺90] H. STOLZENBERG ET AL. *Accurate mass determination of short-lived isotopes by a tandem Penning-trap mass spectrometer.* Phys. Rev. Lett., volume 65(25):3104, 1990.
- [S⁺04] M. SISTI ET AL. *New limits from the Milano neutrino mass experiment with thermal microcalorimeters.* Nucl. Instr. Meth. A, volume 520(1-3):125, 2004.
- [S⁺05] S. SCHÖNERT ET AL. *The GERmanium Detector Array (GERDA) for the search of neutrinoless $\beta\beta$ decays of ^{76}Ge at LNGS.* Nucl. Phys. B - Proc. Suppl., volume 145:242, 2005.
- [Sak58] J. J. SAKURAI. *Rest Mass of the Neutrino.* Phys. Rev. Lett., volume 1(1):40, 1958.
- [SBN⁺08] A. SOLDERS, I. BERGSTRÖM, S. NAGY, M. SUHONEN AND R. SCHUCH. *Determination of the proton mass from a measurement of the cyclotron frequencies of D^+ and H_2^+ in a Penning trap.* Phys. Rev. A, volume 78(1):012514, 2008.
- [Sch08] J. SCHREINER. *Private communication*, 2008.
- [Sch11] M. SCHUH. *to be announced.* Bachelor Thesis, University of Heidelberg, 2011.
- [Scr10] *Scripps center for mass spectrometry*, 2010.
- [SD56] L. G. SMITH AND C. C. DAMM. *Mass Synchrometer.* Rev. Sci. Instr., volume 27:638, 1956.
- [ŠFR⁺08] F. ŠIMKOVIC, A. FAESSLER, V. RODIN, P. VOGEL AND J. ENGEL. *Anatomy of the $0\nu\beta\beta$ nuclear matrix elements.* Phys. Rev. C, volume 77(4):045503, 2008.
- [Str11] S. STREUBEL. *He-Gas Druck-Stabilisierung.* unpublished, 2011.
- [Str12] S. STREUBEL. *to be announced.* PhD Thesis, University of Heidelberg, 2012.
- [STV08] T. SCHWETZ, M. TORTOLA AND J. W. F. VALLE. *Three-flavour neutrino oscillation update.* New J. Phys., volume 10(11):113011, 2008.
- [SVDD81] P. B. SCHWINBERG, R. S. VAN DYCK, JR. AND H. G. DEHMELT. *Trapping and thermalization of positrons for geonium spectroscopy.* Phys. Lett. A, volume 81(2-3):119, 1981.

- [SW75] L. G. SMITH AND A. H. WAPSTRA. *Masses of isotopes of H, He, C, N, O, and F*. Phys. Rev. C, volume 11(4):1392, 1975.
- [TG95] C. H. TSENG AND G. GABRIELSE. *One-electron parametric oscillator*. Appl. Phys. B, volume 60:95, 1995.
- [Tho97] J. J. THOMSON. *Cathode rays*. Phil. Mag., volume 3:293, 1897.
- [Tho07] J. J. THOMSON. *On rays of positive electricity*. Phil. Mag., volume 13:561, 1907.
- [Tho12] J. J. THOMSON. *Further experiments on positive rays*. Phil. Mag., volume 24:209, 1912.
- [Tre11] M. TREMER. *to be announced*. Diploma Thesis, University of Heidelberg, 2011.
- [UDRL⁺09] M. UBIETO-DÍAZ, D. RODRÍGUEZ, S. LUKIC, S. NAGY, S. STAHL AND K. BLAUM. *A broad-band FT-ICR Penning trap system for KATRIN*. Int. J. Mass Spectr., volume 288(1-3):1, 2009.
- [VD95] R. S. VAN DYCK, JR. *Ultra-High-Resolution Mass Spectroscopy in Penning Traps*, chapter 13, 363. Academic Press, 1995.
- [VD10] R. S. VAN DYCK, JR. *Private communication*, 2010.
- [VDFDP89] R. S. VAN DYCK, JR., F. L. MOORE, D.L. FARNHAM AND P. B. SCHWINBERG. *Mass Ratio Spectroscopy and the Proton's Atomic Mass*. In *Frequency Standards and Metrology*. A. De Marchi Jr., 1989.
- [VDFS93] R. S. VAN DYCK, JR., D. L. FARNHAM AND P. B. SCHWINBERG. *Tritium-helium-3 mass difference using the Penning trap mass spectroscopy*. Phys. Rev. Lett., volume 70(19):2888, 1993.
- [VDFZS99] R. S. VAN DYCK, JR., D. L. FARNHAM, S. L. ZAFONTE AND P. B. SCHWINBERG. *Ultrastable superconducting magnet system for a Penning trap mass spectrometer*. Rev. Sci. Instr., volume 70(3):1665, 1999.
- [VDPVLZ06] R. S. VAN DYCK, JR., D. B. PINEGAR, S. VAN LIEW AND S. L. ZAFONTE. *The UW-PTMS: Systematic studies, measurement progress, and future improvements*. Int. J. Mass Spectr., volume 251(2-3):231, 2006.
- [VDS81] R. S. VAN DYCK, JR. AND P. B. SCHWINBERG. *Preliminary proton/electron mass ratio using a compensated quadring Penning trap*. Phys. Rev. Lett., volume 47(6):395, 1981.

- [VDS87] R. S. VAN DYCK, JR., P. B. SCHWINBERG AND H. G. DEHMELT. *New high-precision comparison of electron and positron g factors*. Phys. Rev. Lett., volume 59(1):26, 1987.
- [VDW76] R. S. VAN DYCK, JR., D. J. WINELAND, P. A. EKSTROM AND H. G. DEHMELT. *High mass resolution with a new variable anharmonicity Penning trap*. Appl. Phys. Lett., volume 28(8):446, 1976.
- [VDZ01] R. S. VAN DYCK, JR., S. L. ZAFONTE AND P. B. SCHWINBERG. *Ultra-precise mass measurements using the UW-PTMS*. Hyperfine Interactions, volume 132(1–4):163, 2001.
- [VDZVL⁺04] R. S. VAN DYCK, JR., S. L. ZAFONTE, S. VAN LIEW, D. B. PINEGAR AND P. B. SCHWINBERG. *Ultraprecise atomic mass measurement of the α particle and ^4He* . Phys. Rev. Lett., volume 92(22):220802, 2004.
- [VL04] S. VAN LIEW. *An ultra-precise determination of the mass of helium-3 using Penning trap mass spectrometry*. PhD Thesis, University of Washington, Seattle, 2004.
- [Wap95] A. H. WAPSTRA. *Atomic masses: Thomson to ion traps*. Phys. Scripta, volume 59:65, 1995.
- [WD75] D. J. WINELAND AND H. G. DEHMELT. *Principles of the stored ion calorimeter*. J. Appl. Phys., volume 46:919, 1975.
- [WED78] D. WINELAND, P. EKSTROM AND H. DEHMELT. *Monoelectron oscillator*. Phys. Rev. Lett., volume 31(21):1279, 1978.
- [Wol95] B. WOLF. *Handbook of ion sources*. CRC press, 1995.
- [WW46] R. J. WATTS AND D. WILLIAMS. *Beta-rays from ^3H* . Phys. Rev., volume 70(9-10):640, 1946.
- [Zaf07] S. L. ZAFONTE. *Design notes for compensation coils*. unpublished, 2007.

Acknowledgement

Obviously, the results of a PhD thesis are never obtained alone. So, I would like to thank all people, who contributed to this thesis in one or the other way.

First of all, I would like to thank my supervisor, Prof. Dr. Klaus Blaum, for the opportunity to work on this experiment. Klaus, you always have been as supportive as possible, in particular concerning the possibility of flexible working. In addition, your door was always open, when I had questions, despite your tough schedule as a director at MPIK.

I express my sincere gratitude to Prof. Dr. Robert S. Van Dyck, Jr., who contributed all the equipment available at University of Washington. In addition, he always was available for questions about the mysterious things happening in a Penning trap.

Thanks to PD Dr. Wolfgang Quint for providing the second opinion on the thesis.

Thanks to Dr. David Pinegar for setting up the experiment and introducing me into the operation of THE-Trap. Also thanks for the interesting time in Seattle.

Thanks a lot to Jochen Ketter for all his support throughout the studies in Mainz and Heidelberg. Thanks for keeping the electronics of the experiment in good shape. A special thank for the proof-reading of the thesis and all the good suggestions.

Thanks to Martin Höcker for joining the experiment as a diploma student and always being so passionate about new ideas and suggestions. Also thanks for providing programming support for the evaluation of the data.

Thanks to Sebastian Streubel for keeping the environment as stable as possible during the relevant measurement period at the end of the thesis. Also thanks for the hospitality in his apartment and the nice company at the Winter school.

Thanks to Marius Tremer for his patience as my measurements were delaying his measurement period. Also thanks for several rides to the Heidelberg station.

Thanks to Dr. Jochen Schreiner and Ralf Lackner from the MPIK radiation safety group for all their efforts around our laboratory.

Thanks to Ralph Zilly for his support during the build-up phase and the filling of the magnet with nitrogen.

Thanks to Gertrud Dücker for organisational support and her warm and friendly attitude, whenever entering her office.

Thanks to the present and former members of the division “Stored and Cooled Ions” at MPIK and in Mainz for nice discussions and company throughout this thesis.

Thanks to the IMPRS-QD and the HGSFP for financial support during the thesis and stimulating events, such as the winter schools and the PhD retreat.

Thanks to Deutsche Bahn for being in time mostly.

Thanks to my parents for financial and personal support throughout the time of my studies.

There are no words to express the thanks for my wife Constanze, which has joined and suffered the whole time of my studies. It is amazing to be with you and to start a new family together with Cecilia. Also, special thanks to Cecilia for always letting me sleep enough during the writing phase for the thesis.